ZINC OXIDE NANOWIRES FOR SENSING AND POWER GENERATION FOR SYSTEM-ON-PACKAGE TECHNOLOGY

A Thesis
Presented to
The Academic Faculty

By

Jin Liu

In Partial Fulfillment
Of the Requirements for the Degree
Doctor of Philosophy in the
School of Electrical and Computer Engineering

Georgia Institute of Technology

December, 2008

ZnO Nanowires for Sensing and Power Generation for System-On-Package Technology

Approved by:

Dr. Rao R. Tummala, Advisor
School of Electrical and Computer Engineering
Georgia Institute of Technology

Dr. Oliver Brand
School of Electrical and Computer Engineering
Georgia Institute of Technology

Dr. Zhong Lin (ZL) Wang, Co-Advisor
School of Materials Science and Engineering
Georgia Institute of Technology

Dr. Maysam Ghovanloo
School of Electrical and Computer Engineering
Georgia Institute of Technology

Dr. Gee-Kung Chang,
School of Electrical and Computer Engineering
Georgia Institute of Technology

Dr. Ching-Ping (CP) Wong
School of Materials Science and Engineering
Georgia Institute of Technology

Date Approved: October, 9, 2008

To my parents and my wife

ACKNOWLEDGEMENTS

I would like express my thanks to my advisors, Dr. Rao Tummala and Dr. Zhong Lin (ZL) Wang for their guidance and support through the course my Ph.D. study. I met Dr. Tummala when I was studying in Singapore. It is him who gave me the opportunity to study in the States. It is also him whose professionalism, kindness, and tolerance teach me and influence me into who I am today. I feel very fortunate to have a very close relationship and interaction with Dr. ZL Wang and his group. His enthusiasm and care set a high standard which I won't be able to surpass. I also would like to thank Dr. Gee-Kung Chang for serving as my proposal committee chair and dissertation reading committee member. The first year I was in Georgia Tech is a pleasant memory because of him. Dr. Oliver Brand has been kind enough to serve both at my proposal and dissertation committees. I would like to thank him as well. Dr. Mahadevan Iyer is acknowledged for serving on my proposal committee. Dr. C P Wong and Dr. Maysam Ghovanloo are acknowledged for being the dissertation committee members.

This thesis concludes my life as a pure student. Family and friends certainly play a very important role during the more than 20 years of study. I want to thank my parents to sacrifice all they have to support me. This thesis is dedicated to them. I also want to thank my friends during various stages of my student career, without them the life could have been more pale and tough. Finally, I want to share this thesis with my wife Jie Chen, whose support and encouragement make this possible.

TABLE OF CONTENTS

LIST OF TABLES

LIST OF FIGURES

SUMMARY

As the science and technology advance, people are looking for new discoveries to solve the existing problems and improve the quality of life. In this processes of development, nanoscience and nanotechnology have attracted technologists' attention and turned out to be one of the most promising technologies that could have a revolutionary impact. Znic Oxide (ZnO) nanostructures, in particular nanowires (NWs), have the potential to be one of such revolutionary material. ZnO is a piezoelectric, transparent and semiconducting material. With a direct band gap of 3.37eV and large excitation binding energy (60meV), ZnO exhibits near-UV emission, and transparent conductivity. ZnO NWs, with all of the properties of bulk ZnO, have other properties that are distinct to nanoscale material. All of these make ZnO NWs a very unique material that has many potential applications in system miniaturization.

System-on-package (SOP) technology is a new concept developed to solve the integration problem in microelectronic industry. SOP technology paradigm provides system-level miniaturization in a package size that makes today's hand-held devices into multi-functional systems, with applications ranging from computing, wireless communications, health care to personal security. The SOP is a system miniaturization technology that ultimately integrates nanoscale thin film components for batteries, thermal structures, active and passive components in low cost organic packaging substrates, leading to micro to nanoscale modules and systems.

The goal of this research is to investigate and utilize the unique properties of ZnO NWs and apply them to the fabrication of devices that can be integrated with SOP

platform. The issues include developing techniques to manipulate and align ZnO NWs; developing contact preparation method to improve the contact conductance for the fabrication of ZnO NW based devices. Also, the investigation of the oxygen diffusion coefficient in ZnO NWs is carried out, which serves as the basis of ZnO NWs for sensing applications. Two practical applications, which include fabricating and characterizing SOP compatible ZnO NW based bio-sensor and SOP compatible ZnO NW based nano-generator, are evaluated. Finally the remaining work beyond the scope of the thesis is outlined.

CHAPTER I
INTRODUCTION

The modern world is advancing in an astounding pace that nobody has expected. In the past 40 years or so, people have witnessed many technological developments that are marked with breakthroughs in many scientific fields. These advancements bring the ways of human living to an unprecedented level. For example, since the first construction of point contact transistor by John Bardeen and Walter Brattain in 1947, there is a rapid and tremendous research and development effort going on which ultimately leads to the concept and realization of the information technology (IT) era. People are getting used to the fact that the technology revolution has been kept going for such a long time that no one expects that we are going to reach the end of the tunnel very soon.

It seems, however, that at least some of the technology advances have become close, if not reached, the end of the tunnel. Moore's Law, which essentially states that the number of transistors that can be placed on an integrated circuit is doubling every eighteen months, has been the driving force for the semiconductor industry ever since its inauguration. Scientists are working hard to find ways to reduce the size of the transistors to squeeze more transistors inexpensively on the same die size to keep up with the pace of Moore's Law. As a result, the dimension of the transistor has shrunk to the stage where any size reduction is virtually beyond physical limit which is governed by semiconductor device physics. Scientists are therefore searching for alternatives to the

simple physical size reduction methodology to not only keep Moore's Law valid, but also make new progress for the good of human being. Nanotechnology, which becomes a focused research area lately, has the potential to become one of the key technologies that reshape the world.

1.1 Background Overview

1.1.1 Nanotechnology

Physicist Richard Feynman gave a speech in 1959 entitled "There's Plenty of Room at the Bottom". During the talk, he described a process by which the ability to manipulate individual atoms and molecules might be developed [1]. This is generally considered the origin of the nanotechnology, although it was not called that way at that time. The definition of the nanotechnology is explored and expanded in the following years. As of today, it is generally agreed that the nanotechnology refers to a broad field of applied sciences and technologies whose research areas involve the materials with at least one dimension in the range of one to several hundred nanometers.

Compared with their bulk counterparts, many materials exhibit distinct properties when their sizes are reduced into nanoscale. These differences in properties come mainly from the quantum effect and surface phenomena associated with the reduction in dimension. . For example, semiconductor quantum dot (QD) has a unique relationship between its luminescence spectrum and its size. This unique property is the result of semiconductor quantum effect when the material dimension is in nanoscale, hence the name QD. It has been a hot research topic in scientific research community and found

applications in biological labeling and cancer detection [2-4]. Another example relates to the surface phenomena of nanoscale material. Scientists have demonstrated that Silicon (Si) nanowires (NWs) can be used as bio-sensors to detect bio-molecules with ultra low concentration [5]. This is because of the high surface-to-volume ratio associated with Si NWs. Any small charge redistribution around the NW can be reflected as the conductance change of the NW itself.

By demonstrating its potential capability to improve human lives and contribute to the economic growth, nanotechnology is expected to have a high impact in research as well as everyday life. As a result, researchers are working hard to discover more and more nanomaterials and nanostructures with novel properties. Znic oxide (ZnO) nanostructures have turned out to be one of the most promising categories in the field.

1.1.2 ZnO Nanostructures

ZnO is an interesting and one of the most important materials that scientists have been working not only on its nanoscale structures, but bulk forms as well. ZnO is a piezoelectric, transparent and semiconductive material. With a direct band gap of 3.37eV and large excitation binding energy (60meV), ZnO exhibits near-UV emission, transparent conductivity, and resistance to high temperature electronic degradation. It is commonly used as a material for catalyst [6], sensors [7], piezoelectric transducers [8] and photonic devices [9]. In addition, ZnO is a bio-compatible material [10], which makes it an ideal candidate for biological related applications.

ZnO bulk material has been investigated for decades thanks to its piezoelectricity and other properties [11]. ZnO nanostructures, on the other hand, are becoming an increasingly hot topic in nanofield research community [12-17] after carbon nano tubes

(CNTs) [18] and Si NWs [19, 20] lately. Different morpholgies of ZnO nanostructures, including NWs, nanobelts, nanotubes, etc., have been synthesized and characterized (Figure 1.1) [21]. In addition to the fact that these nanostructures share the common properties of ZnO with their bulk equivalents, they exhibit several distinct properties associated with their nanoscale dimensions, which serves as the foundation of the research presented in this dissertation.

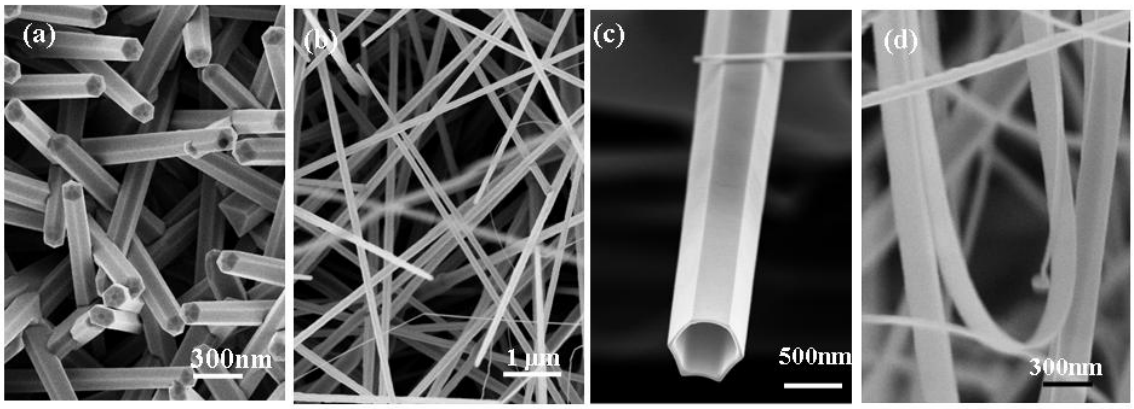

Figure 1. 1 Four types of 1D nanostructure configurations made by ZnO: a) nanorods; b) NWs; c) nanotube; d) nanobelts.

In this dissertation, the main properties of ZnO nanostructure to be utilized are piezoelectric property and high surface-to-volume ratio. Therefore, these two properties will be discussed in detail below.

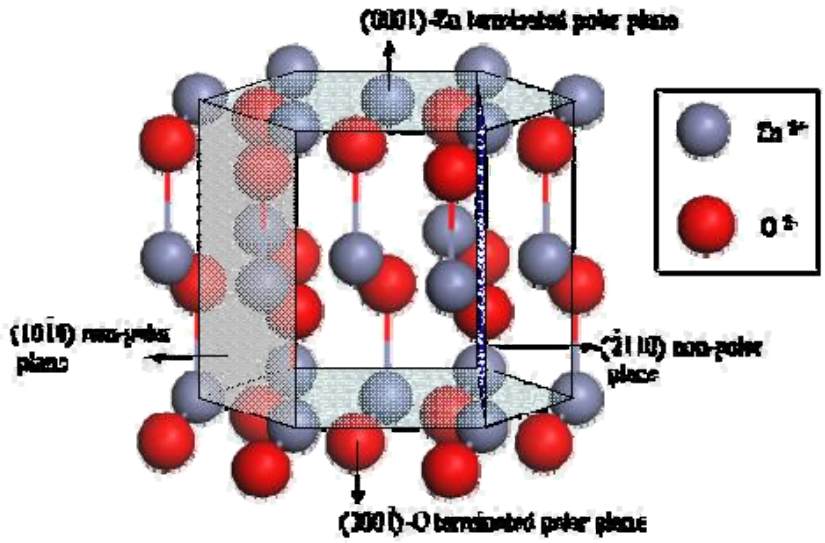

Figure 1. 2 Wurtzite crystal structure of ZnO.

The piezoelectricity of ZnO comes from its crystal structure. ZnO exhibits three types of crystal structures: wurtzite, zinc blend and rocksalt (NaCl). Wurtzite structure, which is shown in Figure 1.2, is the crystal structure of ZnO existed in nature. In wurtzite structure, ZnO is composed of two alternating layers of atoms which correspond to Zn^{2+} and O^{2-}, respectively. Each atom on these two types of layers bonds to each other through four bindings, which is called a tetrahedral structure. Naturally, the formation leads to a non-symmetric structure, both atomically and electrically, which contributes to the spontaneous polarization of ZnO.

Under no pressure, the centers of gravity of negative charges coincide with that of positive charges. Therefore, ZnO material exhibits neutral electric charge when no mechanical deformation occurs to the material. When an external force is exerted on the material, however, the mechanical deformation induced by the external force initiates a displacement between the centers of gravity of positive and negative charges (Figure 1.3). The displacement, which can be considered as a dipole from the electrical charge point of

view, leads to the accumulation of net charges with opposite polarities on the opposite facets of ZnO.

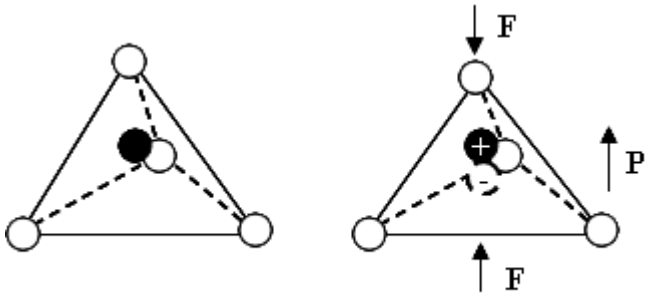

Figure 1. 3 Piezoelectric effect of ZnO.

Piezoelectricity is a native property that is shared by both bulk and nanoscale ZnO. High surface-to-volume ratio, however, is only in connection with nanoscale material. As mentioned above, not only ZnO, but many other nanomaterials, such as Si NWs, have this property as well.

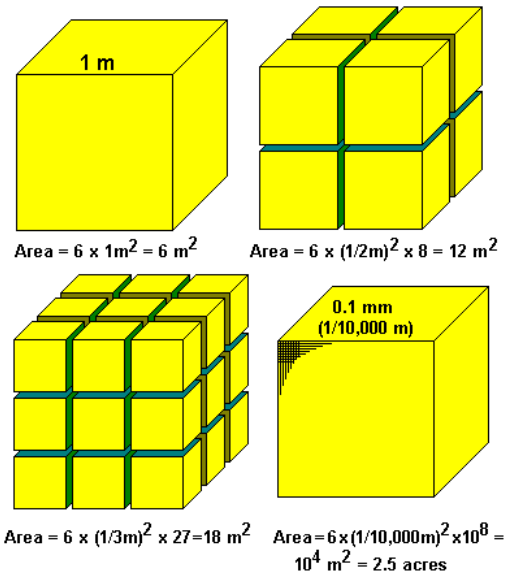

Figure 1. 4 Illustration of the relationship between the volume and the surface area.

To illustrate the relationship between the volume and the surface area, a cube of 1 m^3 is used as an example. The surface area of one 1 m^3 cube is 6 m^2. If the cubicle is cut into eight smaller cubes, the surface area increases to 12 m^2. Similarly, the surface area increases to 18 m^2 if there are 27 cubes while the volume remains the same. Eventually, the surface area becomes an incredible 2.5 acres if the unit cube is 0.1mm by side. From this example, it is obvious that nanostructures have a huge surface-to-volume ratio which far exceeds their bulk counterparts. It is this high surface-to-volume ratio that accounts for many promising applications given by nanostructure materials.

1.1.3 System-on-package Technology

System-on-package (SOP) technology is a new concept developed to solve the integration issues in microelectronic industry, which can be applied to ZnO NW based applications detailed in this research. Today, electronic systems rely mostly on Integrated Circuits (IC) integration (Moore's Law) for performance improvement and cost reduction. But ICs make up only 10-20% of an electronic system size, the remaining 80-90% is typically made up of bulky power sources, heat sinks, passive components and interconnects. These are major bottlenecks for reducing size, cost and power consumption of the system. The SOP technology paradigm provides system-level miniaturization in a package size that makes today's hand-held devices into multi-functional systems, with applications ranging from computing, wireless communications, health care to personal security. The SOP is a system miniaturization technology that ultimately integrates nanoscale thin film and nanostructure components for batteries, thermal structures, active and passive components in low cost organic packaging substrates, leading to microscale and nanoscale modules and systems. This is the

fundamental basis for the SOP concept. In addition to miniaturization, such a concept leads to lower cost, higher performance and better reliability of all electronic systems including energy harvesting and bio-sensor systems that are discussed in this dissertation.

Since SOP technology is system miniaturization in principle, utilizing nanostructure material is a natural consequence to achieve such a goal. ZnO nanostructures, NWs in particular, can be good candidates in integrating with other electronic components to realize special functionality such as energy harvesting and bio-detection capabilities in SOP platform.

1.2 Objective of Thesis and Organization

1.2.1 Objective

As the science and technology advance, researchers are looking for new discoveries as well as better solutions to existing issue to bring our ways of living to a higher standard. In the world of microelectronics, system miniaturization is a key in achieving multi-functional electronic system that keeps up with the level of people's expectations. Moore's Law sets the guidance for the IC size reduction. For most parts of the system, however, such as power and active/passive components, much has yet done to tackle the need of miniaturization. In the processes of technology development, nanoscience and nanotechnology have attracted scientists' attention and turned into one of the most promising technologies that could have a revolutionary impact.

ZnO nanostructures, in particular NWs, have the potential to be one of such revolutionary materials. ZnO is a piezoelectric, transparent and semiconducting material.

With a direct band gap of 3.37eV and large excitation binding energy (60meV), ZnO exhibits near-UV emission, transparent conductivity, and resistance to high temperature electronic degradation. ZnO NWs, with all the properties of bulk ZnO, have unique properties that are distinct to nanoscale materials. All of these make ZnO NWs a very unique material that has potential applications in system miniaturization.

The objective of this research is to investigate and utilize the unique properties of ZnO NWs and apply them to fabricate devices that can be integrated with SOP platform. The key issues to be investigated include:

- Developing techniques to manipulate and align ZnO NWs; developing contact preparation methods to improve the contact conductance for the fabrication of ZnO NW based devices.
- Investigating the oxygen diffusion coefficient in ZnO NWs which serves as the basis for ZnO based sensing applications.
- Fabricating and characterizing SOP compatible ZnO NW based bio-sensors.
- Integrating micro-fluidic system with ZnO NW based bio-sensors and measuring the real-time response of the protein binding event.
- Fabricating and characterizing SOP compatible ZnO NW based nano-generators.
- Investigating various parameters that affect the output characteristics of nano-generators.

1.2.2 Organization

A comprehensive literature review of previous work related to ZnO NWs as well as the state-of-the-art development of ZnO NWs based devices are summarized in chapter 2. A novel technique to align the ZnO NW and improve the contact conductance is

developed in chapter 3. Chapter 4 presents the investigation of oxygen diffusion coefficient in ZnO NWs. ZnO NWs based devices, namely bio-sensor and nano-generator, are developed and presented in chapter 5 to chapter 8. Chapter 5 discusses the fabrication and characterization of ZnO NW based sensors which detect the bio-molecules of interest in non real-time. A real-time, label-free bio-sensor integrated with a micro-fluidic channel is presented in chapter 6. A thin film version of the sensor, which meets the industrial manufacturing requirements, is presented in chapter 6 as well. Chapter 7 and 8 investigates the characteristics of ZnO NW based nano-generators and factors that govern the performances of nano-generators. Finally, chapter 9 summarizes the dissertation and describes the remaining work for future studies.

CHAPTER II
SUMMARY OF PREVIOUS WORK

The work in this thesis is based on many accomplishments that are either done by the students in the same group or described in literature. A comprehensive review of these accomplishments is necessary before going further into the details of this research. Any nanoscale device fabrication starts with the synthesis of the underlying materials. A section is therefore devoted to examine the recent advance of ZnO one-dimensional (1D) material synthesis. Two types of ZnO based devices, pH meters and atomic force microscope (AFM) assisted nano-generators, are described following the review of the material synthesis. PH meters operate under the same principle as that of bio-sensors presented in later chapter; whereas AFM assisted nano-generators establish the fundamentals for the nano-generators that are described in this thesis. Finally, the state-of-the-art development of Si NW based bio-sensors is reviewed for two reasons. Si is a well documented material and its 1D structures are among the most examined 1D materials. The mechanism that governs the operation of ZnO NW bio-sensors and Si NW bio-sensors is the same.

2.1 The Synthesis of ZnO Nanostructures

The synthesis of ZnO nanostructures is one of the more active fields in the research of nanoscience and nanotechnology. Various 1D ZnO materials such as NWs [22], nanobelts [23], nanohelices [24] have been synthesized through a number of

approaches such as the thermal evaporation [14, 25], the laser ablation [26], the template-assisted growth [27], and the sol-gel method [28]. Among these methods, the thermal evaporation is the most widely used method since not only it is a simple setup, but also it produces controllable outcome that is acceptable to scientific research purposes. As a result, many ZnO morphologies, including the ZnO NWs that are used in this work, are synthesized through this simple approach.

2.1.1 Furnace Setup

A single temperature zone furnace is used to synthesize the NWs and other morphologies of ZnO. The setup is shown in Figure 2.1. The synthesis is carried out in an alumina tube in the center of the single temperature zone furnace. The source material, which is a mixture of ZnO and carbon powders, is placed in the center of the tube. The substrate, which could be made from either sapphire or Gallium Nitride (GaN), is placed toward one end of the tube. Cooling water is running constantly at both ends of the tube to keep a stable temperature gradient inside the tube. Before starting the synthesis, the reaction chamber is pumped down to the lowest possible pressure, which is normally $\sim 10 \times 10^{-3}$ Torr, to remove the residual O_2 in the system. The furnace is then heated to the reaction temperature, i.e. 950° C, at a specific heating rate. The ZnO powder, with the assistance of the carbon powder, sublimates under such temperature. Meanwhile, inert gas, such as argon, is introduced into the system at a constant flow rate to bring the pressure in the chamber back to a relatively high value. The inert gas also serves as the carrying gas to carry the sublimated source materialfrom the center of the tube to the substrate, which is at a cooler position. The reaction temperature and the pressure are held constant during the deposition. When the reaction is completed, the furnace is

cooled down to room temperature with the inert gas continuing flowing. More about the furnace setup and the synthesis procedures can be found at Xudong Wang's Ph.D. dissertation [29].

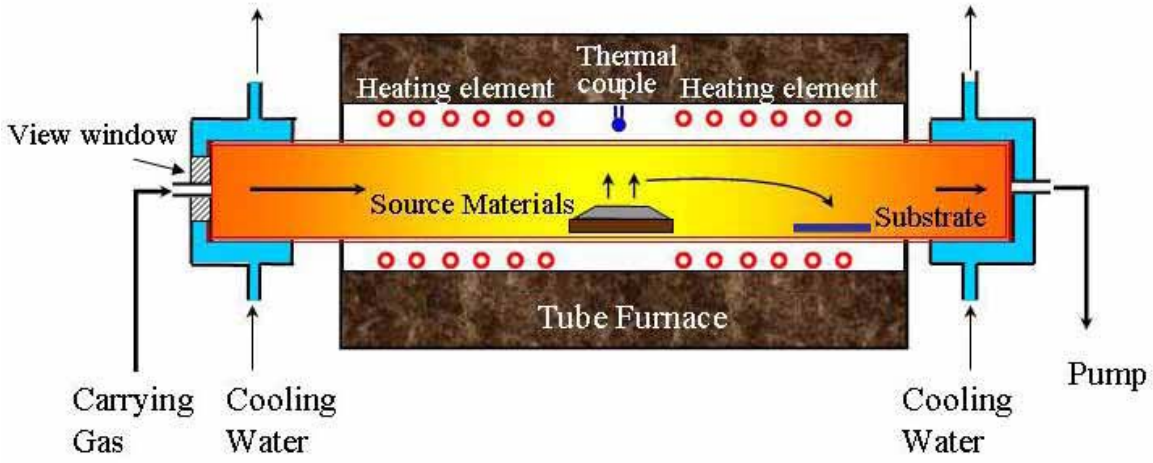

Figure 2.1 The furnace setup of the ZnO NW synthesis.

2.1.2 ZnO Morphologies

In the thermal evaporation synthesis technique, the morphologies of the synthesized ZnO nanostructures are sensitive to the processing parameters, such as the processing pressure, the temperature, the O_2 concentration and the catalyst thickness. Small changes in these parameters could lead to the formation of different nanostructures, as shown in Figure 1.1 in chapter 1. Puxian Gao [21] and Xudong Wang [29] systematically studied the effects of the parameters change to the morphologies of the ZnO nanostructure. It is found that the growth behavior and the product morphology differ dramatically by varying the processing pressure as well as the O_2 concentration in the carrying gas. Figure 2.2 is the SEM images of different growth products with

different processing pressures; and Figure 2.3 presents the effects of the O_2 concentration in the carrying gas on the ZnO morphologies.

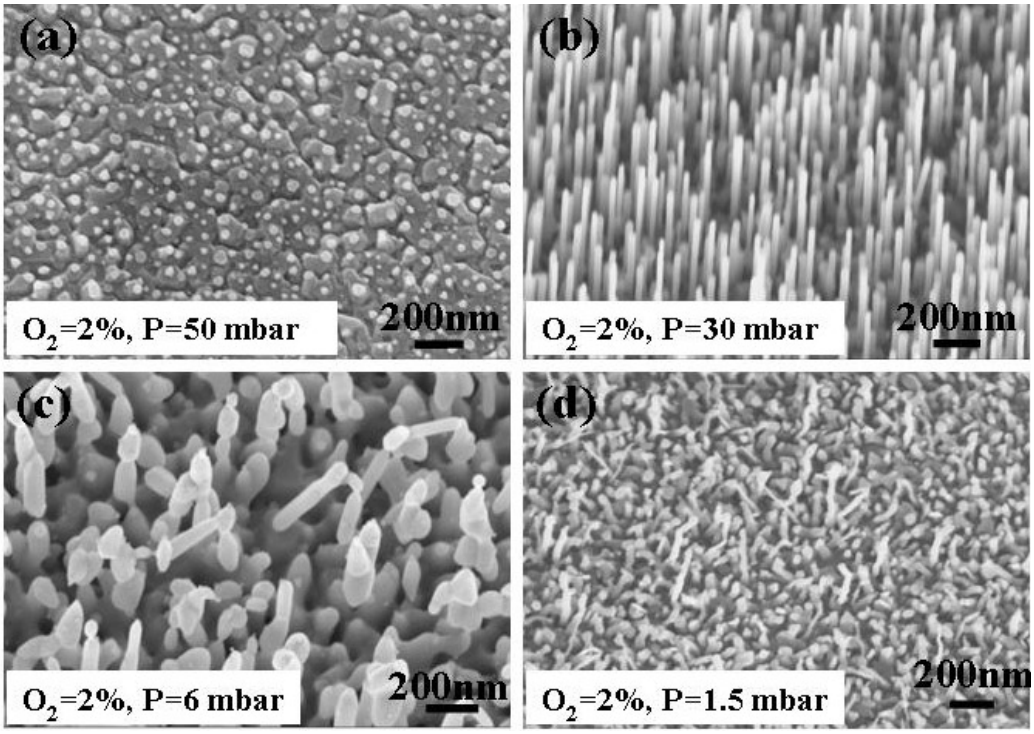

Figure 2.2 SEM images of ZnO NWs grown under four different processing pressures with the same O_2 concentration. (a)50mbar, (b)30mbar, (c)6mbar, and (d)1.5mbar.

The resulting morphologies are strongly dependent on the processing pressure as well as the O_2 concentration. This work paves the way for tuning the synthesis parameters to find the optimal growth conditions for well aligned ZnO NWs that are required in the nano-generator applications.

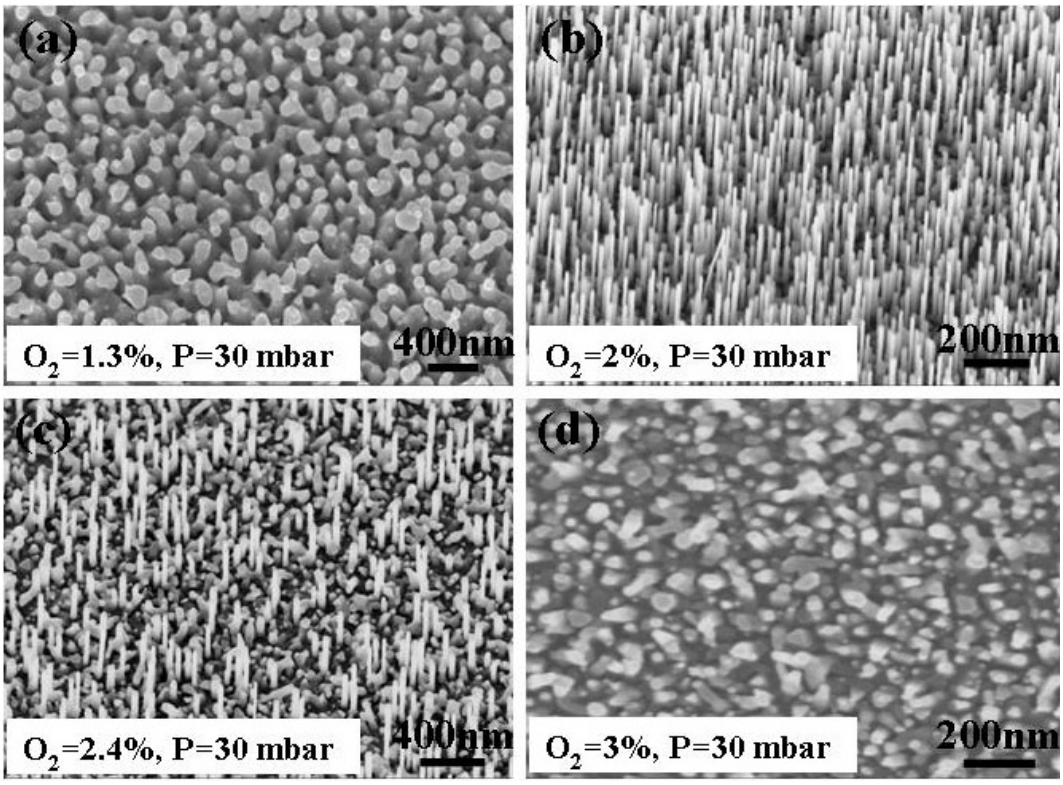

Figure 2.3 SEM images of ZnO NWs grown under four different O2 concentration with the same processing pressure. (a)1.3%, (b)2%, (c)2.4%, and (d)3%.

2.2 ZnO NW-Based Devices

Devices fabrication can be seen as the natural research extension on the existing synthesized ZnO NWs since many properties associated with the ZnO NWs are exciting and too good to miss. There are reports of fabricating ZnO NWs based devices such as gas sensors [30], bio-sensors and field-effect transistors (FETs). As mentioned earlier, the main advantages of the ZnO NWs that are focused in this thesis are piezoelectricity and small dimension. This section will cover the latest development in these two sub-fields.

2.2.1 ZnO NW-Based Field-Effect Transistor

ZnO NWs are uniform 1D nanostructures with confined size effects. ZnO nanobelts, which fall to a special category of NWs with rectangular cross sections, are reported to fabricate FETs. By forming a metal electrode/nanobelt electrical contact and capacitively coupling the nanostructure to a nearby gate electrode, FETs are produced based on the ZnO nanobelts to explore new physical and chemical properties [16].

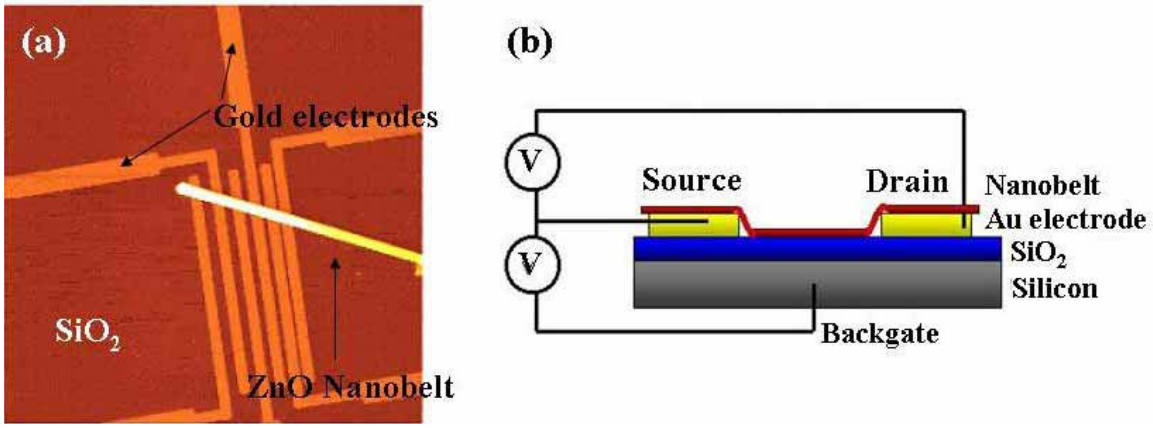

Figure 2.4 (a) An AFM image of an FET built with a single ZnO nanobelt on the gold electrodes; (b) A schematic diagram of the FET device.

The ZnO FETs are fabricated by dispersing the ZnO nanobelts on predefined gold electrode arrays. The SiO_2 gate dielectric thickness is 120 nm; and the back gate electrode is fabricated by evaporating gold on the back side of the substrate. The electrode gaps between the source and the drain electrodes vary from 100 nm to 6 μm. Figure 2.4 (a) shows an FET fabricated with a single ZnO nanobelt according to the design principle illustrated in Figure 2.4 (b).

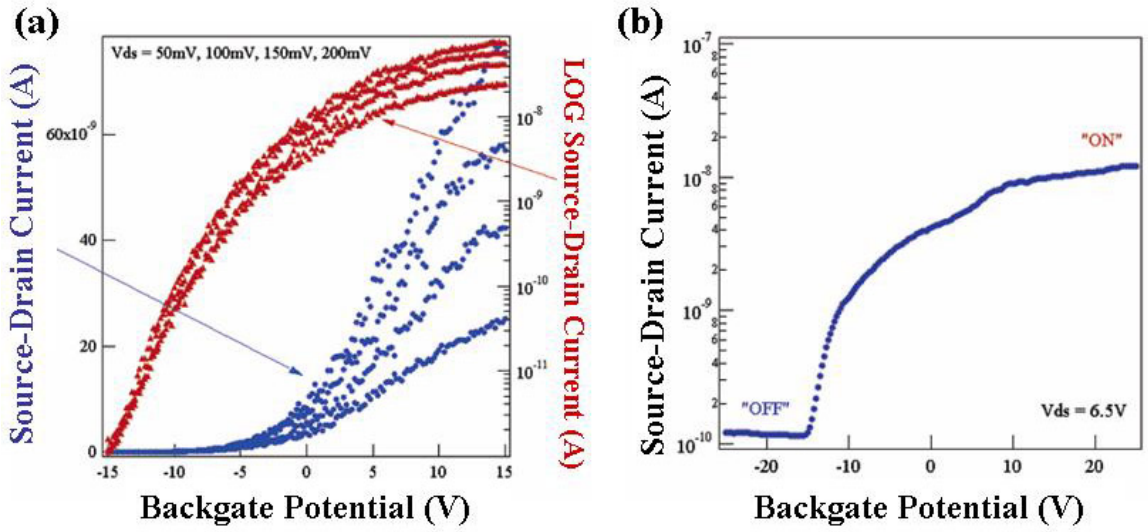

Figure 2.5 (a) The source-drain current versus the gate bias for a SnO_2 FET in ambient environment; (b) The source-drain current versus the gate bias for a ZnO FET in ambient environment.

For comparison purposes, the authors also fabricate SnO_2 FETs based on the same principle. A typical SnO_2 FET pretreated in a 1 atm oxygen atmosphere at 800º C demonstrates a gate-threshold voltage of ~2.5 V, a current switching ratio I(ON)/I(OFF) of nearly 10000, and (ignoring voltage drops at the Ti contacts) a peak conductivity of 8.14 $(\Omega \cdot cm)^{-1}$, as shown in Figure 2.5 (a). The measured conductivities range from 4 to 15 $(\Omega \cdot cm)^{-1}$. The typical leakage conductance between the electrodes under ambient condition is between 20 and 80 pS and gate-bias independent. In most cases, the switching ratios of the FETs are limited by this background conductivity. From an analysis of the transconductance, dI/dVg, for gate biases above the threshold bias, the electron mobility of an n-type field-effect transistor can be estimated if the geometry of the device is known. Without subtracting the voltage drops at the contacts, the electron mobility in the SnO_2 nanobelt is estimated to be ~35 $cm^2/V \cdot s$ from the analysis of Figure

2.5 (a). Other measured SnO_2 nanobelt FETs exhibit electron mobility ranging from 10 to 125 $cm^2/V \cdot s$.

A typical ZnO FET shows a gate threshold voltage of ~15 V, a switching ratio of nearly 100, and a peak conductivity of 1.25×10^{-3} $(\Omega \bullet cm)^{-1}$, as shown in Figure 2.5 (b).

2.2.2 ZnO NW-Based pH Meter

ZnO NWs have huge surface-to-volume ratios, which makes them ideal candidates of sensor applications. B. S. Kang et al. [31] report using this property of ZnO NW to fabricate pH meters.

The ZnO NWs used in this work are synthesized through molecular beam expitaxy (MBE), which is reported elsewhere [12]. After the synthesis, the NWs are released from the substrate by sonicating in ethanol. The NWs are then transferred to thw SiO_2 coated Si substrates. E-beam lithography and a typical lift-off process are employed to pattern the sputtered Al/Pt/Au electrodes which make contacts with both ends of a single NW. The separation of the electrodes is 3.7 mm. Au wires are then bonded to the contact pads for current-voltage (I-V) measurements. An integrated microfluidic channel made of SYLGARD™ 184 polymers from DOW CORNING is bonded to the device. Figure 2.6 illustrates the schematic of one such device and its SEM image.

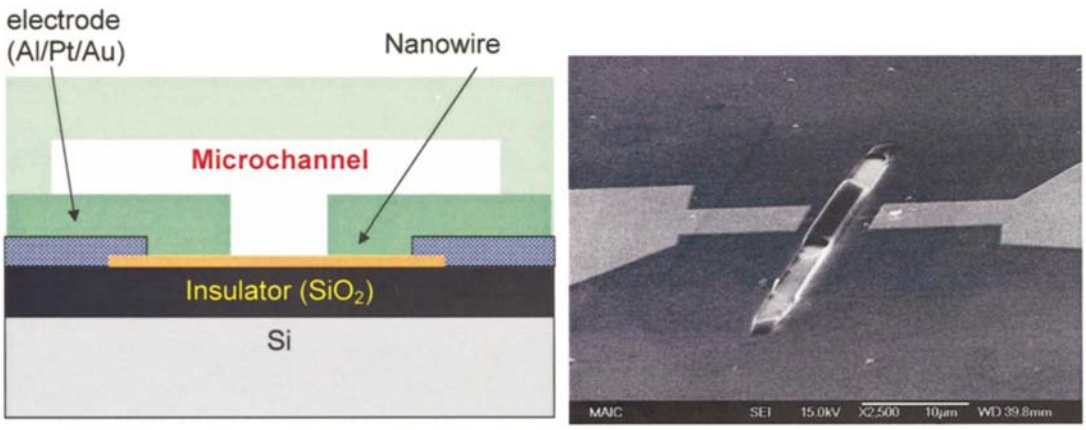

(a) (b)

Figure 2.6 The schematic (a) and the SEM image (b) of a ZnO NW pH meter with an integrated microfluidic channel.

The device is subsequently exposed to a series of solutions for 60 seconds with pH is from 2 to 12. The current of the device is measured against time during the process, which is shown in Figure 2.7 (a). The corresponding conductance of the device during the exposure to the solutions is shown at Figure 2.7 (b). The current is significantly reduced upon the exposure to the polar liquids as the pH is increased. The pH value is varied from 2 to 12. The data in Figure 2.7 show that ZnO NW-based pH meters are sensitive to the concentration of the polar liquid and therefore could be used to differentiate between liquids into which a small amount of another substance is present. The conductance of the NW is higher under UV illumination but the percentage change in conductance is similar to the case without UV illumination.

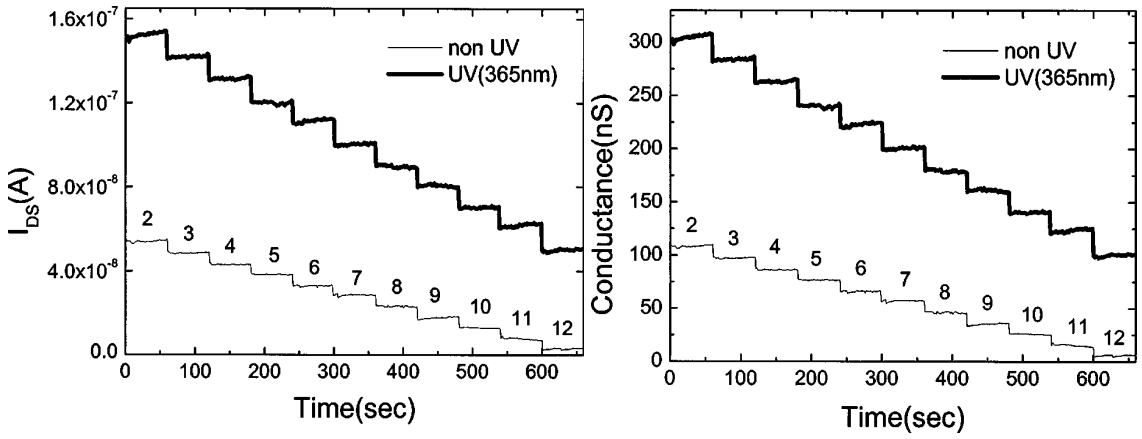

(a) (b)

Figure 2.7 The current (a) and the conductance (b) change of a ZnO NW-based pH meter with respect to time with pH from 2 to 12 at V=0.5V.

2.2.3 AFM Assisted Nano-Generator

The previous two examples utilize the small dimension and the high surface-to-volume raito properties of ZnO NWs. These two properties are common to all 1D nanostructures. The following application, however, is based on the piezoelectric property of ZnO NWs, which is unique to piezoelectric materials.

The concept of the nano-generator is developed based on the coupling of piezoelectric and semiconductive properties of ZnO as well as the formation of a schottky barrier between the metal and the ZnO NW [32]. Figure 2.8 (a) and (b) show the ZnO NWs that are used in the experiment. The NWs are grown on a c plane-orientated α-Al_2O_3 substrate using Au catalyst by the thermal evaporation method mentioned earlier in this chapter. The epitaxial relationship between the ZnO and the α-Al_2O_3 substrate allows the growth of a thin, continuous layer of ZnO at the bottom of the substrate. This ZnO thin film serves as a bridge between the NWs and the metal electrodes for the

electron transports. Transmission electron microscope (TEM) (Figure 2.8 (b) insets) images confirm that the as-grown ZnO NWs are single crystal structures with a small hemisphere, if not free, of Au.

Figure 2.8 (c) illustrates the experiment setup and the procedures of generating electric signal by deforming a ZnO NW with a conductive AFM tip. The AFM tip is coated with Pt to form a schottky contact with the ZnO NW. The base of the NW is grounded and an external load of R_L is applied, which is much larger than the resistance R_I of the NW. The AFM is operating in contact mode.

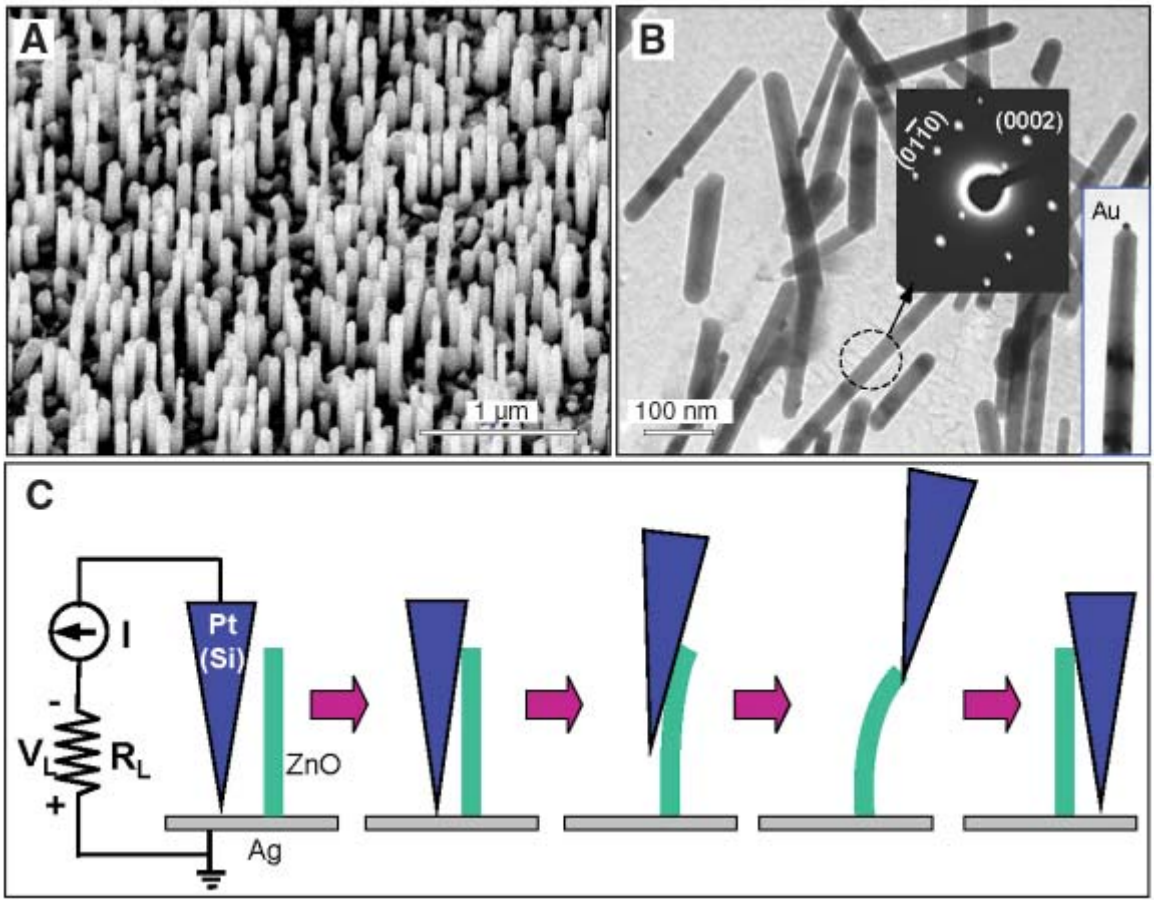

Figure 2.8 The SEM (a)and TEM (b) images of the grown ZnO NWs; (c) The experiment procedure to generate the electric signal.

The physical principle for creating the discharge energy arises from how the piezoelectric and semiconductive properties of ZnO are coupled. For a vertical, straight ZnO NW (Figure 2.9 (a)), the deflection of the NW by an AFM tip creates a strain field, with the outer surface being stretched (positive strain ε) and the inner surface compressed (negative ε) (Figure 2.9 (b)). An electric field E_z along the NW (z direction) is then created inside the NW volume because of the piezoelectric effect. The piezoelectric field direction is parallel to the z axis (NW direction) at the outer surface and antiparallel to the z axis at the inner surface (Figure 2.9 (c)).

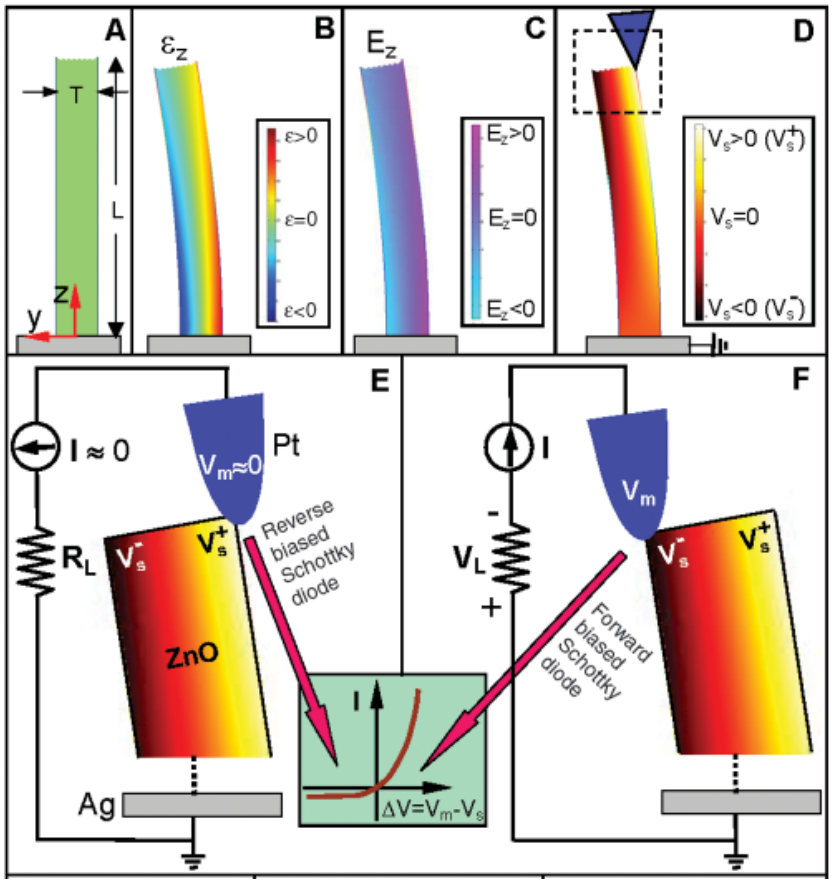

Figure 2.9 (a) The schematic definition of a NW and the coordination system; The ε (b), Ez (c) and Vs (d) distributions of a NW under bending; the current accumulation (e) and the discharge (f) model of the nano-generator.

The contacts at the top and the bottom of the NW are nonsymmetrical. The bottom contact is the ZnO thin film with Ag paste. The effective contact is therefore between the ZnO thin film and the Ag, which is an ohmic contact. At the tip of the NW, the coated Pt has a work function of ~6.1 eV; while the ZnO has a work function of ~5.2 eV [33]. The Pt-ZnO contact is a schottky contact, and dominates the entire transport process. Two distinct transport processes occur across the contact when the AFM tip is in contact with the compressed side and the tensile side of the semiconductor ZnO NW. This is because of the negative potential at the compressed side and the positive potential at the stretched side of the NW. During the scanning, the AFM conductive tip that induces the deformation is in contact with the stretched surface that has a positive potential (Figure 2.9 (d) and (e)). So the Pt-ZnO interface is negatively biased, which is a reverse-biased Schottky diode for an n-type ZnO (Figure 2.9 (e)). As a result, little current flows across the interface. Subsequently in the scanning process, when the AFM tip is in contact with the compressed side of the NW (Figure 2.9 (f)), the Pt-ZnO interface is positively biased. The Pt-ZnO interface is a positively biased schottky diode; and it produces a sudden increase in the output electric current, which is the observed electrical discharge.

2.3 Si NW-Based Bio-Sensor: State-of-the-art Development

One of the goals in this dissertation is to fabricate ZnO NW-based bio-sensors to detect biological macromolecules. Unfortunately, not much has been done utilizing ZnO as the platform. Research of employing Si NW to detect bio-molecules, however, is

intensively investigated and reported. Since the underlying mechanism of utilizing ZnO NW and Si NW as bio-sensors is fundamentally identical, a brief review on the Si NW bio-sensors is presented in the following section. Please keep in mind that an additional advantage of ZnO to Si is the bio-compatibility of ZnO, which is still arguable in the case of Si [34].

Biological macromolecules, such as proteins and nucleic acids, are typically charged in aqueous solution, and therefore can be detected readily by semiconductive NWs. A Si NW-based device, as illustrated in Figure 2.10 (a) can be configured into a bio-sensor, where specific sensing is achieved by linking a recognition group to the surface of the NW.

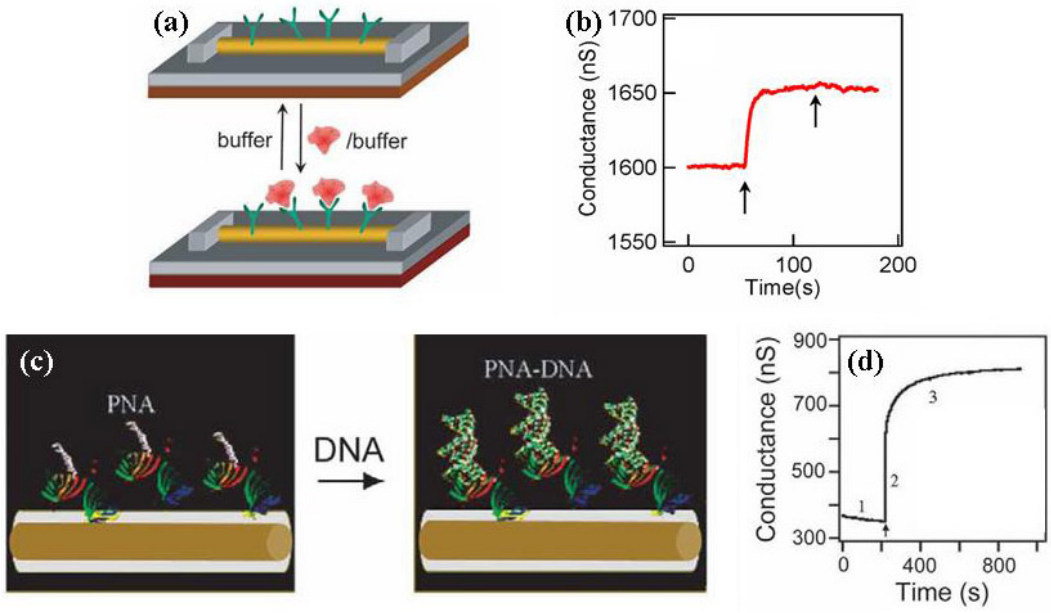

Figure 2.10 (a) The schematic of a Si NW FET configured as a bio-sensor with antibody receptors before and after the binding of the target proteins; (b) The plot of the conductance versus time for a biotin-modified Si NW FET showing the response to the binding of the streptavidin; (c) The schematic of a PNA modified Si NW FET before and after the duplex formation with target DNA; (d) The conductance plot of a Si NW FET DNA sensor where the arrow corresponds to the addition of the DNA sample [29].

Cui and his co-workers [5] demonstrate the detection of proteins in real time with p-type Si NW-based bio-snesors. The surfaces of the NWs are functionalized with molecules biotin, which bind to the protein streptavidin selectively. When the analyte containing the streptavidin is delivered to the NW sensors with modified surfaces, it is found that the conductance increases rapidly to a constant value. This conductance value is maintained after the addition of pure buffer solution, as shown in Figure 2.10 (b). These results come from the facts that streptavidin are charged under the pH value of interest, and the dissociation rate of the streptavidin-biotin system is very small.

More recently, Si NW FETs are investigated as sensors for the detection of single-stranded DNA [35], where the binding of this negatively charged polyanionic macromolecule to the p-type NW surfaces leads to an increase in the conductance. Recognition of the DNA target molecules is carried out with a complementary sequence of a single-stranded material, such as the peptide nucleic acids (PNAs) illustrated in Fig. 2.10 (c). Studies of the p-type Si NW devices modified with a PNA receptor designed to recognize wild type versus the DF508 mutation site in the cystic fibrosis transmembrane receptor gene show that the conductance increases following the addition of a 60 fM wild-type DNA sample solution, as shown in Fig. 2.10 (d). The sequence specificity in these experiments is a critical first step toward the development of the NW devices for genetic-based disease detection.

2.4 Chapter Summary

A comprehensive literature review related to the ZnO nanostructures is presented in this chapter. Devices based on ZnO NWs, such as FET, pH meter, and AFM assisted nano-generator, are discussed in detail. Finally, the state-of-the-art development in the NW based sensors field is reviewed.

CHAPTER III

ALIGNMENT AND CONTACT PREPARATION OF ZNO NW DEVICES

The traditional microelectronic industry employs a top-down approach, where the device fabrication is achieved through typical processing steps such as deposition, etching, and ion implantation. There are no issues of aligning and manipulating nanostructures during these processing steps. However, in a bottom-up approach, where the synthesis of nanostructures is done before the fabrication of devices, successful device fabrication starts with the manipulation of 1D nanostructures. One of the more widely used techniques to manipulate and fabricate devices with 1D nanostructures is electron-beam lithography [36, 37]. However, accessibility to such unusual equipment is limited. In this chapter, two manipulation methods that are less dependent on expensive equipment are presented. The methods to reduce the contact resistance are also discussed in detail. The work in this chapter paves the way toward the fabrication of ZnO NWs-based devices, particularly in a bio-sensing application.

3.1 Alignment of ZnO NWs

In this section, two alignment methods, dielectrophoresis and micro-manipulation, are examined. Their advantages and disadvantages are compared. A conclusion is drawn based on the specific application of the bio-senor fabrication.

3.1.1 Dielectrophoresis

Electrophoresis (EP) and dielectrophoresis (DEP) are widely used separation techniques in biological applications [38]. EP employs the fact that many biological molecules have charges in their natural forms. Therefore, these molecules tend to move under the electric field. DEP, however, works differently. DEP's target molecule is neutral in charge. Under the electric field, there is an induced dipole on the molecules due to the different dielectric constants between the target molecules and the medium. These molecules move according to the gradient of the external electric field. Figure 3.1 explains the difference between and EP and a DEP.

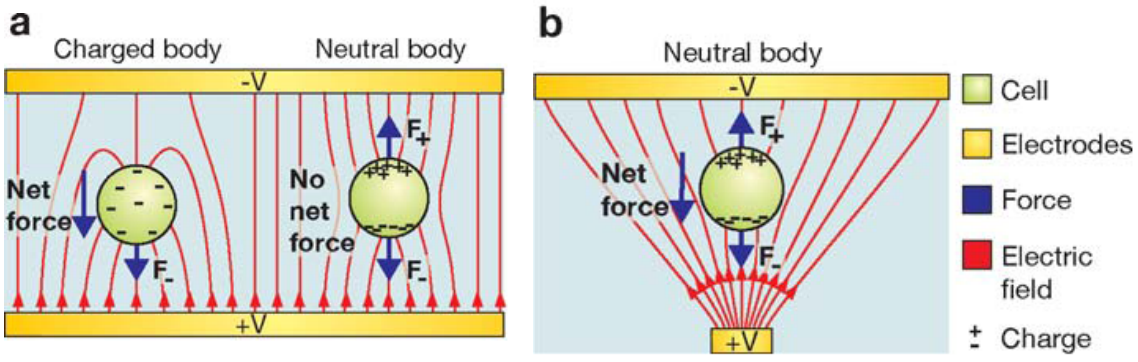

Figure 3.1 EP and DEP. (a) Charged particle (left) feels the net force in a uniform electric field, whereas neutral particle (right) feels no net force; (b) There is a net force applied to a neutral particle in DEP under non-uniform electric field. [38]

Quantitatively speaking, the net force can be expressed as

$$F_{dep} = p \cdot \nabla E \quad , \tag{3.1}$$

where F_{dep} is the dielectrophoretic force induced by the external electric field, p is the particle's dipole moment, and ∇E is the gradient of the external electric field.

To achieve the maximum dielectrophoretic force on certain particles, maximizing the gradient of the electric field is the key.

Borrowing the ideas from colleagues working in bio-fields, many researchers have reported using similar techniques to successfully align nanostructures according to the applied electric field [39, 40]. Several devices have been fabricated using this method [41, 42]. The work presented here mainly involves optimizing the electrode shape to maximize the gradient of the electric field along certain directions.

The shape of the electrodes plays an important role in determining the gradient of the electric field at specific locations. Figure 3.2 illustrates the difference between the electric field strength of a pair of rectangular-shaped electrodes and the strength of a pair of circular-shaped electrodes using COMSOL^{TM} simulator.

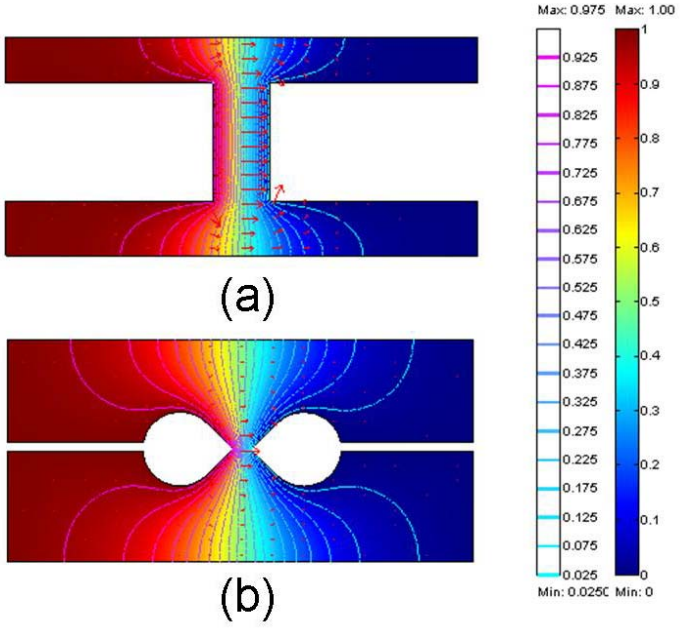

Figure 3.2 Normalized electrical field strength distribution of rectangle electrodes (a) and circular electrodes (b). Red color represents positive potential while blue represents ground. The length of arrows indicates the electrical field intensity at the local position. [43]

To align the NWs at the desired position, maximum electrical field intensity is required at a specific position (tip in this case), while minimum evenly distributed field intensity is required elsewhere. As such, the electric field distribution results in a higher possibility of the NWs aligning across the electrodes.

Once the design of the electrodes is decided, the next step is to fabricate the electrodes. The electrodes are fabricated in a Class 1000 cleanroom by a typical lift-off process. A <100> P-type Si wafer with the resistivity of ~0.001 Ohm·cm^{-1} is thermally oxidized for ~1 hour at 1000° C. As a result, a thin layer of SiO_2 ~100 nm is formed on the surface of Si wafer. AZ5124 photoresist is spin coated at 3000 rpm for 30 seconds. The patterning of the electrodes is accomplished through a Karl Suss MJB-3 mask aligner. After developing, the wafer is coated with a Ti/Au layer or a Ti/Al layer, both of which are 2/200 nm thick. Finally, the AZ-400T photoresist stripper is used to finish the lift-off process. Figure 3.3 shows the optical images of the fabricated electrodes obtained by a Nikon Eclipse L150 optical microscope.

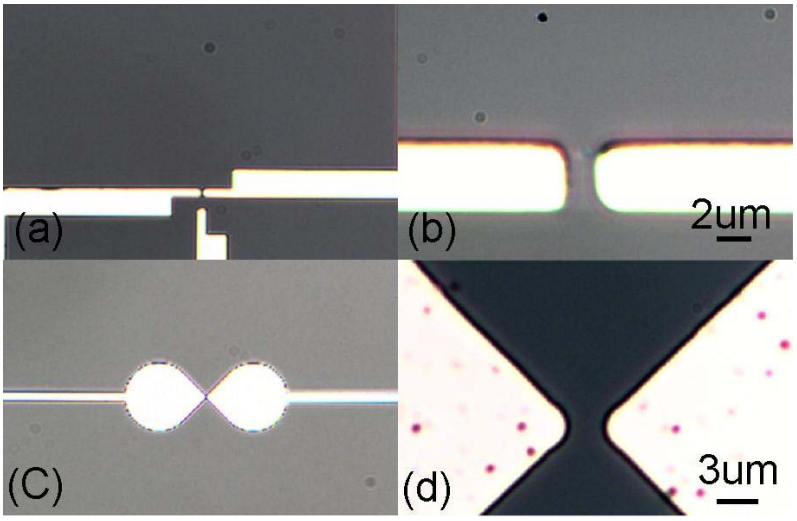

Figure 3.3 Optical images of as-fabricated electrodes. (a) and (b) are rectangle electrodes; (c) and (d) are circular electrodes. The third electrode in (a) is for other experiments.[43]

The DEP alignment is performed with an SRS DS345 synthesized function generator and two Cascade MH2-B probes. A voltage with certain frequency is provided to the electrodes through the probes. The ethanol solution that contains NWs is pippetted to the electrodes. It is found that the voltage of 5V and the frequency of 1MHz give the best results. The electrodes are inspected under SEM after drying.

Figure 3.4 shows aligned NWs on different pairs of electrodes. Generally, in terms of the success of alignment, the electrodes with optimized shape give a better yield than the un-optimized counterparts in terms of the success of alignment (Figure 3.4 (a, b)). For example, tiny misalignment occurs in un-optimized electrodes (Figure 3.4 (b)), which is barely seen in optimized ones (Figure 3.4 (a)). It is worth noting, however, that the NWs are not perfectly aligned across the electrodes, such as illustrated in Figure 3.4 (a). They are not identical to one another either. This is because of the random nature when going into nanoscale.

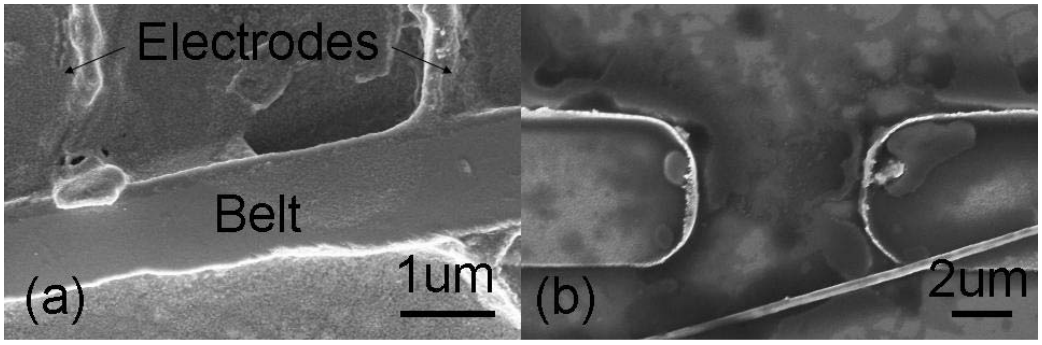

Figure 3.4 SEM images of (a) well aligned NW across circular electrode and (b) misaligned NW on rectangle electrodes.[43]

3.1.2 Micro-manipulation

Comparing with other techniques, aligning ZnO NWs through DEP technique has the advantage of ease to use, convenience and relative low cost. However, the drawbacks are obvious. As shown in the Figure 3.4, the surface of the aligned NW is covered by organic residue that could potentially interfere with the measurement. Moreover, the controllability is not excellent either, and it could be a problem when trying to explore multiplexed sensing scenario where multiple NWs alignment are required. Therefore, in this section, a new way to manipulate ZnO NWs by integrating the alignment with a contact preparation method is presented.

This technique involves an MM3A-EM micromanipulator with NanoControl control electronics from Kleindiek^{TM}. This micromanipulator is integrated inside a Nova 3D 200 focused ion beam (FIB) system from FEI^{TM}. The working mechanism of the FIB will be introduced later in the chapter. This section focuses on using the micro-manipulator only.

Figure 3.5 Images of micromanipulator and control electronics from KleindiekTM. (Courtesy of kleindiek nanoteknik)

Figure 3.5 is an image of the micromanipulator from the company website. Through the controller, the micromanipulator can move mechanically in large distances whenever desired. It can also move piezoelectrically with a resolution down to 5 nm. When working with 1D nanostructures like ZnO NWs, the manipulator is equipped with a tungsten tip with a diameter of ~200 nm. The broad range of the movement, as well as the capability of precise location, provides an excellent opportunity to manipulate individual ZnO NW from the growth substrate to the desired location with high precision and selectivity.

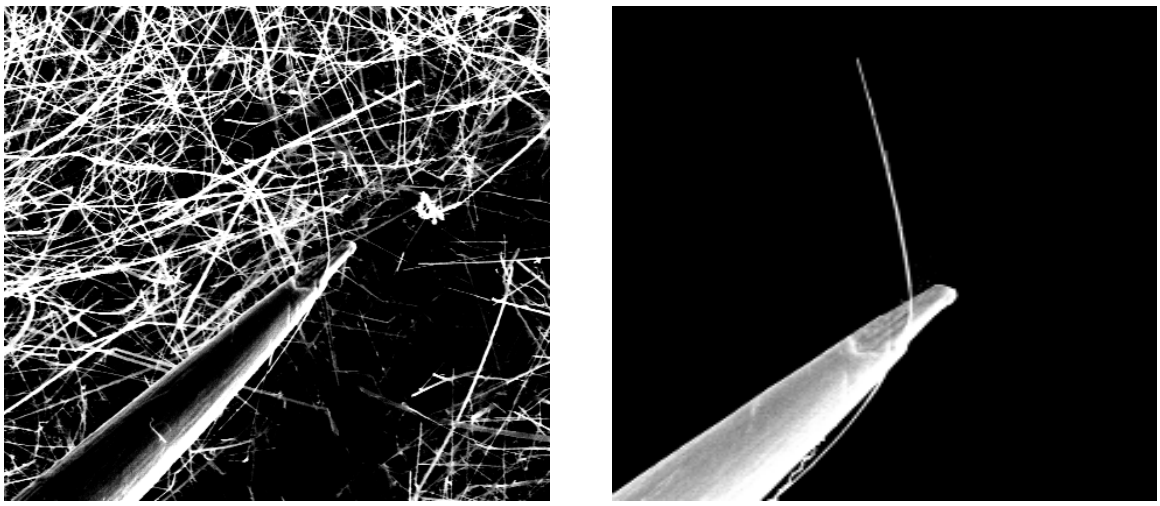

Figure 3.6 (a) SEM images of ZnO NW pick up and (b) enlarged image of the tip of the manipulator.

Figure 3.6 (a) is taken when a ZnO NW is being picked up from the growth substrate. As shown in Figure 3.6 (b), the NW tends to stay with the tip when the tip moves away from the growth substrate because of the electrostatic force. After picking up the desired NW, the tip is moved away from the substrate and placed in close proximity with the electrodes. During this process, necessary alignment procedures are carried out to ensure the NW and the electrodes are along the same direction. Pt is subsequently deposited on both sides of the NW, not only serving as the anchoring point, but also and more importantly, serving as the medium to reduce the contact resistance. Figure 3.7 illustrates this process.

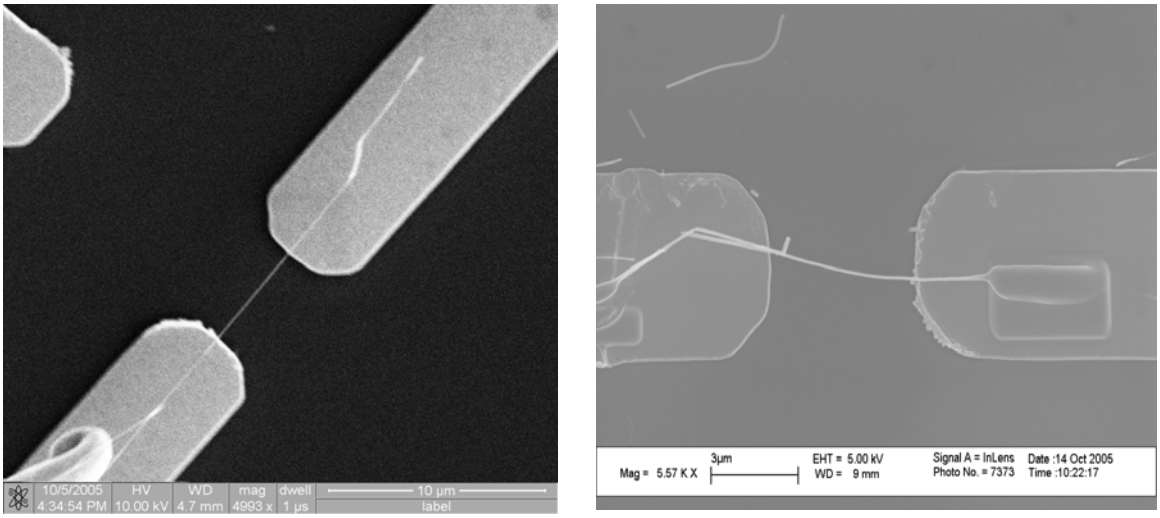

Figure 3.7 (a) A SEM image of the manipulator in close proximity with the electrodes and (b) a SEM image of a NW on the electrodes after the Pt deposition.

The main advantage of this approach is that there is no contamination of the NW from the organic residue. The controllability is also much better compared with the DEP approach. As we will see later in this chapter, the contact resistance after the Pt deposition is negligible; whereas it is large in the case of the DEP approach. However, the one-NW-at-a-time approach is low in efficiency and has difficulty applying to a large-scale manufacturing.

3.2 Contact Preparation of ZnO NW Based Devices

The contact between the ZnO nanostructures and the underlying metal electrodes is one of the more important issues in turning the as-synthesized nanostructures into practical devices. Depending on the work function of the metal, the contacts could be either schottky [44, 45] or ohmic [17, 45-47]. Due to the nature in our approach, it is impossible to realize ohmic contact by depositing Al or other metals, which have similar work functions as ZnO, on top of the ZnO NWs. Therefore, alternatives have to be

considered when dealing with the contact issue. In this section, two methods are discussed. The first method is to anneal the device at an elevated temperature; while the second is to deposit Pt using FIB during the manipulation process.

3.2.1 Annealing

Au is an excellent choice for the contact electrode because of its stability in the atmosphere. It is suitable for applications where the electrodes are required to be exposed in air. It is well known that the undoped ZnO and the Au forms a schottky contact, which exhibits a rectified current behavior [17, 47]. The work function of Au is 5.1 eV, and our previous work suggests that the 1D ZnO nanostructure has a work function of ~5.2-5.3 eV [33], which is larger than that of thin film ZnO (4.5 eV) [48]. It is therefore expected that the contact between the ZnO NWs and the Au electrodes is a weak schottky contact. To reduce the contact resistance, the aligned samples are annealed at 300º C and 500º C for 1 minute and 10 minutes, respectively. An SRS DS345 synthesized function generator and a Keithley 6485 picoammeter are used to generate and measure the voltage and the current, respectively. An NI BNC-2120 card is used to acquire the measured data. After comparison, it is found that annealing at 500º C for 1 minute gives the best result. Figure 3.8 illustrates this difference on current-voltage (I-V) behaviors. It is clear to see the resistance after the annealing decreases dramatically. We suspect a poor contact is the main reason for the large resistance upon the alignment of the NWs. This poor contact might be caused by a point contact or the organic residue frpm the DEP alignment, since it is unlikely that the Au and the ZnO NW forms an intermetallic compound at such temperature. After the annealing, the poor contact is improved to some extent due to the effect of the elevated temperature. In addition, the I-

V curve after the annealing exhibits a weak rectification, which is consistent with the reported data and the small work function difference between the Au and the 1D ZnO nanostructures.

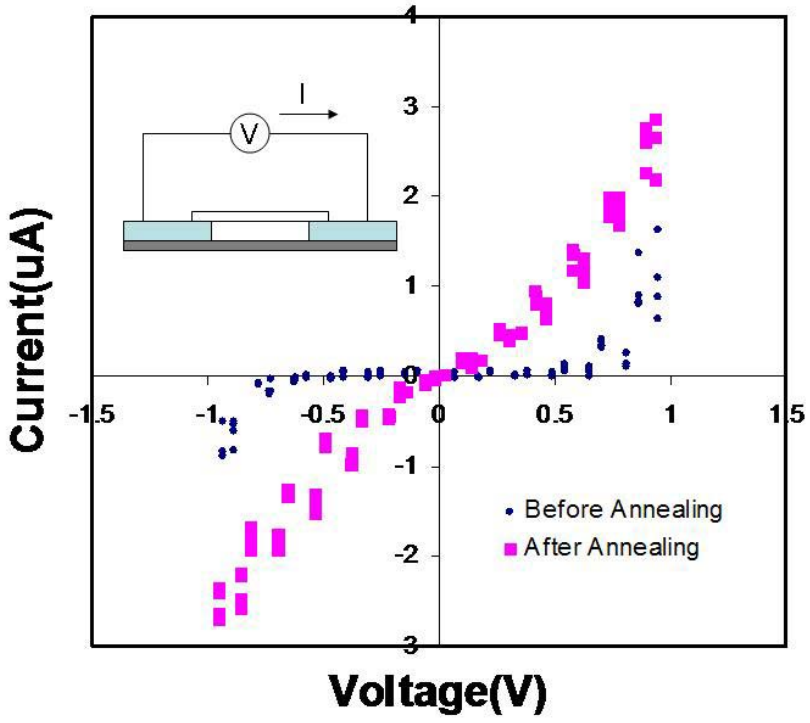

Figure 3.8 I-V characteristics of aligned sample before and after anneal. Inset shows the measurement setup.

3.2.2 Platinum Deposition by Focused Ion Beam

There are several techniques available for making the contact and immobilizing the NWs [36, 37, 49]. Among these methods, e-beam lithography is the most widely used approach. However, e-beam lithography, which requires precise control, is not well suited for NW based applications where NW dispersion is a random process. In addition, the spin coating of the e-beam photoresist introduces organic residue that will contaminate the NW surfaces. The contamination could deteriorate the sensing

performance of NWs-based bio-sensors. Therefore, direct Pt deposition is chosen as the preferred approach in this thesis.

As mentioned in the first section of this chapter, Pt deposition is used to immobilize an individual NW during the NW transfer and manipulation process. More importantly, however, the deposited Pt serves as the medium between the ZnO NW and the Au electrodes. It is found that the contact between the Au electrodes and the ZnO NW is ohmic after Pt deposition [50]. In the section, the FIB system is introduced first. Measuring data as well as a proposed mechanism on the formation of the ohmic contact is presented following the introduction of the FIB.

A FIB system is similar to a SEM that both the instruments are used to take images of the objective of interest under inspection. The difference, however, is that instead of using focused electrons beam to image the sample, FIB uses a focused beam of gallium (Ga) ions. The reason Ga is chosen is because that Ga is easy to build a liquid ion metal source (LIMS). In a Ga LIMS, Ga metal is in contact with a tungsten needle which serves as the emission gun. When the tungsten needle is heated, the Ga wets it, and a huge electric field causes the ionization and field emission of the Ga atoms. Figure 3.9 is the image of the FIB used in this work.

Figure 3.9 Nova Nanolab 200 FIB system. (Courtesy of FIB^{2}Center, Gatech)

Unlike the SEM, the FIB is inherently destructive to the sample, due to the high energy of the Ga ions. When the Ga ions strike the specimen, they will sputter atoms off the surface as well as go implanted into the first few atomic layers of the sample. However, the destructive nature of the high energy Ga ions can also be used to deposit metals, such as Pt.

The deposition, which is called an ion beam induced deposition, is working in the following manner. The Trimethyl-methylcyclopentadienyl-platinum precursor gas is injected into the chamber and chemisorbed on the surfaces of the specimen, ZnO NWs in this case. By scanning the desired area where the deposition is required, the precursor gas dissociates into volatile components and Pt. The volatile components are pumped out of the chamber while the Pt remains on the surface as the deposited metal. By scanning both ends of an individual ZnO NW, Pt is deposited to immobilize as well as to improve the contact between the NW and the underlying Au electrodes.

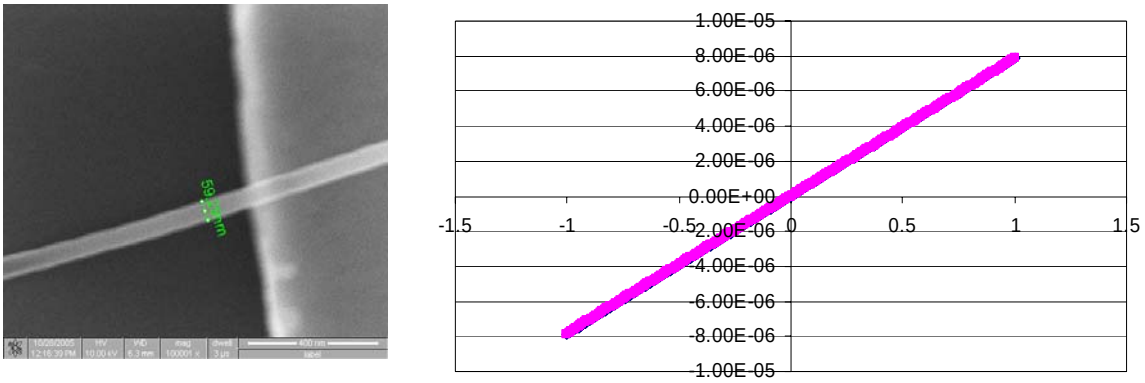

(a) (b)

Figure 3.10 (a) SEM image of an aligned ZnO NW and (b) I-V characteristics of the ZnO NW.

To investigate the contact resistance, the I-V characteristics of a Pt deposited device are measured. In theory, the contact between the ZnO and the Pt is shcottky contact due to the work function difference (Pt ~ 5.6eV and ZnO nanostructure ~5.2eV). However, the measurement indicates that the contact is ohimc, as shown in Figure 3.10 (b). Therefore, the contact resistance can be neglected in this case. The deposited Pt is dissociated from metalorganic precursor and different from pure Pt structurally. It is suspected that the work function of the deposited Pt is different from that of pure Pt.

Considering all the advantages and the disadvantages of these two alignment and contact preparation techniques, the manipulator and the FIB assisted Pt deposition approach is chosen for the fabrication of the devices of interest in this dissertation. Although it is a low output approach, the quality of each fabricated device is guaranteed for the bio-sensing application.

3.3 Chapter Summary

Two alignment methods are discussed and evaluated based on their advantages and disadvantages. In addition, two approaches to prepare and reduce the contact resistance are presented. Annealing the ZnO NW devices could improve the contact to some extent. However, the DEP method associated with the annealing approach leaves organic residue on the ZnO NW surfaces, which could potentially interfere with the sensing experiment. Therefore, the second approach, which integrates the micro-manipulation and the FIB assisted Pt deposition is chosen based on the requirements of the application specified in this thesis, although it has the disadvantage of being a low throughput comparing with the DEP approach.

CHAPTER IV
OXYGEN DIFFUSION IN ZNO NANODEVICES

As discussed in earlier chapters, ZnO nanostructures are very important materials. They can be fabricated into many devices ranging from field-effect transistors [51], gas sensors to pH meters. One of the important factors that need to be investigated for these applications is the oxygen diffusion behavior in the nanostructures. As the oxygen diffusion behavior affects the performance of NWs based sensors significantly [50]. This study will be helpful in predicting the stability of the devices made from ZnO NWs and similar structures. This chapter starts with the fabrication process of the device under test, followed by the measurement results. A finite element analysis is established based on the equation that governs the oxygen diffusion behavior. Finally, the oxygen diffusion coefficient is derived from the extrapolation of the measurement data.

4.1 Device Fabrication

The ZnO NWs are synthesized through the high temperature thermal evaporation method as described in chapter 2. The synthesized ZnO NWs have a diameter of ~ 200 nm and length of up to 5 um. According to Pan et al. [23], the ZnO NW is wurtize (hexagonal) structure with a lattice constant of 3.249 Å and c of 5.206 Å. It is grown along either the $[0001]$ or the $[01\bar{1}0]$ direction. The synthesized ZnO NWs are then transferred from the Al_2O_3 substrate to the prepatterned Au electrodes via the micro-manipulation method described in chapter 3. The prepatterned Au electrodes are

fabricated through a typical lift-off process on a 100 nm Si_3N_4 layer that is deposited on a Si wafer using plasma enhanced chemical vapor deposition (PECVD). The details of the experiment are as follows. SiH_4 and NH_3 gases, which act as the precursors of the reaction, are plasmonrized at 30 kV and 300° C. As a result, Si_3N_4 is deposited on the surface of the Si wafer at a rate of 50 Å/min. Then, AZ5214-E photoresist is spun on and exposed under the UV light with an MJB-3 mask aligner. After developing, a Ti/Au layer with the thickness of 20/200 nm is deposited through the e-beam evaporation to form the Au electrodes. Pt is deposited during the manipulation process as described in chapter 3. The ZnO NW placed between the Au electrodes is subsequently exposed to a deposition process of 50 nm Si_3N_4 by PECVD for the purpose of isolating the ZnO NW from contacting the atmosphere. Also, the PECVD procedure introduces defects to the ZnO NW, and the defects are also isolated in the ZnO NW by the Si_3N_4 layer. To investigate the diffusion of oxygen, half of the deposited Si_3N_4 is milled off by the FIB. The current and voltage (10 kV, 1 pA) of the milling parameters are chosen to be very small to make sure that the milling process does not introduce extra damage or defects in the NW. The resultant schematic structure of the device is shown in Figure 4.1.

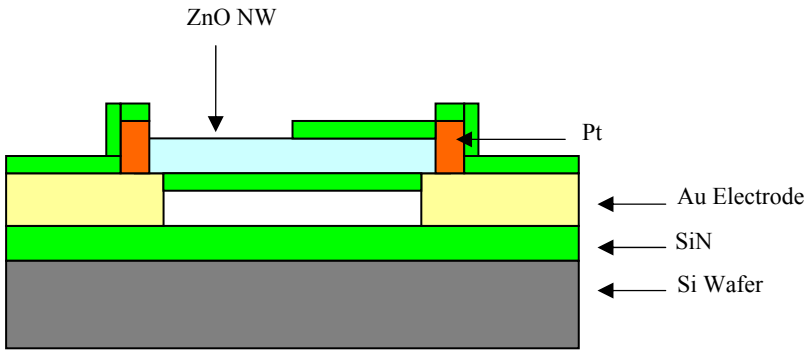

Figure 4.1 The schematic of a ZnO NW device under test.

Two samples of the ZnO NWs with different lengths and diameters are prepared through the above procedures. The two samples may also be slightly different in the concentration of the defects as introduced by the fabrication process. The I-V characteristic of the ZnO NW is then measured by an HP 4156A precision semiconductor analyzer immediately after the ion milling. Additional measurement is done on a daily basis through one week. For an easy comparison, the conductivity is used to represent the electronic property of the NW. The conductivity change of the ZnO NW over time could be expressed as

$$\Delta\sigma(t) = \Delta G(t) \cdot \frac{l}{A} \quad , \tag{4.1}$$

where $\Delta\sigma(t)$ is the conductivity change over time, $\Delta G(t)$ is the conductance change over time, which is measurable. l is the length of the NW and A is the cross section area. The plotted conductivity change over time is shown in Figure 4.2.

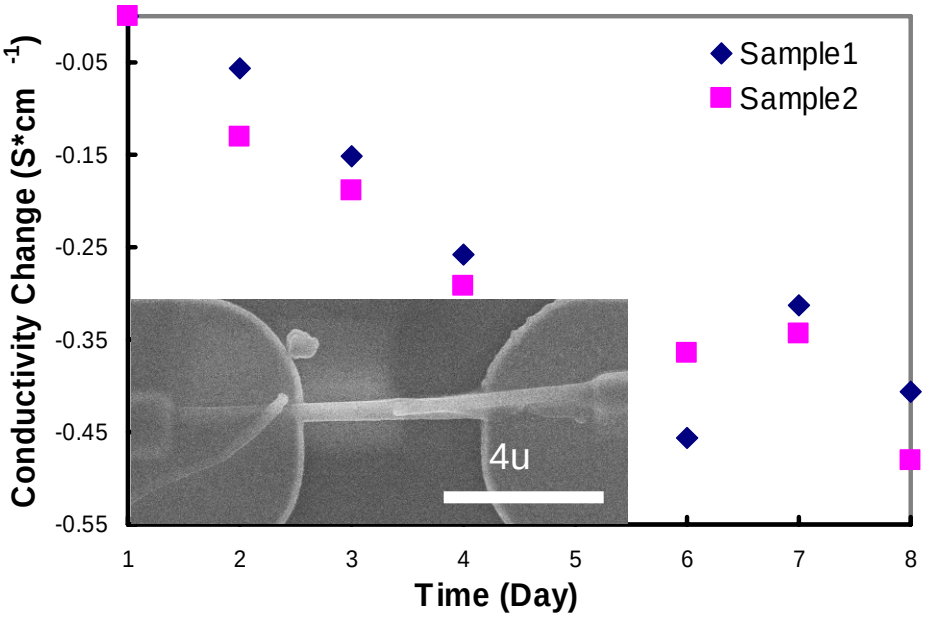

Figure 4.2 The conductivity change of two ZnO NWs over time. The inset shows the SEM image of one of the fabricated devices.

4.2 Data Analysis

It is well known that the conductivity of ZnO comes from the oxygen vacancies and the Zn interstitial defects [52]. Considering the large surface area of the NW, surface conductivity also contributes to the final data in the case of the ZnO NWs [53]. If the surface adsorption occurs quickly after the device is fabricated, the change in the conductance is mainly contributed from the change in the oxygen vacancy concentration of the ZnO NW volume. As more oxygen diffuses through the surface to fill the oxygen vacancies, the conductivity of the NW is expected to drop. A quantitative understanding of this process may derive the diffusion coefficient of the oxygen in ZnO nanostructures.

To explain the behavior of the observed conductivity change, we have carried out a simulation based on the following assumptions. First of all, the defects are assumed to

be uniformly distributed in the volume of the NW at the beginning of the experiment since the NW cross section is relatively small. Secondly, the oxygen molecules in the atmosphere adhere to the surface of the ZnO NW and break down to single oxygen atoms, which have the same molecular concentration as the oxygen molecule in the atmosphere (22% in volume). This is concluded from the fact that oxygen molecules absorbed on the surface of the ZnO NWs are decomposed into single oxygen atoms with the presence of oxygen vacancies. The oxygen vacancies on the surface are intrinsic as well as created by the plasma effect during the PECVD process. The presence of a large number of oxygen vacancies together with the constant diffusion of oxygen atoms into the bulk of the ZnO NWs drives the decomposition of the molecules. Therefore, it is assumed that the concentration of the single oxygen atoms on the surface of the ZnO NW is constant and the same as that of oxygen molecules in the atmosphere. This is to set the boundary condition. Lastly, the Si_3N_4 layer acts as an O_2 insulator between the atmosphere and the ZnO; thus, there is no oxygen penetration into the NW at the portion covered by the Si_3N_4 thin film. Oxygen could only diffuse through the exposed region to the NW. Based on these assumptions, a finite element analysis (FEA) model is established using the COMSOL^{TM} Multiphysics. The simulation is carried out starting from the Fick's law. Figure 4.3 illustrates the simulated oxygen concentration distribution profile inside a NW on the eighth day.

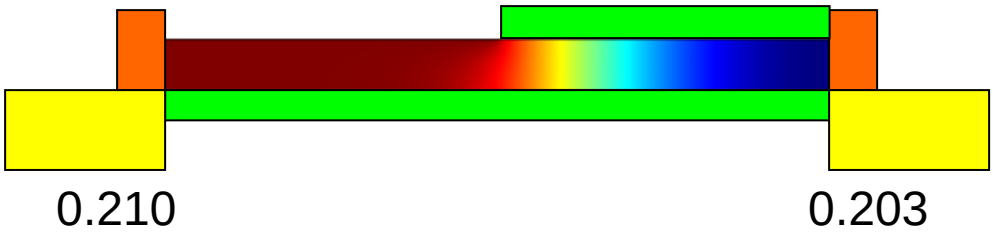

Figure 4.3 Simulated oxygen distribution on the eighth day after ion milling process.

As an n-type semiconductor, it is known that the conductivity in the ZnO could be expressed as

$$\sigma(t) \approx e \cdot n(t) \cdot \mu^e , \tag{4.2}$$

where $\sigma(t)$ is the conductivity of the ZnO as a function of time, e is the charge of an electron, $n(t)$ is the electron concentration over time and μ^e is the electron mobility of the ZnO. $n(t)$ could be expressed in terms of the created vacancies minus the vacancies that are filled by the oxygen atoms,

$$n(t) = \frac{2(V_D - \int_0^d C(x,t) \cdot dx)}{V} , \tag{4.3}$$

where V_D is the total oxygen vacancies, d is the diameter of the ZnO NW, $C(x,t)$ is the amount of diffused oxygen atom at a particular distance x from the surface at a particular time t. Each oxygen vacancy contributes two free electrons. V is the volume of the ZnO NW.

For two different time, t_1 and t_2

$$\Delta n(t) = n(t_2) - n(t_1) = \frac{\sigma(t_2) - \sigma(t_1)}{e \cdot \mu^e} = \frac{2(V_D - \int_0^R C(x,t_2) \cdot dx) - 2(V_D - \int_0^R C(x,t_1) \cdot dx)}{V}$$
$$= \frac{2(\int_0^R C(x,t_1) \cdot dx - \int_0^R C(x,t_2) \cdot dx)}{V} \quad . \tag{4.4}$$

Therefore, combine (2) and (4), we get

$$\frac{\Delta\sigma(t)}{e \cdot \mu^e} = -2\Delta C_o(t) \quad , \tag{4.5}$$

where $\Delta C_o(t)$ is the concentration change of oxygen atom due to diffusion.

From (4.5), we have

$$\Delta\sigma(t) = -2 \cdot e \cdot \mu^e \cdot \Delta C_o(t) \quad . \tag{4.6}$$

$\Delta C_o(t)$ could be obtained from the simulation. e and μ^e are known. It is possible to plot a curve of the conductivity versus time change as shown in Figure 4.4, which could link the oxygen diffusion coefficient in the ZnO NW with the simulation result. The following block diagram is used to illustrate the experiment processes.

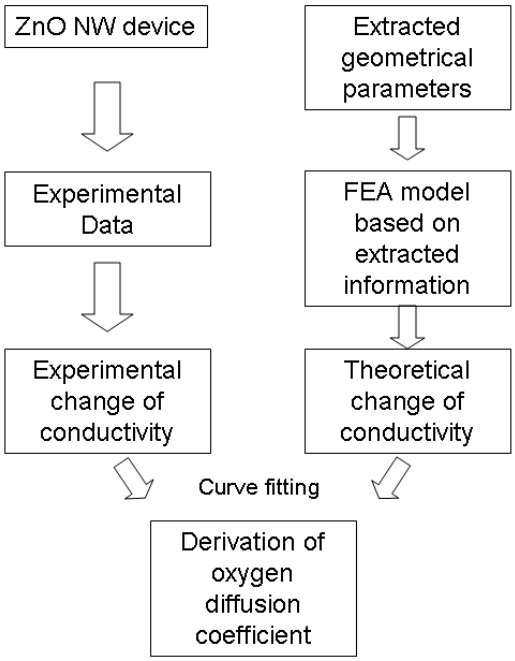

Figure 4.4 The flow chart of extracting the oxygen diffusion coefficient of ZnO NWs.

Oxygen diffusion coefficient is used to represent the actual diffusion process in the material. For ZnO, there is report that the mechanism of oxygen diffusion is interstitial and the coefficient is in the order of 10^{-15}~10^{-17} cm^2/s, depending on the growth temperature [54]. It is important to obtain the diffusion coefficient of ZnO nanostructures, which could be very useful in predicting the performances of sensors. To obtain the oxygen diffusion coefficient of ZnO NWs, the graphs of the conductivity change versus time are plotted for different coefficients in the COMSOL™. Experimental data are used to fit the theoretical plotting with the results shown in Figure 4.5. It is clear that the two sets of data fit between 1×10^{-13} and 1.5×10^{-13} cm^2/s, which is 2~4 orders of magnitude larger than that of bulk ZnO.

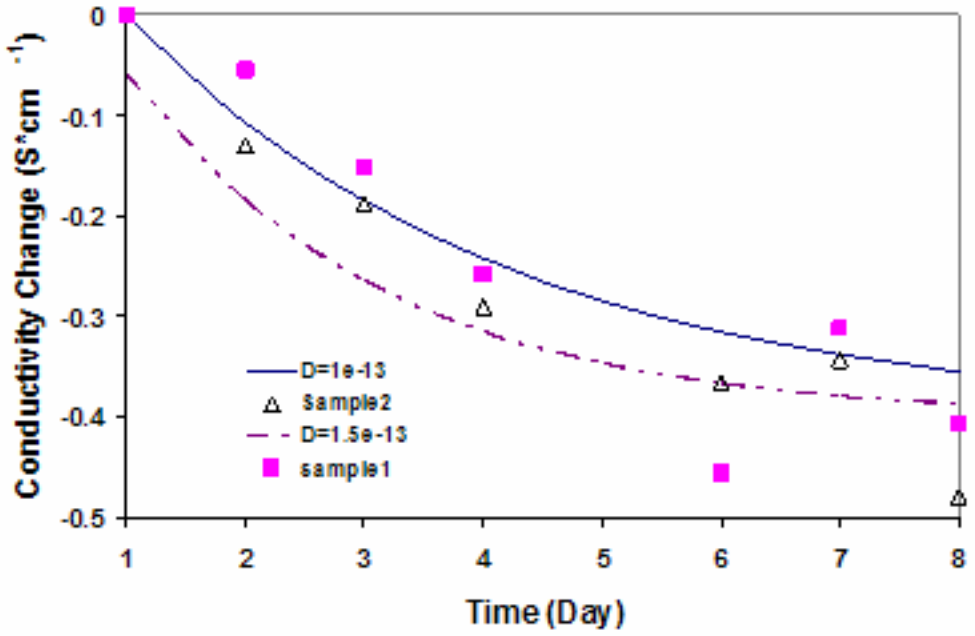

Figure 4. 5 The illustration of the curve fitting to determine the oxygen diffusion coefficient. The continuous lines represent the simulated results; while the dots represent the experimental results. The geometrical parameters are extracted from the SEM images of the tested NWs.

With the intention of explaining the difference in the oxygen diffusion coefficients between the ZnO bulk and NWs, TEM pictures are taken after the deposition of the Si_3N_4 thin film on the ZnO NWs, which are shown in Figure 4.6. From the pictures, it is apparent that there are point and planar defects introduced during the Si_3N_4 deposition process. In addition, it is possible that the growing process of the ZnO NW and milling process of the Si_3N_4 thin film introduce extra defects. These defects enhance the oxygen diffusion process dramatically, which results in the increase of the oxygen diffusion coefficient.

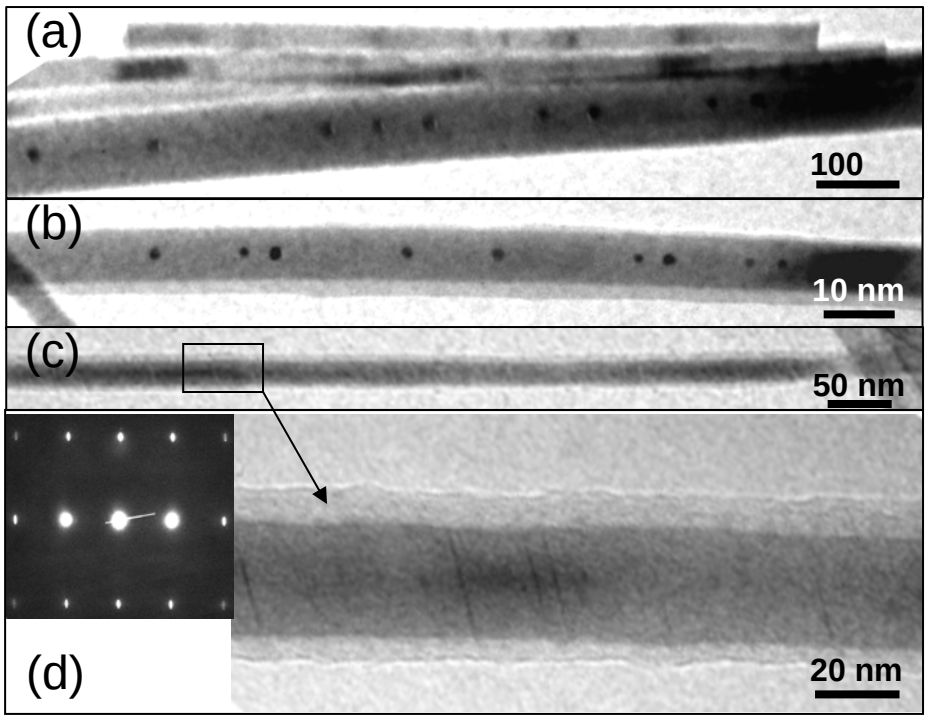

Figure 4.6 The TEM images of ZnO (a) and (b) nanobelts and (c) NW after Si_3N_4 deposition, showing the defects introduced in the volume as a result of nanofabrication.

4.3 Chapter Summary

A new method of calculating the ZnO NW oxygen diffusion coefficient is presented. It involves the fabrication and the characterization of a two port single ZnO NW device which is coated with a Si_3N_4 insulation layer. An FEA calculation is used to bridge the experimental data with the theoretical oxygen diffusion coefficients. The result suggests that the oxygen diffusion in the ZnO NWs is 2~4 magnitude higher than that of the bulk counterparts. This may attribute to the surplus defects formed during the growth of the ZnO NWs and the Si_3N_4 deposition processes.

CHAPTER V
BIO-SENSORS BASED ON ZNO NANOWIRES

Having considered the synthesis, the manipulation and the oxygen diffusion behavior of the ZnO NWs, the following chapters describe the applications based on these NWs. With the obvious advantages of the high surface-to-volume ratio, it is expected that the ZnO NW-based devices find their edges comparing with traditional devices in bio-medical sensing applications. Considering manipulating ZnO wires in nanosize is time-consuming, ZnO wires in microsize are used instead in several cases. This, however, does not change the underlying mechanism.

This chapter illustrates utilizing the ZnO wires as the platform for bio-sensor devices to detect a specific protein [55]. The bio-sensor device has the potential to detect any targeted bio-molecule. The background is introduced first, followed by the fabrication and the experiment protocols. Finally a conclusion is drawn based on the experimental data.

5.1 Motivation

Early detection of biological and chemical species has become more and more important lately in several fields ranging from biological research and clinical diagnosis to homeland security and many others. For example, cancer, the second leading cause of death in the US, could be cured with early stage detection and diagnosis, which requires

novel detection methods with ultra-high sensitivity [20]. Similarly, there is also an increasing demand for the detection devices to be portable, reliable and cost effective.

The conventional method for detecting proteins or peptides require radioactive material [56], biotin [57], digoxigen [58], fluorescent dye [59, 60], labeled probes, and large quantities of probe and analyte molecules. They are cumbersome, labor intensive and high-cost operations. Emerging detection methods, such as nanoparticles [2] and microcantilevers, [61] are capable of detecting antigen, antibody and other chemicals in trace quantities. For example, planar semiconductor devices have been introduced to serve as the basis for chemical and biological sensors, where the detection is monitored in terms of the change of the electrical conductivity. Metal oxide field-effect transistors (MOSFETs), which form the basis of semiconductor technology, can be converted into sensors by replacing the gate metal with chemically sensitive surfaces or membranes of interest [62]. The binding of the charged targeted species results in a depletion or an accumulation of mobile carriers within the MOSFET. This change is then picked up electrically. MOSEFT-based sensors are portable and cost effective compared with the conventional detection approaches. The detection mechanism is reliable and label-free. However, the relatively small surface-to-volume ratio determines that the detection sensitivity is limited. In addition, MOSFET-based sensors have to be fabricated on Si-based substrates, which limits its potential of integration with non-Si systems.

Electrical detection systems based on nanoscale materials avoid the usage of labeled probe and require as small as attogram quantities of analyte or target molecules. The fabrication of such sensitive, rapid throughput and cost effective detection systems is gaining tremendous importance in clinical diagnostics, industrial process control,

environmental protection, food packaging and homeland security. Chemical and biological sensors based on 1D structures, such as silicon NWs [63] and CNTs [18] can easily overcome the sensitivity and physical limitations of the planar semiconductor devices. The diameters of these 1D structures are in the range of tens to hundreds of nanometers. Any depletion or accumulation caused by the binding event will impose on the bulk of these structures as opposed to the surface layer in the planar semiconductor devices. The detection sensitivity can therefore be greatly enhanced. In addition, recent development in assembly and integration processes has enabled the preparation of dense NW or CNT arrays [49]. These techniques remove the barrier of the large-scale assembly of 1D nanostructures. Lieber et al. [64] have demonstrated a real-time, high sensitivity and multiplexed virus detection by silicon NW-based sensors. Given the fact that these NWs are synthesized prior to the assembly, it is possible to fabricate these devices on substrates other than Si, such as plastic substrate and printed circuit board (PCB). The integration flexibility is enhanced, too.

5.2 The Fabrication and the Experiment Protocols

The ZnO wires are synthesized according to the method illustrated in chapter 2. The manipulation and contact formation are described in chapter 3. In short, the as-synthesized ZnO wires are transferred to the pre-patterned Au electrodes using micro-manipulation method. The ohmic contact is prepared by depositing Pt on both ends of the wire. After that, a thin layer of Si_3N_4 with the thickness of 50 nm is deposited by a Unaxis PECVD to provide insulation to the device. The entire transfer and deposition

process is shown in Figure 5.1. The SEM images of the device are illustrated in Figure 5.2, where both the whole device and the contact part are presented.

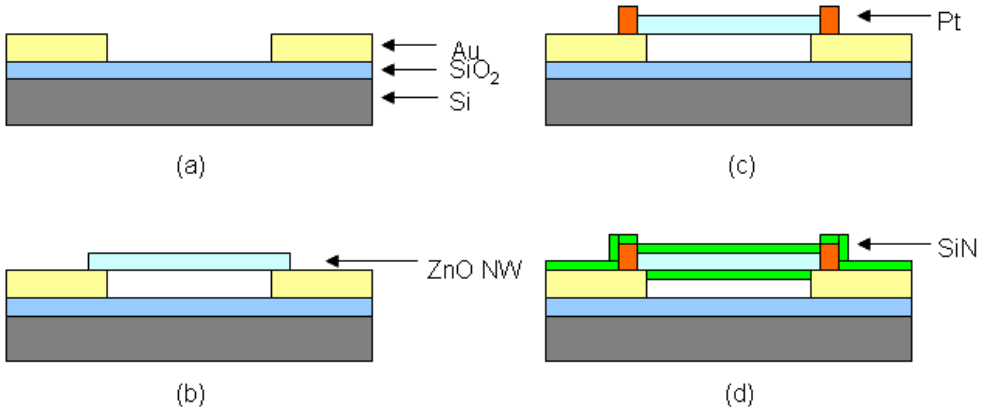

Figure 5.1 The schematics of the transfer and subsequent processing steps of a ZnO wire. (a) The pre-fabricated Au electrodes; (b) The ZnO wire is transferred to the electrodes by the micro-manipulation technique; (c) Pt is deposited on both ends of the ZnO wire; (d) The Si_3N_4 thin film is deposited by the PECVD.

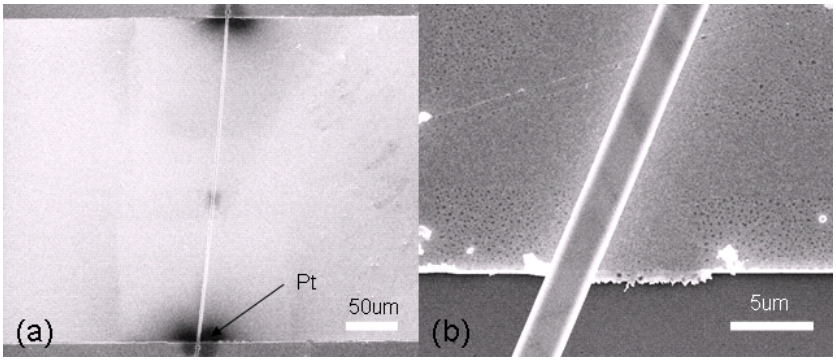

Figure 5.2 The Images of a ZnO bio-sensor. (a) the SEM image of a ZnO wire device; (b) The SEM image of the contact region.

The ZnO devices are surface modified with 3-(trimethoxysilyl) propyl aldehyde for 30 minutes. The devices are then washed with 95% ethanol and DI H_2O three times to remove unbound silane compounds, and heated at 120˚ C for 15 minutes. The bio-functionalization is carried out by incubating the devices with anti-IgG antibodies in 10

mM phosphate buffer solution (PBS) (pH 8.4) containing 4 mM sodium cyanoborohydride for 3 hours. The passivation to the unreacted aldehyde surface groups is done with ethanolamines in the presence of 4 mM cyanoborohydride. The coated antibodies on the devices are hybridized with IgG antibodies at a concentration of 50ng/ml for 1 hour. NaCl solution of 0.5 M was used to remove any non-specifically adsorbed antibodies. The devices are then rinsed with DI H_2O, and air-dried. Reference samples are set up following the same protocols except that there are no anti-IgG antibodies in the PBS. Figure 5.3 illustrates the bio-funcationalization process for the ZnO devices.

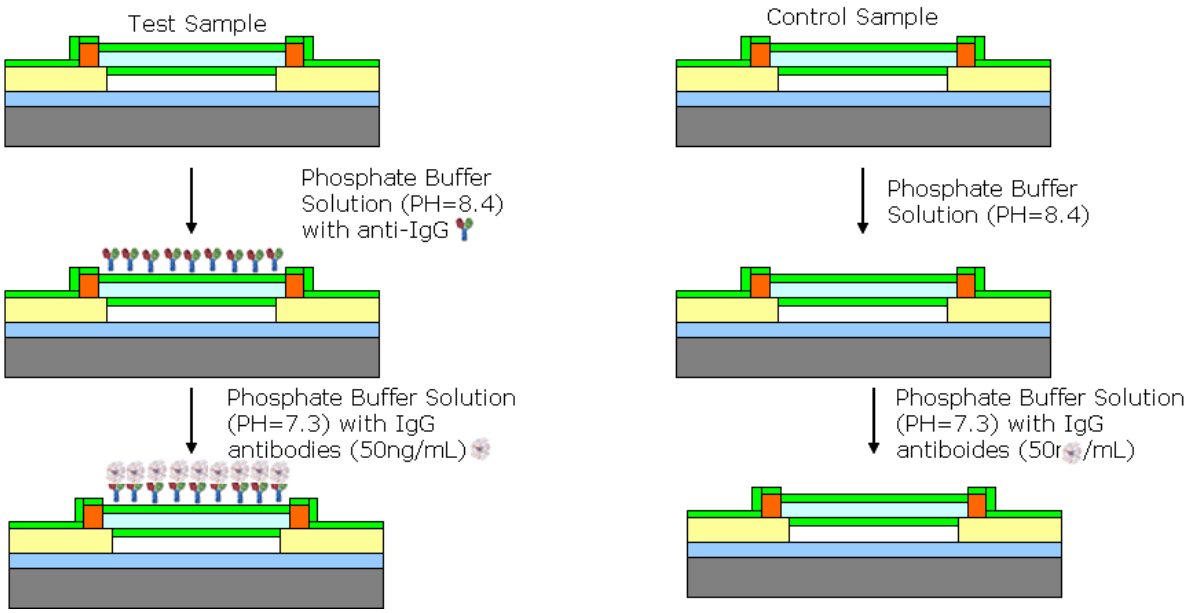

Figure 5.3 The bio-functionalization protocols of the ZnO devices.

All the I-V characteristic measurements are taken by an HP 4156A Precision Semiconductor Analyzer. A LEO 1530 field emission microscope is used to take the SEM images of the samples.

5.3 Results and Discussion

The I-V characteristics of the ZnO bio-sensor are taken three times during the experiment. First measurement is done after the device is fabricated, which is called original in the plot; second measurement is done after the anti-IgG antibodies are bound to the surfaces of the devices, which is called the functionalization in the plot; while the last measurement takes place after the binding happens between the anti-IgG and IgG antibodies, which is called the hybridization. To compare the morphology change on the surfaces of the device, SEM images are taken for both the test sample and the reference sample. All of these are shown in Figure 5.4. The difference between the reference sample and the test sample in terms of the I-V characteristics and morphology is clearly seen. For the ease of comparison, the currents taken at 1 V and the change in percentile are tabulated and shown in Table 5.1. There is a 12.4% current change in the test sample compared to only 1.9% in the reference sample. The morphologies also exhibit distinct difference between the reference sample and the test sample.

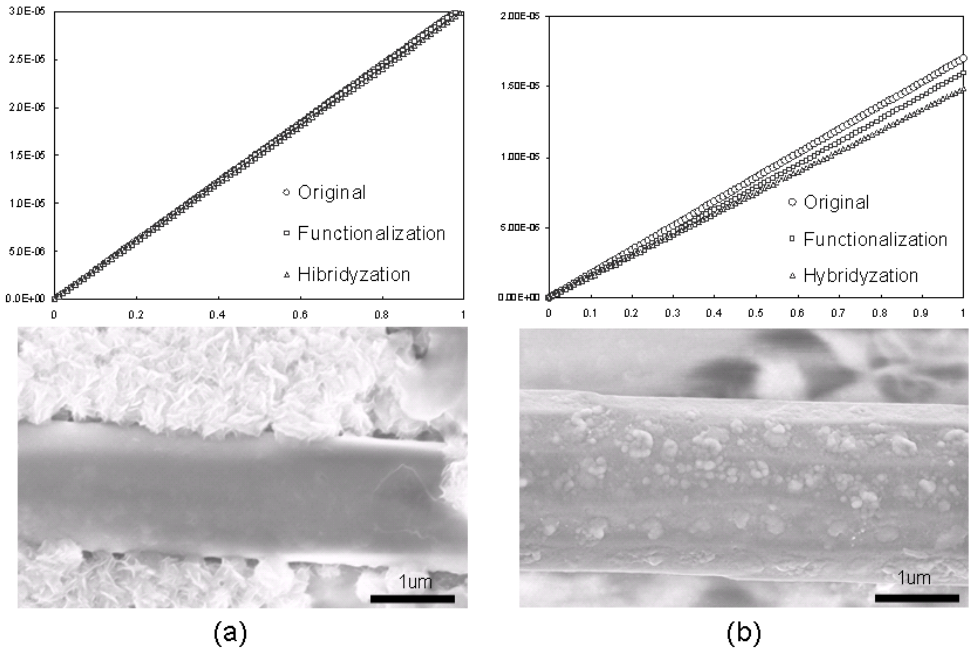

Figure 5.4 The I-V characteristics and SEM images of (a) control sample and (b) test sample.

Table 5.1 The comparisons of the I-V change for each of the steps. The currents are measured at 1V. The entire percentile changes are taken with respect to the original current values.

	Original (uA)	Functionalization (uA)	Hybridization (uA)
Reference Sample	30.7	30.5	30.1
Test Sample	17.0	16.0	14.9
	Original	Functionalization	Hybridyzation
Reference Sample	1	0.65%	1.9%
Test Sample	1	5.9%	12.4%

The fundamental sensing mechanism of metal oxide-based gas sensors relies on a change in the electrical conductivity due to the interaction process between the surface complexes such as O^-, O^{2-}, H^+ and OH^- reactive chemical species and the gas molecules to be detected [65]. As for the detection mechanism in bio-molecules, Scouteyrand et al. [66] propose that in the case of DNA detection, the negative charge of the DNA strands (from PO^{4-} groups) influences the spatial charge of the electrode, repelling the electrons in the n-doped semiconductor. This leads to a conduction band edge curvature toward the positive energies with a decrease of the electron density in this zone of spatial charge. This results in a higher resistance and impedance, which has been observed for n-type $CdIn_2O_4$ thin film by Zebda et al. [67]. Lieber et al. [63] demonstrate that field-effect accounts for the conductivity change in Si NW sensors. In addition, Hu et.al. [68] report the observation of the direct electron transfer between the hemoglobin and the polytetrafluoroethylene (PTFE) film which serves as the matrix material. Therefore, it is reasonable to propose that both the localized field effect induced by the charged bio-molecules to the ZnO wire and the contact area are the factors affecting the resistance of the sensors. The micro and nanostructures offer safe, long lasting, cheap and smart bio-sensors. For 1D structures, the diameters are in the range of tens to hundreds of nanometers. Because of the high surface-to-volume ratio, the binding events have a dramatic influence on the conducting properties of the sensing element.

The individual sensing elements demonstrated in this work can be easily multiplexed to form a sensor array and functionalized with different pathogen specific antibodies. The sensor array is able to provide a detection pattern for a specific chemical or bio-molecule. Coupled with the interface electronics, the pattern can be analyzed through typical signal

processing techniques for pattern recognition. For simple systems, a histogram of responses can be generated for various potential pathogens; and the unknown subject can be identified by matching the pattern to one of the known substances in the library. Combined with micro-fluidics and sensor array, this work can lead to an accurate and real-time detection of chemicals and bio-molecules.

5.3 Conclusions

We systematically present the fabrication process of the ZnO wire-based sensors, followed by the bio-functionalization protocols. The electrical characterization is carried out to detect any change due to the specific binding of the bio-molecules on the ZnO surfaces. It is shown that a more than 12% change in the current is detected in the test sample as opposed to the 1.9% change in the control sample for the protein IgG with concentrations as low as 50 ng/ml. Corresponding morphological changes are observed with the SEM images. For the first time, we demonstrate the ZnO sensing capability toward bio-molecules.

5.4 Chapter Summary

In this chapter, the application of utilizing ZnO wire in biological field is presented. The chapter starts with the motivation behind this work and the advantages of employing the ZnO wire structures. Then, the fabrication and the bio-functionalization procedures are outlined in the subsequent sections. The results based on the observation of the electrical measurement and the SEM images are presented. The mechanism that

governs such change is discussed based on previous work. Finally, the conclusion is drawn and future direction is proposed.

CHAPTER VI

REAL-TIME ZNO BIO-SENSOR WITH A MICRO-FLUIDIC CHANNEL

Previous chapter describes the detection of the IgG proteins based on the ZnO devices. It is, however, not a real-time detection scheme, as the characteristics of the devices are measured after the analyte on the devices vaporizes. This prevents the devices from more practical applications since most bio-molecules, if not all, are based in aqueous media. It is necessary, therefore, to develop a detection scheme that enables the real-time detection approach based on the ZnO devices.

This chapter first discusses the necessity of utilizing the micro-fluidic channel for the ZnO-based bio-sensors. Another platform, ZnO thin film-based bio-sensors, is also introduced in this chapter. The motivation behind it is presented. The fabrication process of thin film-based devices is illustrated followed by the experimental protocols and the measurement setup. Finally the data and mechanism governing the performance of the two kinds of bio-sensor are discussed. The chapter is summarized with the conclusion based on the analysis.

6.1 Motivation

Recent years have witnessed the significant research activities of nanostructure-based electrical detection system. Chemical and biological sensors based on 1D structures, such as silicon NWs [63] and CNTs [18] can easily overcome the sensitivity

and physical limitations of planar semiconductor devices. While the detection mechanism is still debatable [18, 55, 69, 70] (Table 6.1), it is agreed that the detection process is free of labeled probes. Furthermore, the diameters of these 1D structures are in the range of tens to hundreds of nanometers. Any depletion or accumulation caused by the binding event would impose on the entire surface area of these structures as opposed to the top surface layer in planar semiconductor devices. Therefore, the detection sensitivity can be greatly enhanced. Given the fact that these NW are synthesized prior to the assembly, it is possible to fabricate these devices on substrates other than Si, such as plastic substrate and PCB.

Table 6. 1 Summary of previous work on NW based bio-sensors.

Platform	Carrier Type	Analyte/Net Charge	Change in Resistance	Reference
Si NW	p-type	Virus/ Positive Charge	Increase	[70]
In_2O_3	n-type	LDL/ Positive Charge	Decrease	[69]
CNT	p-type	Protein/ Negative and Positive	Increase	[18]
ZnO	n-type	Protein/ Negative Charge	Increase	[55]

While the devices utilizing the ZnO NWs are theoretically more sensitive than planar devices, it is difficult to apply them to a large manufacturing scale. This is especially true considering the alignment and assembly is still a problem despite many research efforts going on [49, 71] in this field. Thin film devices, which are fabricated

through the top-down approach, on the other hand, are subject to mature processing technologies and can be easily integrated into the microelectronic industry. Furthermore, there has been some work on fabricating NW based bio-sensor using top-down approach [72, 73], which are far more controllable than the bottom-up approach. Therefore, it is worth trying to use ZnO thin film to fabricate bio-sensor systems that perform similarly as NW devices.

A micro-fluidic system deals with the behavior, precise control and the manipulation of fluids with very small volume. The micro-fluidic channel integrated with the existing platform is able to guide and regulate the fluid flow over the sensor while avoid generating artifact by shorting the electrodes. Unlike traditional methods, where large amount of agent is involved, in a micro-fluidic system, very small amount of agent is required to carry out the experiment due to the fact that the micro-fluidic system operates with very small volume of analyte. There are several choices when considering the material for the micro-fluidic channel. In this work, a commercially available glass micro-fluidic tube is chosen. Compared with other approaches such as the polydimethylsiloxane (PDMS) or the Si based channels, the glass channels are more bio-compatible, easier to fabricate and more cost effective. Considering SiO_2 is a well-documented material in the industry, the integration process could be easier as well. Together with the low additional cost, existing bio-sensors with the glass micro-fluidic system are capable of carrying out the measurement in real-time and aqueous environment without significantly increasing the size and cost of the system.

6.2 Thin Film Device Fabrication

The ZnO thin film (50 nm) is sputtered on to a Si substrate with a PVD RF Sputterer (Kurt J Lesker Co) and annealed in O_2 at 350˚ C. The oxide is then patterned with a single etch back process. A thin film positive photoresist (SC 1813, Shipley/Rohm and Haas) is used to accurately define the oxide geometry, which is 5 um × 35 um. ZnO can be etched with most acids and bases. Suitable dilution is needed to weaken the etching action and control the etch rates. After defining the ZnO geometries, the contact pads are patterned through a lift-off process. The e-beam evaporated Au pads are chosen as the material of the electrodes. Au cannot be selectively etched with respect to zinc oxide. Hence, a lift-off process is ideal to accurately define the gold geometries without damage the zinc oxide layer. A thick negative photoresist (Futurrex, NR5 8000P, 8-9 microns) is used to perform the task. Finally, as for ZnO NW-based devices, a 50 nm Si_3N_4 layer is deposited on the device. Figure 7.1 illustrates the fabrication process of the thin film ZnO device. The SEM image of the ZnO NW-based devices as well as the optical image of the thin film-based devices is shown in Figure 7.2.

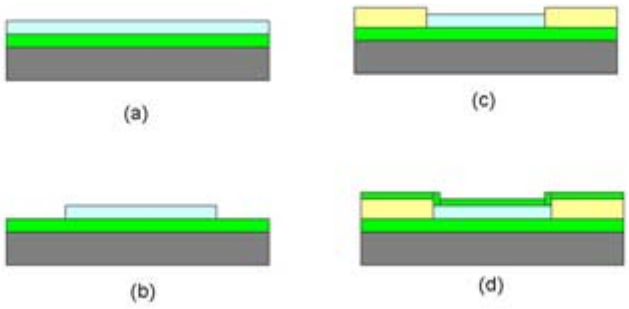

Figure 6.1 The fabrication process of the ZnO thin film-based devices.

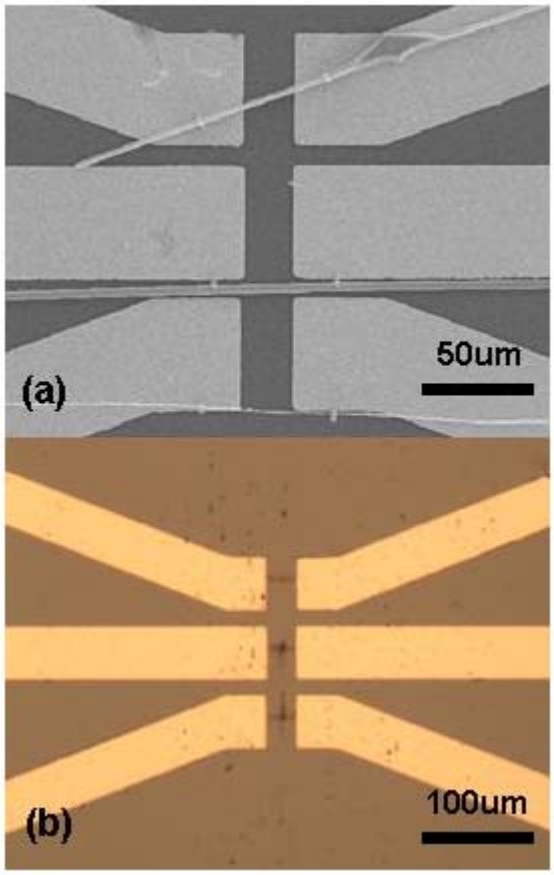

Figure 6.2 (a) The SEM image of a ZnO NW-based device; (b) The optical image of a ZnO thin film-based device.

6.3 The Experiment Protocol

Both the ZnO NW and the thin film devices are surface modified with 3-(trimethoxysilyl) propyl aldehyde for 30 minutes. The devices are then washed with 95% ethnol and DI H_2O three times to remove the unbounded silane compounds, and heated at 120˚ C for 15 minutes. The bio-functionalization is carried out by incubating the devices with biotin hydrazide (50ng/ml) in 10 mM phosphate buffer solution (PBS) (pH 8.4) for 2 hours. The passivation to the unreacted aldehyde surface groups is done with the ethanolamines in the presence of 4 mM cyanoborohydride for 1 hour. The real-time

sensing measurements are taken with strepatavidin proteins (50ng/ml), which have a specific binding with biotin. The control experiment is conducted with non-specific protein such as IgG protein (50ng/ml). An electrochemical analyzer (CH Instruments, model 1200A series) is used to carry out the electrical measurement. The instrument consists of a digital function generator, a data acquisition system, and a potentiostat/bipotentiostat.

6.4 The Experiment Set Up and the Micro-fluidic Channel Integration

Two different approaches are taken to carry out the experiment. For the NW-based devices, no micro-fluidic channel is integrated with the bio-sensor. The solution containing the analyte is dispensed onto the device with a syringe. The electrical contacts are established on both ends of the device, as shown in Figure 6.3 (a). As for the thin film-based devices, a micro-fluidic channel made of glass with inner diameter of 0.5 mm is bonded to the platform after the functionalization (Figure 6.3 (b)). A glass fiber with 100 μm inner diameter (Polymicron Technologies) is used to connect the device to a syringe with the help of an adapter (InnovaQuartz). Figure 6.3 (c) shows the final setup of the system.

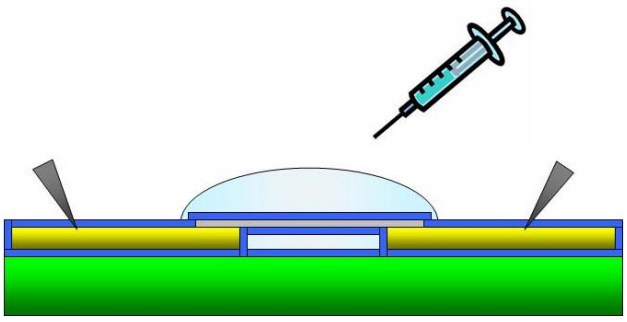

(a)

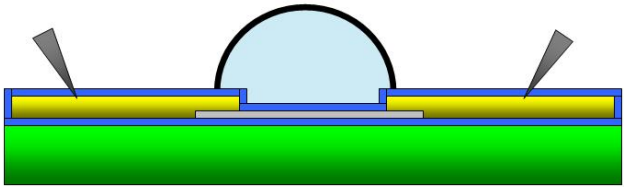

(b)

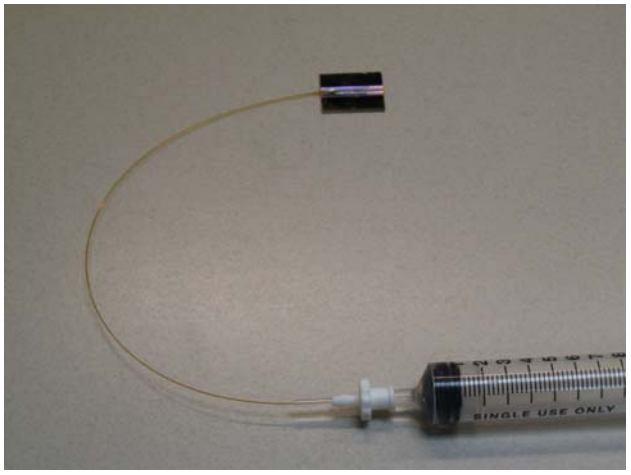

(c)

Figure 6.3 (a) A cross sectional view of the experimental setup for the NW-based device, where the analyte is dropped onto the device; (b) A cross sectional view of the experimental setup for the thin film-based device, where the glass channel is integrated with the device. Analyte is flown through the channel; (c) An optical image of the final setup.

6.5 Results and Discussion

Figure 6.4 shows the amperometric measurement of the two experimental setups. The horizontal axis represents time, and the vertical axes stands for the change in resistance. The graph on the top represents the measurement taken from the ZnO NW-based device. In the graph, the "control" measurement is conducted with the analyte that contains the non-specific protein (IgG); while the pink curve labeled as "SA" indicates that the analyte contains the specific protein, streptavidin. The arrow points to the time when the analyte is added to the system. The bottom graph, which represents the results from the thin film-based device, is denoted in the same way.

It is clearly seen from the graphs that both of the devices are able to detect the presence of streptavidin selectively and specifically. In the case of the NW-based device, there is a more than 15% change in the resistance after 1000 seconds of the addition of the streptavidin analyte; whereas only 3% change in resistance is observed in the case of the non-specific protein (IgG). Similar trend can be found in the thin film-based device measurement.

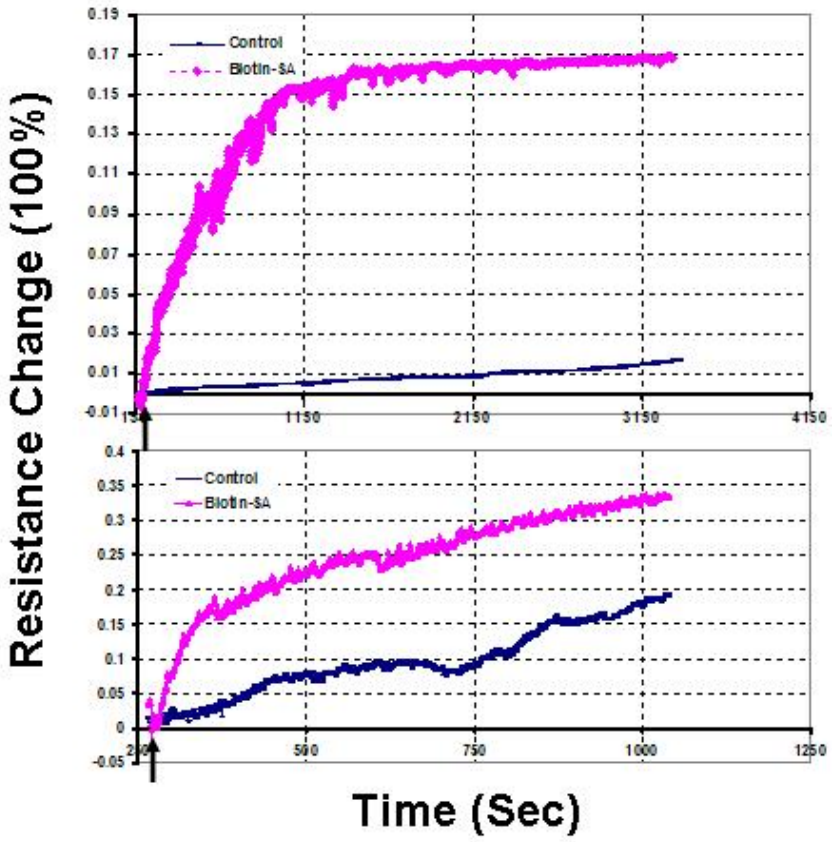

Figure 6.4 The amperometric measurement of the ZnO NW-based device (above) and the thin film-based device (below). The arrow indicates the time when the analyte is added to the devices. Control means the analyte with the non-specific protein (IgG); while SA represents the analyte with the streptavidin, which has the specific binding ability with the biotin.

There are several concepts that need to be introduced to understand the phenomena mentioned above. The first one is the specific binding between biotin and streptavidin. Figure 6.5 illustrates the working mechanism. The biotin (B) modified device surfaces has a very strong binding affinity with streptavidin (SA). Therefore, if streptavidin is present in the analyte, it can be quickly drawn to the vicinity of the devices and bind to the biotin because of this strong binding affinity. As mentioned earlier, the working mechanism of the semiconductor-based bio-sensor relies on the fact that the depletion region under the channel be modified by the presence of net charges. The

modification of the depletion region will in turn change the resistance of the device, which can be picked up by the amperometric measurement. Depending on the polarity of the net charges and the type of semiconductor, the resistance can either increase or decrease. ZnO is an n-type semiconductor due to the oxygen vacancies formed during the synthesis; and the streptavidin is negatively charged at the pH of 8.4. Therefore, the binding of the streptavidin to the biotin on the surfaces of the ZnO devices will bring an increase in the resistance. Another concept needs to be introduced is non-specific binding (NSB) [18, 74], which happens between the proteins, such as IgG and streptavidin in this case, and surfaces of any kind. NSB exists universally, and it can also affect the resistance. The NSB, however, is much weaker than the specific binding. The change in resistance is therefore smaller than that of the specific binding. The baseline increase in all four experiments shown in Figure 6.4 can be explained by the NSB. The sharp increase that results from the addition of streptavidin is due to the specific binding between biotin and streptavidin. This binding is much stronger and more evident than the NSB that introduces the resistance change in the control experiment.

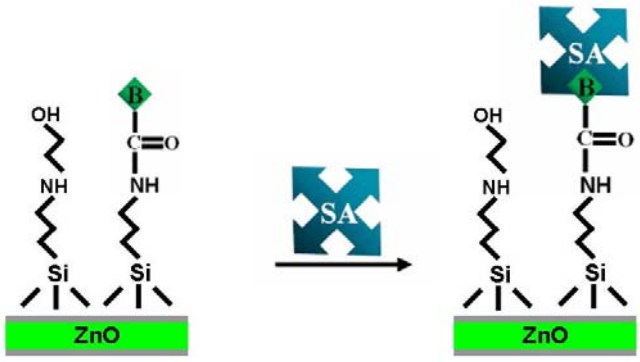

Figure 6.5 The specific binding between the biotin (B) and the streptavidin (SA) on the biotin modified ZnO surfaces.

Another interesting phenomenon is that the baseline increase in the NW-based device is much smaller than that in the thin film-based devices. A possible explanation arises from the different crystalline structures of these two devices. ZnO NWs utilized in the experiment are single crystals because of the way they are synthesized. ZnO thin film-based devices, on the other hand, are sputtered polycrystalline materials, which exhibit different surface characteristics due to the existence of grain boundaries. These grain boundaries together with the biotin that modify the device surfaces could trap more non-specific binding analyte, which is IgG in the experiment. In other words, the NSB in the ZnO thin film-based devices is more evident than the NSB in the NW-based devices. Therefore, from the perspective of the signal to noise ratio, ZnO NW-based devices perform better, although ZnO thin film-based devices are easier to scale up in terms of manufacturing capability.

6.6 Conclusions

Through this work, we have demonstrated the capability of utilizing ZnO NWs and thin films as the building blocks to fabricate the bio-sensors which can be used to detect bio-molecules in real-time. ZnO NW-based devices are tested with the analyte of interest; and the ZnO thin film-based devices are integrated with a glass micro-fluidic channel before the test is carried out. Both of the devices are capable of detecting the presence of the analyte of interest in real-time. By comparing with the control experiments, we show that this detection is specific and selective. This is a real-time, label-free, and cost effective process which can be exploited further by expanding into

arrays. It is possible to integrate this platform with other micro-electronic elements to form portable, reliable and cost effective devices with application in many areas.

6.7 Chapter Summary

The chapter starts with the motivation behind the work, which is the need for a real-time, ultra-sensitive, portable bio-sensor platform. Various aspects of the system, including the NW-based devices, thin film-based device as well as the micro-fluidic channels, are introduced. The device fabrication and experiment protocols are discussed followed by the experiment results and analysis. Finally, an investigation into the mechanism and the explanation of the observed phenomena are presented.

CHAPTER VII

POWER GENERATION BASED ON ZNO NANOWIRE ARRAYS

Converting the mechanical vibration energy to the electrical energy through ZnO NWs is a newly developed concept [32]. It relies on the coupling properties of the semi-conductivity and the piezoelectricity of ZnO. Previously, the conversion is realized by scanning the vertically aligned ZnO NWs with an AFM tip. This, however, does not provide feasible solution for practical applications. In this chapter, a continuous current output is achieved from an ultrasonic wave driven nano-generator. In the first section of the chapter, the work in fabricating and characterizing the device is presented. The as-fabricated device is also capable of operating in bio-fluid, which is shown in the second part of the chapter.

7.1 A Direct-current Nano-generator Driven by Ultrasonic Wave

7.1.1 Motivation

Wang and Song [32] have demonstrated an innovative approach for converting the mechanical energy into the electric energy in nanoscale with piezoelectric ZnO NW arrays. By deflecting the aligned NWs with a conductive AFM tip in contact mode, the mechanical energy created by the deflection of ZnO NWs is converted into the electric energy with the help of the AFM. This phenomenon is due to the coupled

semiconductive and piezoelectric properties of the NWs as stated in [32]. To improve the power generation capabilities of the system, it is necessary to replace the AFM tip with a simpler deformation source that can actuate all the NWs simultaneously and continuously. The problem can be solved in the following ways. First, the AFM tip can be replaced by a V-shaped top electrode which resembles the functionality of many AFM tips. Figure 7.1 illustrates the working mechanism. It can be seen from the figure that even though both sides of the NW are in touch with the V-shape electrode, it is equivalent to the scenario where the AFM tip contacts the NW with the negative potential. This is because the contact between the positive side of the NW and the V-shape electrode is in reversed biased region of a schottky contact. No current or very little current can flow through.

The idea can be extended from a single V-shape trench to a three-dimensional (3D) top electrode where the V-shaped trenches are placed next to each other, as shown in Figure. 7.2.

The second half of the approach to solve the aforementioned problem is to use ultrasonic waves to drive the motion of the NWs. This will eliminate the usage of the AFM tip and result in a continuous output for both the current and the voltage.

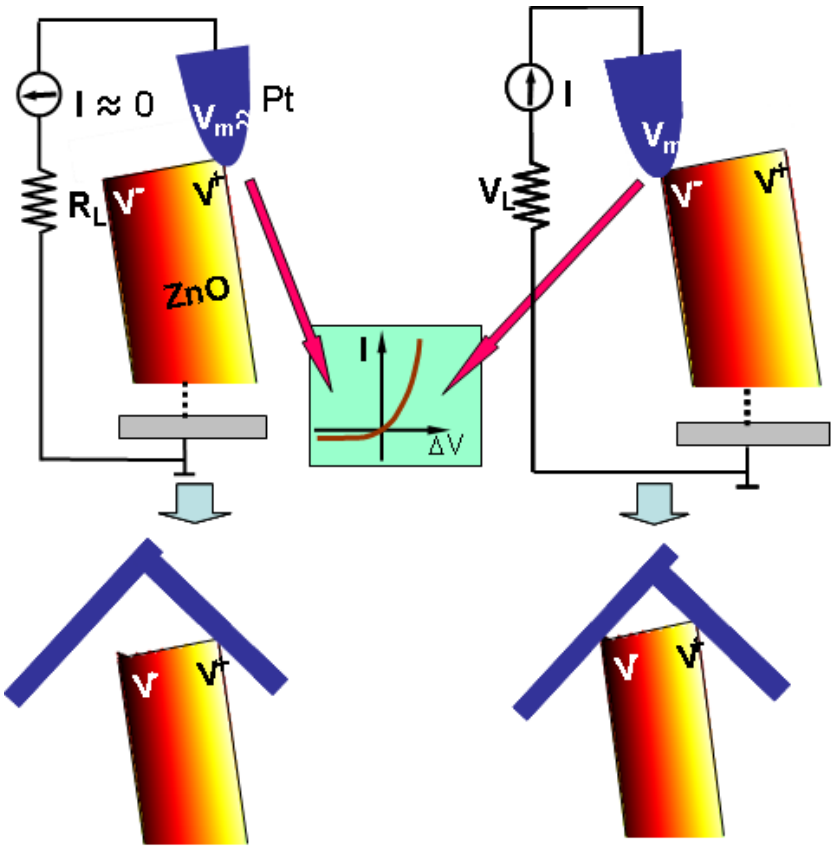

Figure 7.1 The working mechanism of a V-shaped electrode and its relationship with an AFM tip.

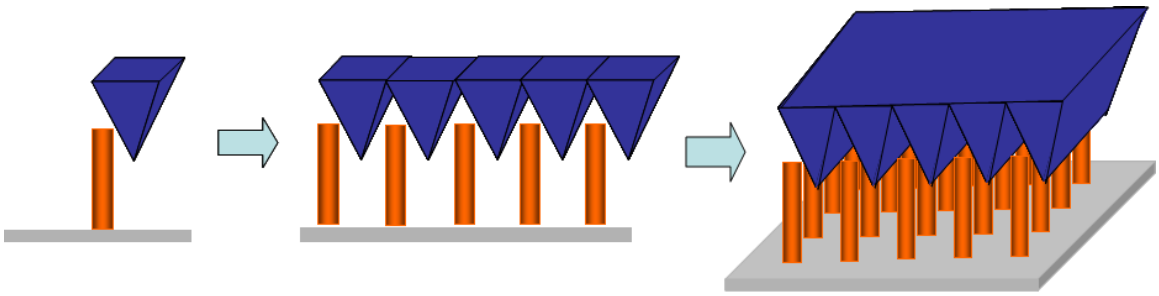

Figure 7.2 The electrodes expansion from one AFM tip to a three-dimensional top electrode.

7.1.2 Top Electrode Fabrication

The fabrication of the top electrode has taken the advantage of Si wet etching [75]. Due to the different etching rates of different Si orientations in potassium hydroxide (KOH) solution, the final profile of Si after KOH wet etching exhibits triangular shapes with an angle of 54.8 degrees (Figure 7.3). Figure 7.4 illustrates the fabrication flow of the top electrode in a two step wet etching process.

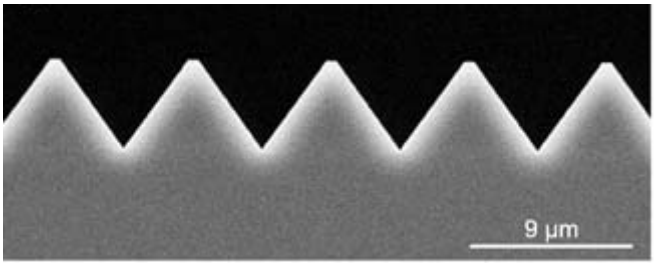

Figure 7.3 A Si wet etching profile with a slope of 54.8 degrees [75].

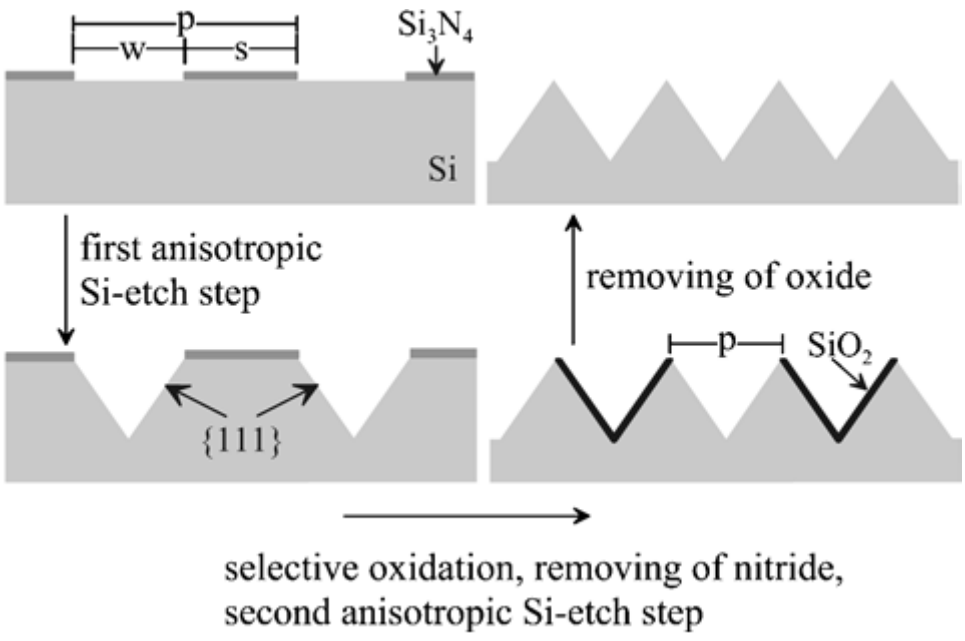

Figure 7.4 An illustration of the two step wet etching process to obtain the top electrode of the nano-generator.

In the two step etching process, a (100) Si wafer is used as the body for the to be fabricated electrode. A 50 nm thick Si_3N_4 layer is deposited on the Si wafer by a Unaxis PECVD. A subsequent patterning process transfers a pattern of periodic strips with a width of 2 um to the photoresist which is spun on top of the Si_3N_4 layer through deep UV lithography. The pattern is then transferred again from the photoresist to the underlying Si_3N_4 layer with the help of a Plasma-Therm inductive coupled plasma (ICP) etcher, which serves as the hard mask for the wet etching. After these steps, the Si wafer is placed in a bath containing 35% KOH in DI water. The bath is agitated with an ultrasonic cleaner to keep the active ingredient (KOH) uniformly distributed in the solution. In addition, the agitation removes one of the reaction products, hydrogen, off the Si surface quickly to allow for the subsequent reaction to take place.

The first step etching is finished with the formation of the first half of the V-shaped trenches with a pitch of 2 um, as shown in Figure 7.5 (a). A following oxidation process oxidizes the bare Si surface which is exposed due to the previous etching step. By this way, the already formed V-shaped trenches will be protected in the second etching step. The remaining Si_3N_4 layer is then removed through a hot sulfuric acid bath (85% H3PO4 in DI water), followed by a second step wet etching process which is conducted under the same principle as the first step. The electrode morphology after the second step etching is shown in Figure 7.5 (b). The process is finished with the removal of the oxide layer and the Pt deposition. Figure 7.5 (c) illustrates the final SEM of the top electrode prior to the Pt deposition.

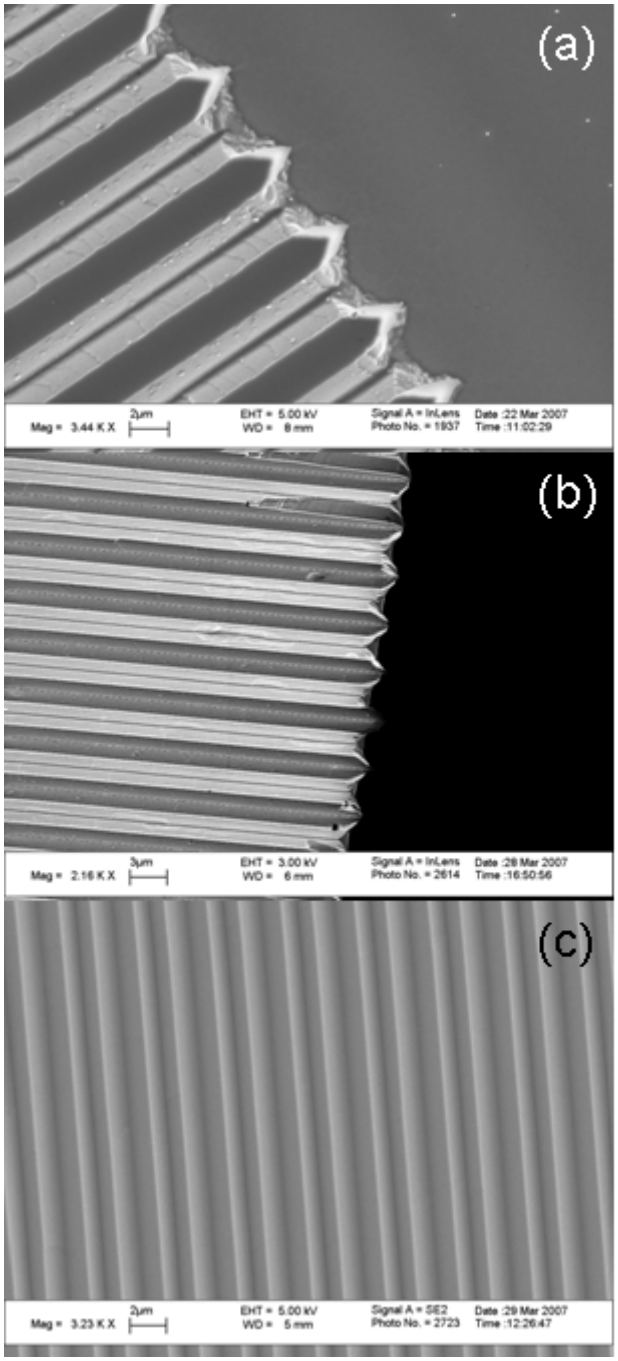

Figure 7. 5 SEM images of a Si top electrode after (a) first step wet etching, (b) second step wet etching, and (c) oxide removal.

7.1.3 Experiment Setup

The experimental setup is schematically shown in Figure 7.6 (a). An array of the aligned ZnO NWs is covered by a Si top electrode coated with Pt. The Pt coating not only enhances the conductivity of the electrode, but also creates a schottky contact at the interface with the ZnO NWs. The NWs are grown on either GaN substrates (Figure 7.6 (b)) or sapphire substrates that are covered by a thin layer of ZnO film [27, 76], which serves as a common electrode for directly connecting the NWs with an external circuit. The density of the NWs is ~10/mm^2, and the height and the diameter are ~1 mm and ~40 nm, respectively. The top electrode is fabricated according to the process detailed in the previous section. It is coated with a thin layer of Pt (200 nm in thickness) (Figure 7.6 (c)). The electrode is placed above the NW arrays and manipulated by a probe station under an optical microscope to achieve precise positioning; the spacing is controlled by soft-polymer stripes between the electrode and the NWs at the four sides. The resistance of the nano-generator is monitored during the assembly process to ensure a reasonable contact between the NWs and the electrode by tuning the thickness of the polymer film. Then the assembled device is sealed around the edges to prevent the penetration of liquid. A cross-sectional image of the packaged NW arrays is shown in Figure 7.6 (d); it displays a "lip/teeth" relationship between the NWs and the electrode. Some NWs are in direct contact with the top electrode, but some are located between the teeth of the electrode. The inclined NWs in the SEM image are primarily caused by the cross sectioning of the packaged device. The packaged device is supported by a metal plate that is in direct contact with water contained in the cavity of an ultrasonic generator. The operation

frequency of the ultrasonic wave is ~41 kHz. The output current and voltage are measured by an external circuit at room temperature.

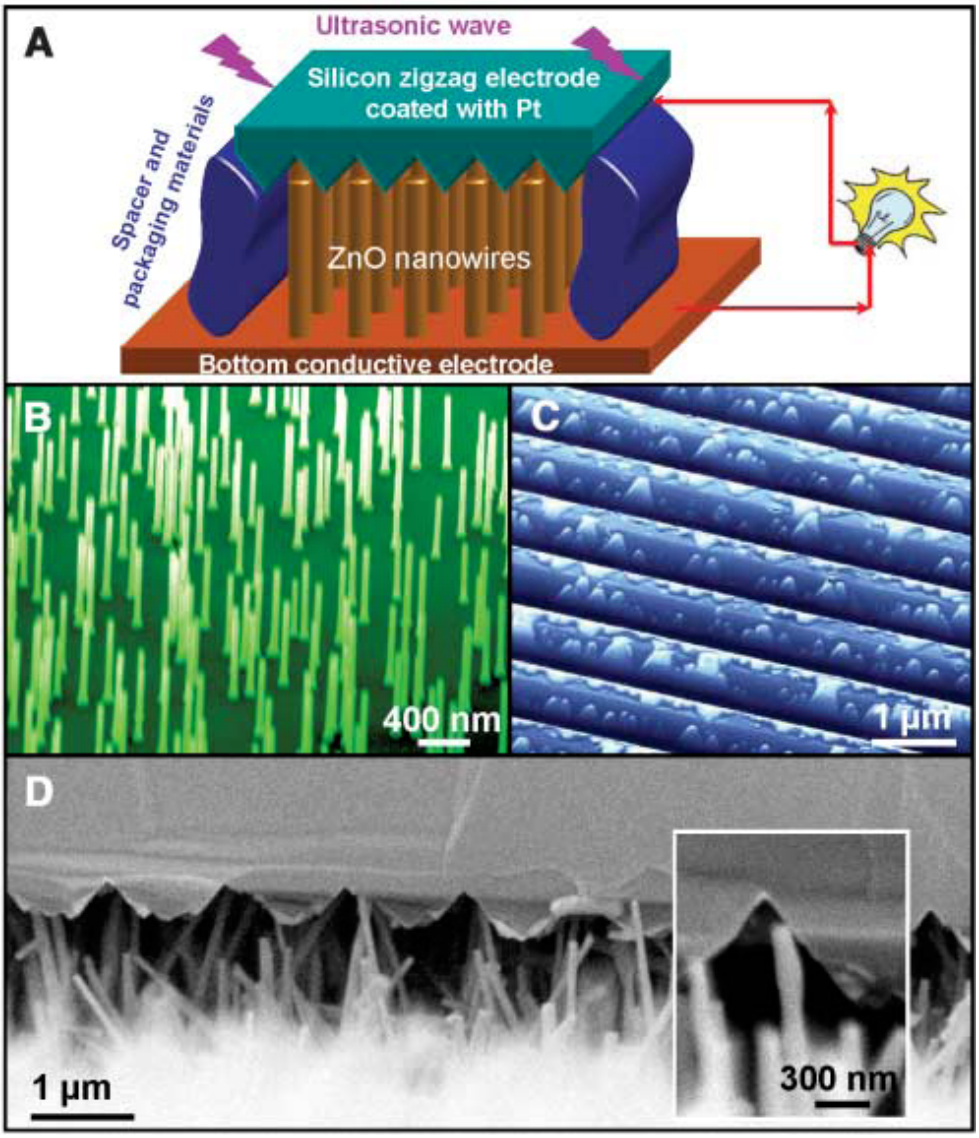

Figure 7.6 (a) A schematic diagram of the design and structure of the nano-generator. (b) Aligned ZnO NWs grown on a GaN substrate. (c) A zigzag trenched electrode after being coated with 200 nm of Pt. (d) A cross-sectional SEM image of the nano-generator. (Inset) A typical NW that is forced by the electrode to bend.

7.1.4 Results and discussion

Figure7.7, (a) to (c), shows four possible configurations of the contacts between a NW and the top electrode. When subject to the excitation of an ultrasonic wave, the top electrode can move down and push the NW I, which leads to a lateral deflection of NW I. This, in turn, creates a strain field across the width of NW I, with the NW outer surface being in tensile strain and its inner surface in compressive strain. The establishment of the strain across the NW results in an establishment of a piezoelectric field along the NW, which produces a piezoelectric potential across the NW. When the electrode makes contact with the stretched surface of the NW, which has a positive piezoelectric potential, the Pt metal-ZnO semiconductor interface is a reversely biased schottky barrier, resulting in little current flowing across the interface. This is the process of creating, separating, preserving, and accumulating the charges. With further pushing by the electrode, the bent NW I will reach the other side of the adjacent tooth of the zigzag electrode. In such a case, the electrode is also in contact with the compressed side of the NW, where the metal/semiconductor interface is a forward-biased schottky barrier, resulting in a sudden increase in the output electric current flowing from the top electrode into the NW. This is the discharge process.

Analogous to the situation described for NW I, the same processes apply to the charge output from NW II. NW III is chosen to elaborate the vibration/resonance induced by the ultrasonic wave. When the compressive side of NW III is in contact with the electrode, the same discharge process as that for NW I occurs, resulting in the flow of current from the electrode into the NW (Figure 7.7 (c)). NW IV, which is short in height, is forced (without bending) into compressive strain by the electrode. In such a case, the

piezoelectric voltage created at the top of the NW is negative. Thus, across the electrode-ZnO interface, a positively biased schottky barrier is formed; hence, the electrons can flow freely across the interface. As a result, electrons flow from the grounded substrate electrode into the NW as well as into the top zigzag electrode as the deformation occurs. This discharging process, if substantial, may also contribute to the measured current. In each of the four cases described in Figure 7.7 (a) to (c), all of the currents are added up in the same phase. An equivalent electric circuit is shown in Figure 7.7 (d) to illustrate the measurements and outputs of the nano-generator. The NWs producing current in the nano-generator are equivalent to a voltage source V_s plus an inner resistance R_i that also contains the contact resistance between the active NWs and the electrode. On the other hand, there are a lot of NWs that are in contact with the electrode but can not be bent or move freely; thus, they do not actively participate in the current generation, but they do provide a path for conducting the current. These NWs are simply represented by a resistance R_w that is in parallel with the portion of the circuit that generates power. A resistance R_c is introduced to represent the contact resistance between the electrode and the external measurement circuit. The capacitance in the system is ignored in the circuit in order to simplify the discussion about the dc measurement. The current and voltage outputs of the nano-generator are shown in Figure 7.7 (e) and (f), respectively, with the ultrasonic wave being turned on and off regularly. A jump of ~0.15 nA is observed when the ultrasonic wave was turned on, and the current immediately falls back to the baseline once the ultrasonic wave is turned off. Correspondingly, the voltage signal exhibits a similar on and off trend but with a negative output of ~0.7 mV. The negative sign of the voltage is consistent with the mechanism presented in Figure 7.7 (c).

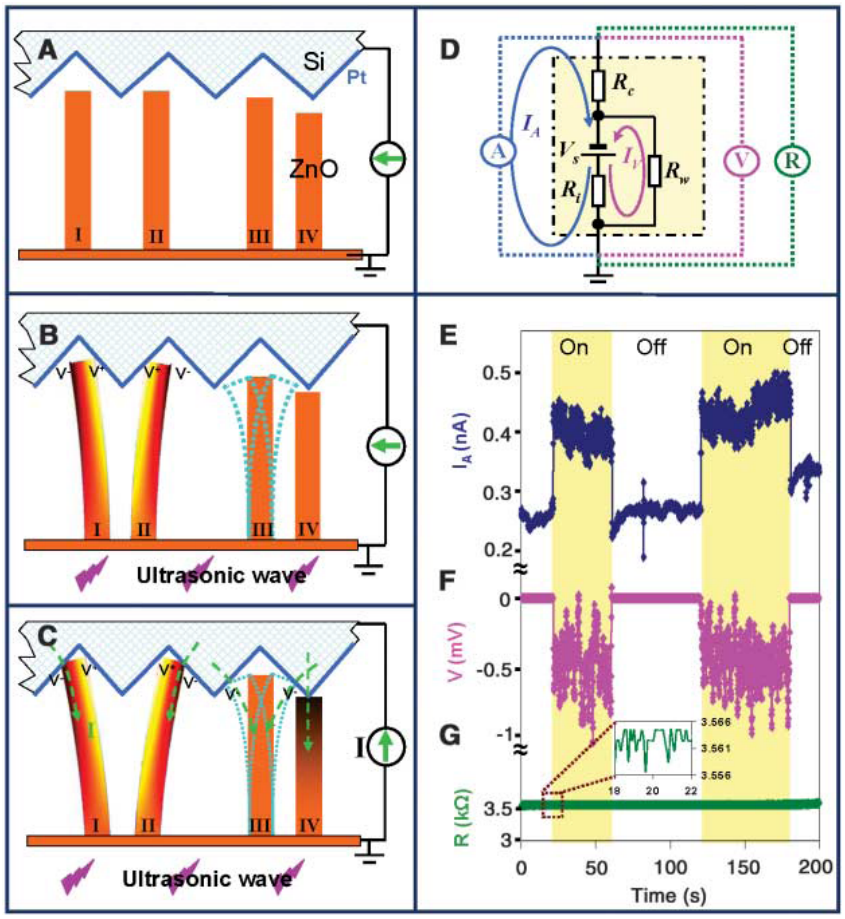

Figure 7. 7 (a) Schematic illustration of the top electrode and the four types of NW configurations, (b) Piezoelectric potential created across NWs I and II under the push or deflection of the electrode, (c) Schematic of NW under vibration, d) Equivalent circuit of the nanogenerator and the setup for measuring the output current I, output voltage V, and resistance R. (e to g) I, V, and R measured with the connections shown in (d).

7.2 An Integrated Nano-generator in Bio-fluid

As mentioned in the beginning of the chapter, operational nano-generators in fluidic environment are desired for certain bio-medical applications. The following experiment demonstrates that through proper packaging techniques, it is possible to operate the nano-generators in bio-fluid.

The nano-generator is modified from our original model composed by vertical aligned ZnO NWs and a Pt-coated zigzag top electrode, as described in detail in [77]. The nano-generator core is completely packaged by a polymer to prevent the infiltration of bio-fluid into the nano-generator. The polymer also has certain flexibility to remain free of relative movement between the ZnO NWs and the top electrode. As shown in Figure 7.8 (a), the nano-generator is placed inside a container filled with 0.9% NaCl solution, which is a typical bio-compatible solution. The substrate and the top electrode are connected by a waterproof extension cord to the outside of the container and marked as the positive and negative electrode, respectively. The definition of the two electrodes is done according to the flow of the current in the external circuit, which is always from the bottom substrate to the top electrode due to the rectifying effect of the schottky barrier between the ZnO NWs and the Pt in the core of the nano-generator.

An ultrasonic stimulation is applied through the bottom of the container with a frequency of ~41 kHz. The ultrasonic wave transports through the fluid and triggers the vibration of the electrode and NWs to generate electricity. The performance of the nano-generator is characterized by measuring the short circuit current I_{sc} and the open circuit voltage V_{oc}. As illustrated in Figure 7.8 (a), during the measurements, the current/voltage meter is forward connected (positive and negative probes are connected to the positive and negative electrodes, respectively) and reversely connected (positive and negative probes are connected to the negative and positive electrodes, respectively) to the two electrodes of the nano-generator. The corresponding I_{sc} and V_{oc} signals are shown in parts (b) and (c) of Figure 7.8, respectively. After the ultrasonic wave is switched on, the current output peak reaches as high as 17 nA, with an average output of ~9 nA and a

"noise/ instability" within 4 nA (pink line in Figure 7.8 (b)). When the current meter is reversely connected, the current signal with the same amplitude is received but reversed in sign (blue line in Figure 7.8 (b)). This measurement clearly eliminates the effects from measurement system error, and confirms that the current is generated by the nano-generator. The corresponding voltage output is rather low and noisy compared to the current signal. As shown in Figure 7.8 (c), a typical voltage level is ~0.1 mV, and a jump of the signal can still be clearly distinguished from the baseline. The voltage exhibits the same sign as the corresponding current signal, and its sign is reversed while the meter connection is switched.

For technological applications, raising the voltage and the current outputs of the nano-generator is essential for raising the output power. If we take each nano-generator as a battery, the most straightforward way to increase the current/voltage is to put them in parallel/serial. This has been demonstrated experimentally. As shown in parts (a) and (b) of Figure 7.9, two nano-generators I and II have been tested under the same experimental conditions. Nano-generator I exhibits an average I_{sc} of ~0.7 nA, and nano-generator II shows a lower noisy signal of 1 nA. These two nano-generators are then connected in parallel (inset of Figure 7.9 (c)) and tested under the same condition again. The resultant output current reaches an average of ~1.8 nA, which is the sum of the two individual outputs (Figure 7.9 (c)). This concept is further proved by anti-parallel connecting nano-generator I and nano-generator II (inset of Figure 7.9 (d)). Since the magnitudes of the I_{sc} of the two nano-generators are very close, the total current is mostly cancelled out by the "head-to-tail" connection in parallel, and the received signal is around the baseline (Figure 7.9 (d)), just as we expect. If more NWs are located in the activate position when

packaging the top electrode, the output current can be improved by several times. As shown in Figure 7.9 (e), with a better assembly, nano-generator III exhibits an average I_{sc} of ~4 nA. Once nano-generator III is added to the parallel connection with nano-generator I and nano-generator II (inset of Figure 7.9 (f)), their total output current is the sum of the three nano-generators (5.9 nA ~ 0.7 nA + 1 nA + 4 nA), as shown in Figure 7.9 (f).

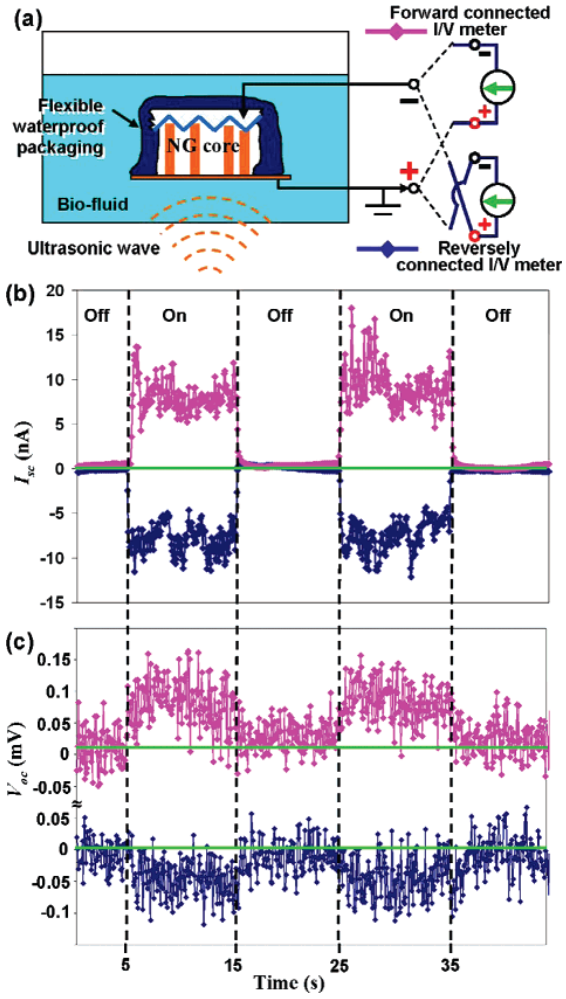

Figure 7.8 (a) A schematic of a nano-generator that operates in bio-fluid and the two types of connections used to characterize the performance of the nano-generator. The pink and blue curves represent signals from the forward connected current/voltage (I/V) meter and the reversely connected I/V meter, respectively. (b, c) The short circuit current and the open circuit voltage measured by the two types of connections when the ultrasonic wave is turned on and off.

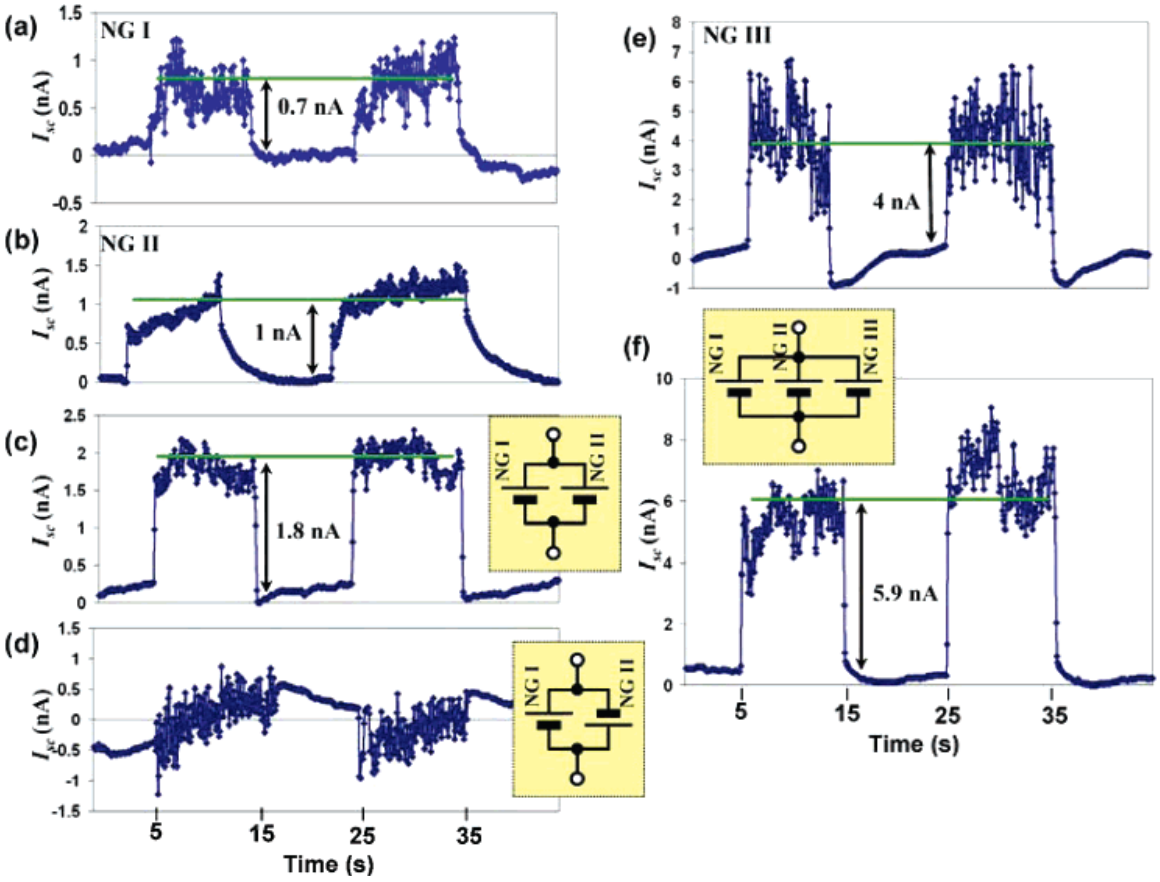

Figure 7.9 (a, b) The current signal measured from two individual nano-generators, I and II. (c, d) The current signal measured from parallel and antiparallel connected nano-generators I and II, respectively. (e) The current signal measured from nano-generator III with a better performance. (f) The current signal measured from the parallel connected nano-generators I, II, and III.

This series of experiments demonstrate that the short circuit current can be effectively improved by parallel connecting multiple nano-generators. This sets the platform for developing three-dimensionally stacked nano-generators. Although the voltage signals are much noisy than the current signal, the increasing trend can still be clearly distinguished when nano-generators are connected in serial. As shown in Figure 7.10 (a), a single nano-generator gives a very noisy voltage output of only ~0.04 mV (nano-generator I). When two similar nano-generators (I and II) are connected in serial,

their output voltage is almost doubled to an average value of 0.07 mV (Figure 7.10 (b)). Once the nano-generator III is added to the serial, the resultant voltage output clearly jumps above the baseline and reaches an average of ~0.18 mV. Therefore, similar to the current output, the open circuit voltage can be effectively improved by connecting multiple nano-generators in serial.

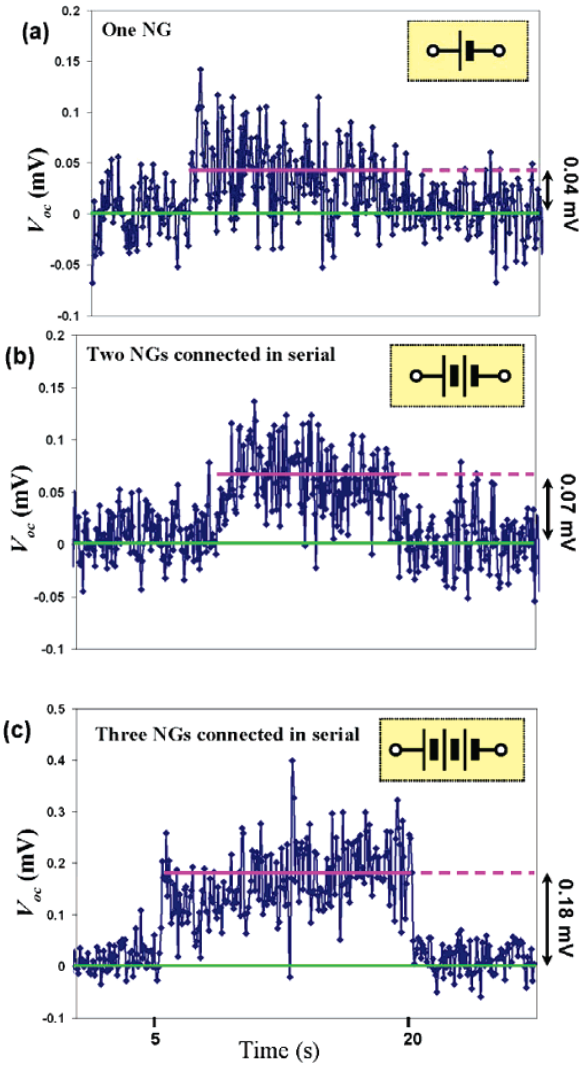

Figure 7.10 The open circuit voltage measured from an integrated nano-generators system. (a-c) The voltage signal measured from one, two, and three serial connected nano-generators. The connection configurations are schematically shown in the insets.

7.3 Chapter Summary

This chapter starts with the motivation behind the design of nano-generators, followed by the fabrication of the top electrode, which is an essential component of the nano-generator. The assembly as well as the test setup is subsequently explained. The detailed working mechanism of the nano-generator is then discussed. Four possible configurations of ZnO NWs under sonication are proposed. The second part of the chapters introduces the nano-generator which is hermitically packaged. This newly designed nano-generator has the capability of operating in bio-fluid.

CHAPTER VIII

CARRIER DENSITY AND SCHOTTKY BARRIER ON THE PERFORMANCE OF THE NANO-GENERATOR

Having demonstrated the operational capability of nano-generators in air and in bio-fluid sets the first step toward the application of these newly invented devices in practical fields. It is, however, still far from to drive the electrical devices even in nanoscale [78]. Therefore, having nano-generators with much improved output power is highly desired. To thoroughly understand the mechanism as well as the factors that govern the performance of nano-generators is vitally important in improving the output characteristics of nano-generators. The first half of the chapter presents the work in investigating the relationship between the carrier density of the NWs, the schottky barrier hight and the output characteristics of nano-generators. A high power nano-generator together with a proposed model is discussed in the second half of the chapter.

8.1 Relationship between Carrier Density, Schottky Barrier and the Output of Nano-generator

8.1.1 Motivation

The mechanism of the nano-generators is based on two important physical quantities. One is the height of the schottky barrier, which needs to be high enough to hold the charges from leaking. Second, the conductivity and carrier density of the ZnO

NW are adequately low in the first step to preserve the piezoelectric potential distribution in the NW from being "neutralized" by the freely flowing charge carriers, which are electrons for n-type ZnO, but they need to be high enough to transport the current under the driving of the piezoelectric potential in the charge releasing process. In this section, we designed a series of experiments to tune the height of the schottky barrier and the carrier density by UV irradiation to study their effects on the performance of the nano-generator. We experimentally show that a schottky diode between the top metal electrode and the NW arrays is a must for the nano-generator, whereas the carrier density has an optimum value at which the output of the nano-generator is expected to be maximized. A testing criterion is established for determining the effectiveness of a nano-generator for generating current.

8.1.2 Experiment Design

The aligned NW arrays to be used for the experiments are grown epitaxially on an optically transparent AlN/sapphire substrate using a method reported elsewhere [76]. The bottom of the substrate is polished for enhancing the optical transparency. At the roots of the NWs, a thin layer of ZnO film is also grown simultaneously, which serves as a common electrode for the electrical measurements. Our fabrication of the DC nano-generator follows the methodology developed in previous chapter. A Pt coated Si top electrode is aligned on top of the ZnO NWs. A flexible spacer is placed between the top electrode and the AlN/sapphire substrate to ensure a proper space required for the nano-generator. The device is then packaged with a water-proof polymer. The entire nano-generator is mounted on a UV-transparent quartz slide (SPI 01016-AB quartz slide) before testing. The packaged nano-generator is placed upside down in a well isolated

water bath, with the quartz slide and AlN/substrate facing up so that the UV light is able to penetrate the slide and reach the core of the nano-generator, as shown in Figure 8.1 (a). The UV light source (100 W long wave mercury spot lamps) is placed 5 cm above the water surface. A 41 kHz ultrasonic wave generator is used as the source to excite the nano-generator from the bottom of the water bath. The transmission spectrum from 200 to 800 nm is measured to ensure that the UV reaches the ZnO NWs, as shown in Figure 8.1 (b). Then the UV transmittance of the AlN/sapphire substrate is measured by stacking the substrate on a UV transparent quartz slide, as shown by the red curve in Figure 8.1 (b), where the oscillation in the measured data is due to the interference of the light reflected from the substrate and the slide. Finally, the UV transmittance is measured for two parallel plates filled with water between them. Due to the reduced total reflection in the water and plate interface, the measured transmittance is even better than that without water (>100%; dark line). Our measurement data clearly show that the near UV light can effectively penetrate through the substrate and water to reach the ZnO NWs.

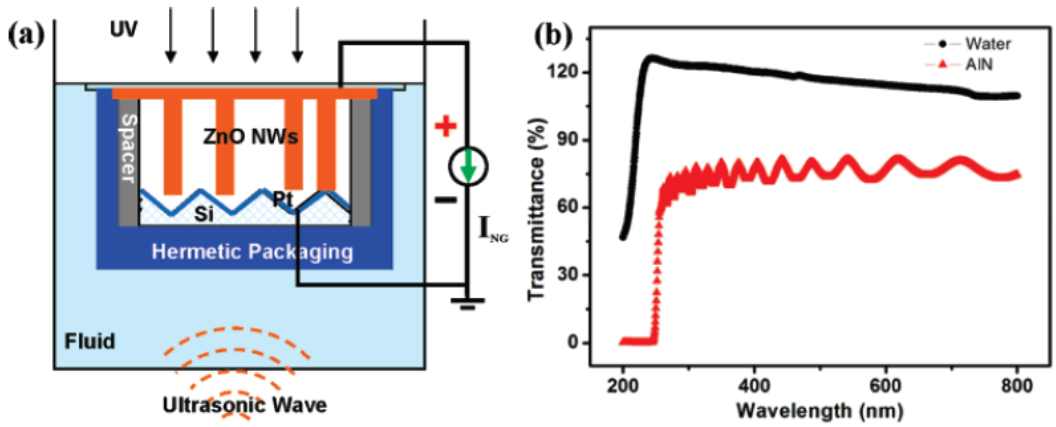

Figure 8.1 (a) The experimental set up for measuring the UV response of an assembled nano-generator in liquid. The nano-generator is placed up side down to ensure the UV illumination from the substrate side to reach the ZnO NWs. (b) The UV transmittance spectra through the AlN/sapphire substrate and water to ensure the penetration of the UV into the core of the nano-generator.

8.1.3 Carrier Density on the Output of the Nano-generator

To evaluate the UV response of ZnO NWs as well as an assembled nano-generator, two experiments have been carried out. Figure 8. 2 (a) shows the UV response of the vertically aligned ZnO NWs and the underlying ZnO thin film by connecting two electrodes at the two ends of the film, as shown in the inset. By applying a constant voltage V_0, the transport current is monitored when the UV is turned on or off. The conductance of the film responds rapidly to change of the UV illumination, and reaches saturation after ~300 s. However, the current decays very slowly after the UV is turned off, possibly due to the following reason. The UV light can effectively create electron-hole pairs in the ZnO and greatly increase the carrier density. After turning off the UV, the electrons and holes would recombine and thus decrease the conductivity. However, some carriers may be trapped in the surface/vacancy states in the ZnO, which greatly delays the electron-hole recombination rate, possibly resulting in a long decay in conductivity.

The long lasting tail in the recovery stage of the conductivity in Figure 8. 2 (a) may indicate that the ZnO synthesized through our approach can hold the charges for an extended period of time before they are completely and entirely neutralized/screened by external electrons. One may suggest that the piezoelectric charges and potential created in a NW hold for an equivalent length of time before being neutralized/screened by external electrons, so that it can effectively gate the charge carriers as proposed for nano-piezotronics [79], giving sufficient time for experimental observation of the effect of the piezoelectric potential across a NW. Such length of time may be even longer than tens to hundreds of seconds.

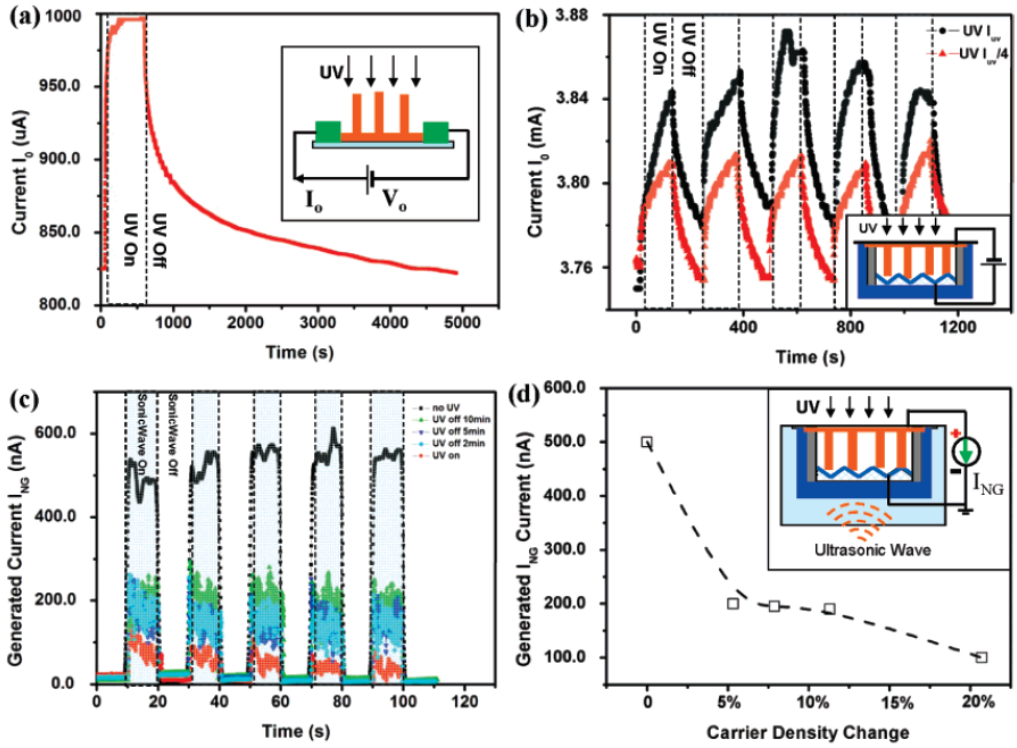

Figure 8. 2 Tuning the transport property of ZnO and an assembled nano-generator by UV excitation. (a) The response of the current transported through a thin ZnO film with NWs on top when subjecting to UV illumination, showing a long delay in the recovering process. The externally applied voltage V_0=2 V. The inset is the measurement set up. (b) The current transported through an assembled nano-generator under an externally applied voltage V_0=2 V when the UV light is tuned on and off. The dark and red curves represent the response curve at full UV intensity I_{UV} and $I_{UV/4}$, respectively. The inset is the measurement set up. Response of the nano-generator output when it is subject to the UV excitation. (c) The current generated by the nano-generator when the ultrasonic wave is turned on and off under different illumination conditions of UV light (see text). A dramatic fact is that the UV illumination reduces the output current by 10-20%. The size of the nano-generator is 6 mm^2. (d) The plot of the nano-generator generated current as a function of the increased percentage of the carried density in the NWs. The inset is the measurement set up.

The second experiment is to characterize the UV response of an assembled nano-generator, as shown in the inset in Figure 8. 2 (b). By reducing the relative UV intensity from I_{UV} to $I_{UV/4}$, the conductance of the nano-generator changes by ~2%. The

conductivity also responds to the on and off of the UV sharply, clearly showing that the UV can effectively increase the carrier density in the nano-generator.

After observing the increased conductivity in nano-generator under the UV irradiation, we investigate the performance of the nano-generator for generating electricity as a function of the carrier density. Figure 8. 2 (c) illustrates the generated current (I_{NG}) of a nano-generator when subject to the ultrasonic wave excitation by changing the UV irradiating condition. When the UV light is off for an extended period of time, the generated current is ~500 nA for a nano-generator with 6 mm^2 in size, corresponding to an output current density of 8.3 $\mu A/cm^2$. This value is about 20 times higher than that reported previously [80]. The key to obtaining a high output current density is to have NWs that are uniform in size and with patterned distribution on substrate that matches the design of the top electrode. The generated current drops to as low as 30~80 nA as soon as the UV light is turned on. At the same time, we monitor the generated current I_{NG} after the UV is turned off for 2, 5, and 10 min, and the generated current increases to ~180, 190, and 205 nA, respectively. Such a gradual increase in the generated current corresponds to the slow decay in the conductivity as shown in Figure 8. 2 (b). This set of experiments apparently shows that an increase in conductivity, e.g., the carrier density, reduces the output current of a nano-generator. By extracting the relative change in the carrier density from Figure 8.2 (a) and the correspondingly measured nano-generator output I_{NG} from Figure 8.2 (c), Figure 8.2 (d) illustrates the monotone decrease relationship between the increased percentage in the carrier density and the output current I_{NG}. This result indicates that the carrier density in ZnO is one of the key characteristics that dictate the output power of a nano-generator. A too high carrier density would

screen the piezoelectric charges, resulting in a lower or even vanishing output current. However, a too low carrier density would increase the inner resistance and greatly decrease the output current. Therefore, there should be an optimum choice of the NW carrier density or the conductivity to maximize the NG output.

In a separate experiment, the output of a nano-generator is monitored when the ultrasonic wave is continuously on but with the UV being turned on and off, as shown in Figure 8.3. The data reproducibly show that the UV irradiation reduces the output current by 30-45%.

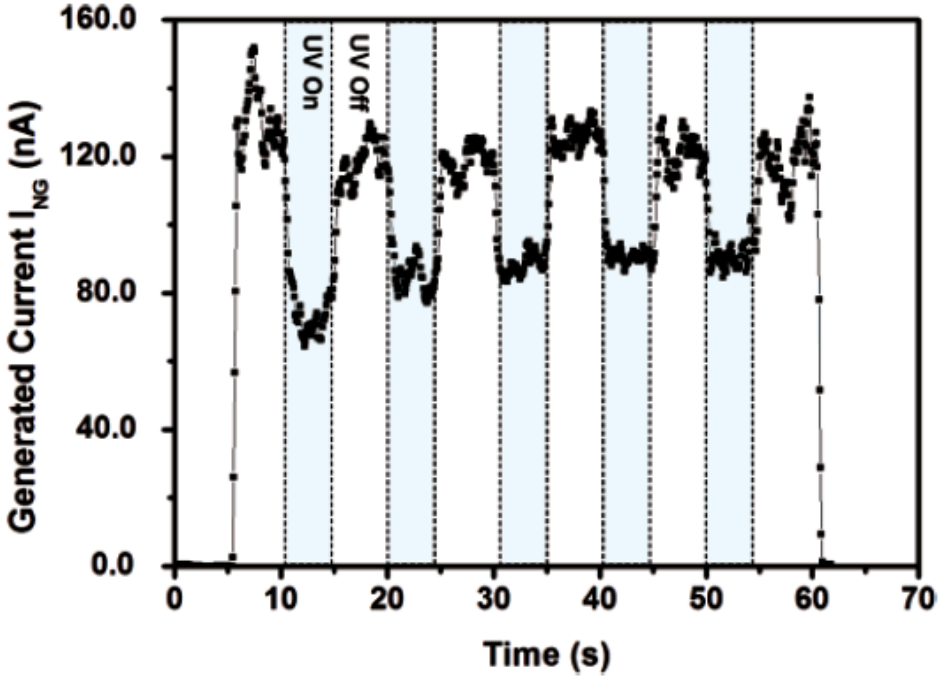

Figure 8.3 Output of a NG as excited by ultrasonic wave when the UV light was turned on and off. The UV light can reduce the output current 30-45%, indicating increasing of carrier density is not beneficial for improving the output power.

8.1.4 Schottky Barrier on the Output of the Nano-generator.

The Schottky contact between the metal contact and ZnO NW is another key factor to the current generation process. Investigating how it affects the performance of the a nano-generator will provide effective guidance in designing and fabricating high output nano-generators. We characterize the I-V characteristic of a set of nano-generators to illustrate the effects of schottky barrier for current generation. Figure 8.4 (a) shows the I-V characteristics of a nano-generator that generates output current (top inset of Figure 8.4 (a)). The experimental setup for the measurement is shown in the inset at the lower right corner in Figure 8.4 (a). The nano-generator exhibits a schottky-like I-V characteristic, which means that the nano-generator has different responses for forward and reverse biases. When illuminated by UV, the nano-generator exhibits an increased conductance, and its schottky-like rectifying effect is largely reduced due to the increased conductance. Alternatively, for a "defective" nano-generator that does not produce current in responding to ultrasonic wave, its I-V characteristic is clearly ohmic even prior to UV illumination (Figure 8.4 (b)). By examining over 10 nano-generators, their I-V characteristics reliably indicate if the nano-generators are effective for producing current. This study establishes a criterion for identifying the working nano-generators from the defective ones.

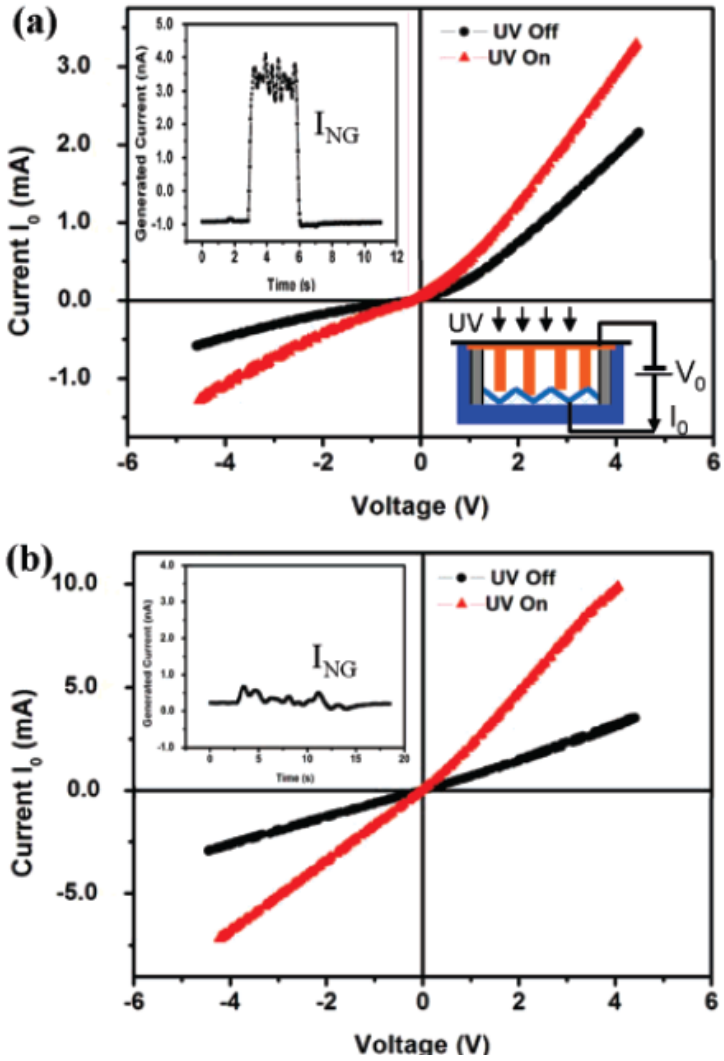

Figure 8.4 The I-V characteristic of an assembled nano-generator for identifying its performance for producing current. (a) For a nano-generator that is actively generating current, as shown in the inset, its I-V curve when the ultrasonic wave was off clearly shows a Schottky diode behavior. The UV light not only increases the carrier density (or conductivity) but also reduces the barrier height. (b) For a "defective" nano-generator that does not produce current, the I-V curve shows a clearly Ohmic behavior. The UV light clearly increases the conductivity as well.

To examine the role played by the schottky barrier in the nano-generator, we use the AFM-based manipulation and measurement system as used in our first study for demonstrating the piezoelectric nano-generator [32] (Figure 8.5 (a)). When a 100 nm thick Pt coated Si tip is used to scan the NWs in contact mode, voltage peaks are

observed (Figure 8.5 (b)), and the output voltages are in the order of ~ -11 mV (the negative sign means that the current flowed from the grounded end through the external load). By changing the tip to an Al-In (30 nm/30 nm) alloy coated Si tip, the ZnO NWs show no piezoelectric output (Figure 8.5 (c)). In order to understand the two distinct performances of the two types of scanning tips, we have measured their corresponding I-V characteristics with the ZnO NWs. To ensure the stability of the contact, we use a large electrode that is in contact with a group of NWs, as shown in Figure 8.5 (d). The Pt-ZnO contact clearly presents a schottky contact behavior (Figure 8.5 (e)), whereas the Al-In- ZnO is an ohmic contact. In reference to the piezoelectric output presented in Figure 8.5 (b), (c), we conclude that a schottky contact between the metal electrode and ZnO is a must for a working nano-generator.

8.1.5 The Relationship between the UV Illumination and the Schottky Barrier Height

As illustrated in the last section, the presence of a schottky barrier between the metal electrode and the ZnO NWs is a key for determining the performance of a nano-generator. We now examine the influence of the UV light on the performance of a schottky diode. For this purpose, we use a pair of Au electrodes interconnected by a ZnO NW, and a schottky diode based device was fabricated (inset in Figure 8.6). The schottky diode characteristic of the NW (dark curve) may be produced by the asymmetric contacts of the ZnO NW with the two electrodes [42]. When being illuminated by the UV light, the conductance of the device is improved over 20 times (red curve in Figure 8.6). More importantly, the threshold voltage of the diode has been greatly reduced from close to 1 V (without UV) to almost 0 (with UV; Figure 8.6), and the I-V curve shows an ohmic like

behavior. Therefore, a weakening or disappearing rectifying effect of the diode is likely to be the reason why the performance of the nano-generator as shown in Figure 8.2 (c), (d) deteriorates with the increase of the UV generated carrier density.

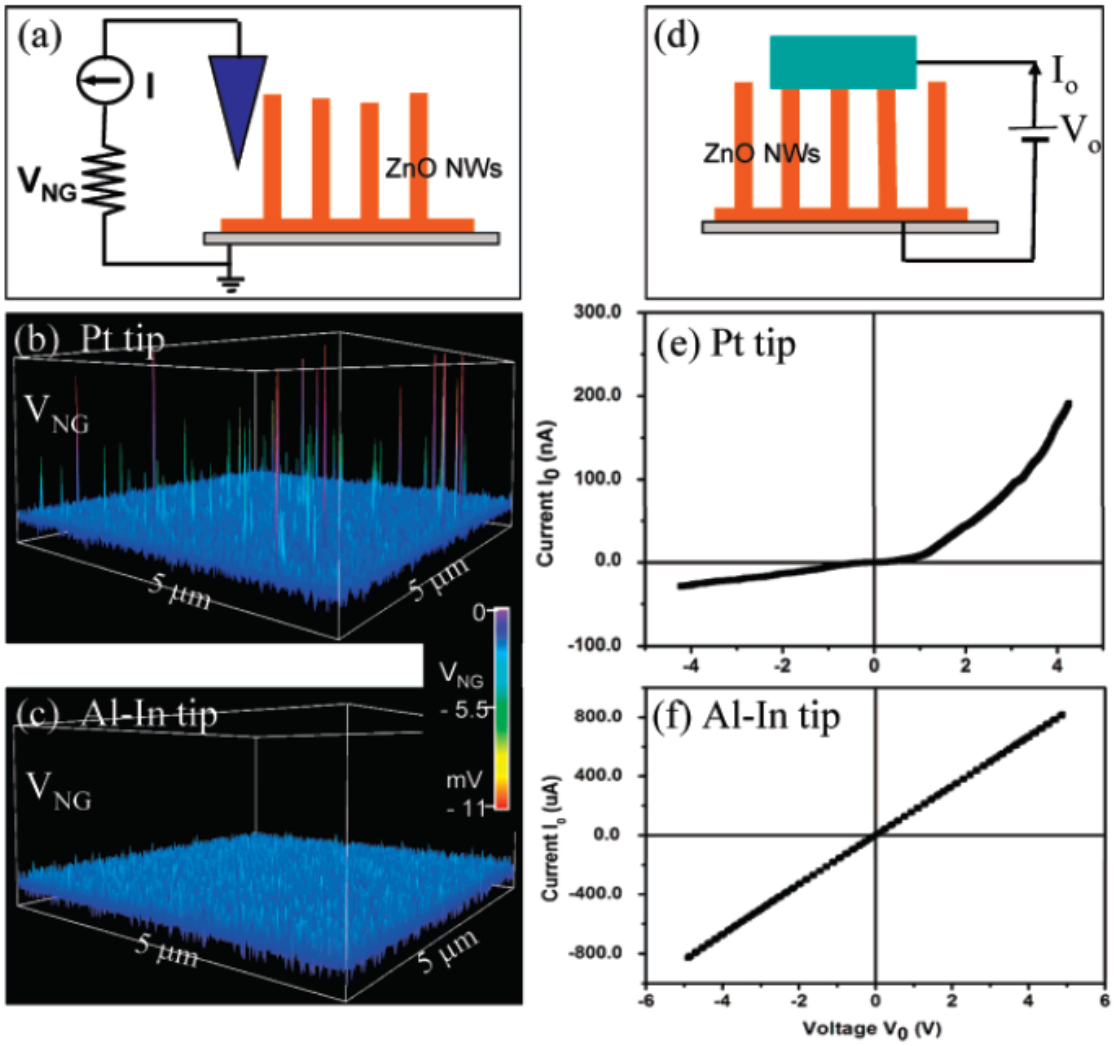

Figure 8.5 (a) The AFM-based measurement set up for correlating the relationship between the metal-ZnO contact and the nano-generator output. (b) The output potential generated by a ZnO NW array when scanned by a Pt coated Si tip. (c) No output potential is generated by the ZnO NW array when scanned by an Al-In coated Si tip. (d) The experimental set up for characterizing the I-V transport property of the metal-ZnO NW contact. (e) The I-V curve of a Pt-ZnO NW contact, showing schottky diode effect. (f) The I-V curve of an alloyed Al/In-ZnO NW contact, showing ohmic behavior.

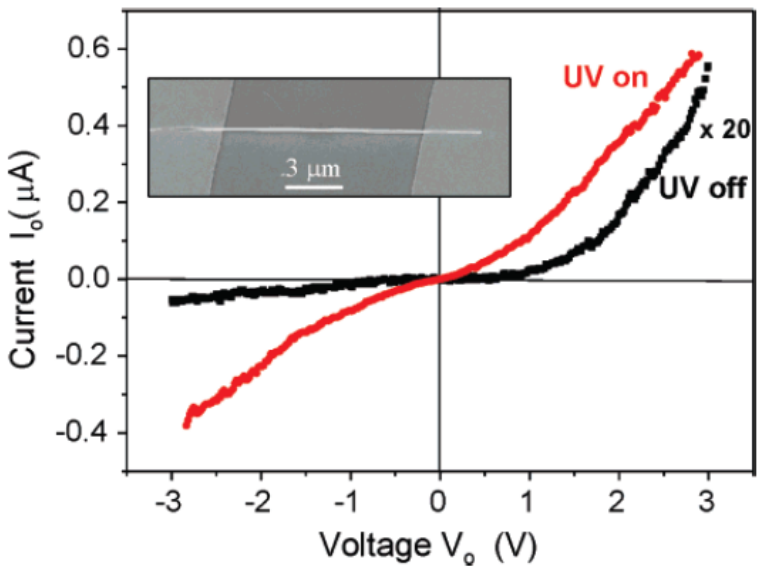

Figure 8.6 A two-electrode-based device fabricated using a ZnO NW for measuring its transport property when subjecting to the UV illumination. An SEM image of the device is shown in the inset. The asymmetric contact at the two ends results in a schottky diode. The UV not only increases the carrier density but also reduces the barrier height at the interface.

8.1.5 Conclusions

In summary, by assembling aligned ZnO NW array based nano-generators that are transparent to UV light, we investigate the performance of the nano-generator by tuning its carrier density and the transport property of the schottky barrier between the metal electrode and the NWs. The presence of a schottky diode between the top zigzag metal electrode and the ZnO NWs is mandatory for the effective operation of the nano-generator. UV light not only increases the carrier density in the ZnO but also reduces the barrier height between the metal electrode and the ZnO. A reduced schottky barrier height greatly weakens the function of the barrier for preserving the piezoelectric potential in the NW. A replacement of a schottky contact by an ohmic contact overrides the role played by the barrier for accumulating the piezoelectric charges. If there were no

charge accumulation in the first process, no charge would be released in a later stage. Our study shows that identifying the existence of the schottky diode transport property of a nano-generator is an effective means for identifying if the nano-generator is good or defective. An increased carrier density speeds up the rate at which the piezoelectric charges are screened/neutralized. However, a very low carrier density may improve the local piezoelectric potential and prevents the flow of current through the NWs, as well as increases the inner resistance of the NWs and possibly the contact resistance at the interface. Therefore, there should be an optimum choice of NW conductance for maximizing the output of the nano-generator. NWs with excellent conductivity may greatly reduce the lifetime of the piezoelectric charges, resulting in very small or no output current. A comprehensive computer simulation that takes into consideration the dynamics of charge transport is necessary for predicting the value of the optimum conductance.

8.2 A Circuit Model of the Nano-generator

8.2.1 A High Power Nano-generator

The design and fabrication of nano-generators follow a similar method as in previous chapter. To ensure the quality of the nano-generator, the NW arrays are carefully chosen so that the variance of the average length of the NW is minimal. This is to maximize the number of NWs that would contribute to the power generation process while minimizing the parasitic capacitance that could bring down the voltage output. The nano-generator is then placed in the water bath to measure the closed circuit current and open circuit voltage. The ultrasonic wave generator is periodically turned on every other

15 seconds. Measurements are taken under both connection polarities to rule out any possible artifact caused by the measurement setup. Figure 8.7 (a) shows the closed circuit current when the ultrasonic wave is turned on and off. The data clearly indicate that the current output is originated from the nano-generator as a result of the ultrasonic wave excitation, as the output coincides with the working cycle of the ultrasonic wave generator. Furthermore, the output signal switches in sign from positive to negative when the measurement polarity is switched from forward to reversed connection. Finally, there is no destabilization of the output amplitude over time in the graph. A similar pattern in the open circuit voltage output is also observed, as shown in Figure 8.7 (b). Both the current and the voltage outputs exhibit high levels for this type of nano-generator, with a current of ~500 nA and voltage of ~10 mV. Considering the effective area of the nano-generator (6 mm^2), it is equivalent to a current generation density of ~8.3 $\mu A/cm^2$, which is ~20 times higher than previously reported [80]. A power generation density of ~83 nW/cm^2 is reported, which shows a great potential to power nanoscale sensors [78].

The output current of the nano-generator is the sum of those contributed by all of the active NWs, while the ultimate output voltage is determined by individual NW. Our previous calculation shows that, based on an assumption that ZnO is nonconductive, the output voltage can be in the range of a fraction of a volt [81]. However, our experimental observation gives a much lower output in 1~20 mV. We now propose the following model to explain the received small output voltage.

8.2.2 Circuit Model of a Nano-generator and Guidelines for Improvement

Here we consider a voltage generation model. Figure 8.7 (a) represents three possible situations for any individual NW during the voltage generation process. The first two stand for the NWs that are generating output current. They are illustrated by an equivalent circuit model shown in the left of Figure 8.7 (b). The circuit consists of a capacitor (c_0), which represents the capacitance between the NW and the electrode, two resistors (r_c and r_0), which represent the contact and system resistance, respectively, a voltage source (v_0), which represents the voltage created in the NW, and a diode, which represents the schotty contact between the NW and the Pt coated electrode. The second possible situation is illustrated by NW III in Figure 8.7 (a), where the NW does not participate in the voltage generation process. Instead, the NW is in touch with the top electrode constantly. The situation is modeled by an equivalent circuit similar to NWs I and II, except with no voltage output. NW IV in Figure 8.7 (a) illustrates the third possible configuration between the NW and the top electrode, where the NW neither participates in the voltage generation process, nor in contact with the top electrode. Under such circumstance, a capacitor (c_0) is used to represent the capacitance between the NW and the top electrode. Figure 8.7 (b) is the corresponding equivalent circuit of Figure 8.7 (a). In addition to the circuits that are from the NWs, a capacitor which represents the system capacitance (c_s) that comes from the measurement setup is added at the right-hand side. To simplify the calculation, it is assumed that all the variables that are represented by the same symbol have the same quantity, i.e. the capacitance (c_0) is the same for all individual NWs. In reality, the resistance and capacitance for each NW can be different. Let q_0 denote the charge generated from each NW during the bending

process. Therefore, according to the assumption, q_0 is the same for all of the NWs. Under low frequencies, the voltage generated by a single NW can be written as

$$v_0 = \frac{q_0}{c_0} \quad . \tag{1}$$

If a total of n NWs all simultaneously contribute to the energy generation process, and if the system capacitance c_s is negligible, the measured voltage would be

$$v_0' = \frac{nq_0}{nc_0} = \frac{q_0}{c_0} = v_0 \quad . \tag{2}$$

Therefore, for any nano-generator under such configuration, the maximum voltage output of the device is equal to the maximum voltage output of each individual nanowire v_0.

For a non-ideal case, such as in our experiment, let n_1 denote the number of active NWs that output electricity, and n_2 the number of inactive NWs that do not output electricity, as shown in Figure 8.7 (b), the system voltage output (v_s) is then

$$v_s = \frac{n_1 q_0}{(n_1 + n_2)c_0 + c_s} \quad . \tag{3}$$

For any given nano-generator, let n be the total number of NWs, $n = n_1 + n_2$. Therefore, equation (3) can be rewritten as

$$v_s = \frac{n_1 q_0}{nc_0 + c_s} \quad . \tag{4}$$

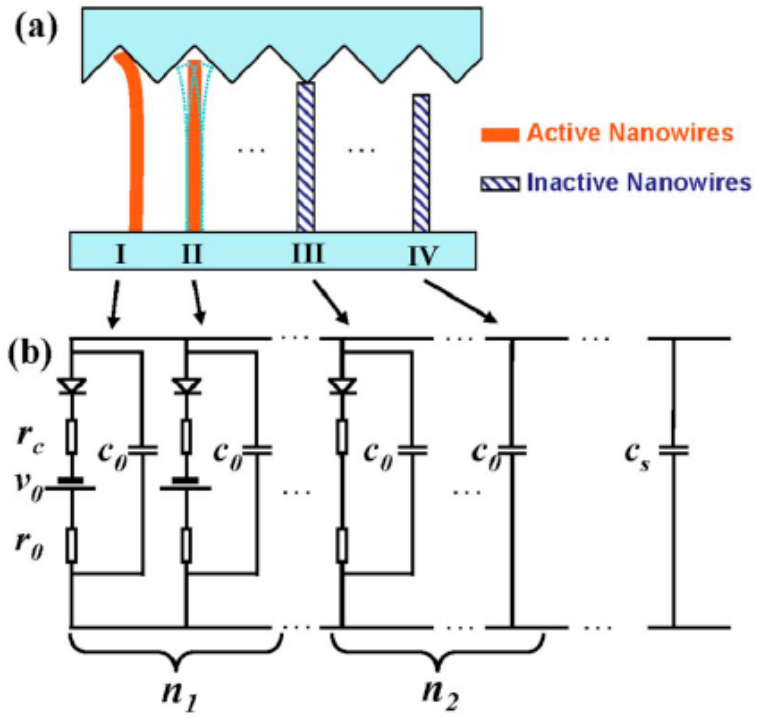

Figure 8.7 The equivalent circuit analysis of a nano-generator. (a) Three different types of NWs are presented: NWs I and II are active NWs that output electricity; NW III is in contact with the top electrode but does not produce current; and NW IV is not in contact with the top electrode. (b) The corresponding circuit model, where c_s is added to represent the system capacitance.

Equation (4) gives a guideline for increasing the voltage output (v_s). Combining with the existing knowledge on the relationship between the morphology of ZnO NW arrays and the performance of a nano-generator, we summarize the key factors to boost the voltage output as follows:

(i) Increase the number of active NWs for participating electricity generation. This is crucial in determining the voltage output performance. There are two possible approaches to increase n_1. One is to utilize ZnO NW arrays with uniform size, especially uniform in length. The other approach is to pattern the NW arrays according to the

dimension and shape of the top electrode. An increase in the output voltage will be accompanied with an increase in the output current that is directly proportional to n_1.

(ii) Increase the charge generated from individual NW during the vibration process. This may be possible by increasing the magnitude of the external excitation, because the magnitude of the generated voltage is proportional to the deflection of the NW [81].

(iii) Optimize of the electric conductivity of the ZnO NW arrays. Our previous work [82] has indicated the relationship between the carrier density and the performance of a nano-generator. It is expected that by tuning the carrier density to an optimal value, both the current and voltage outputs can be increased significantly. But the optimum value of the conductivity needs to be modeled with consideration of the charge transport dynamics.

(iii) Decrease the capacitance between individual NW and the top electrode as well as the system capacitance. The size of the electrodes can make large contribution to the system capacitance. The other factor is the capacitance of the measurement circuit.

8.3 Summary

The first half of the chapter presents the work in investigating the relationship between the carrier density of the NWs, the schottky barrier hight and the output characteristics of nano-generators. A high power nano-generator together with a proposed model is discussed in the second half of the chapter.

CHAPTER IV

CONCLUSION, FUTURE WORK, AND CONTRIBUTIONS

With the increasing need to better understand the phenomena at nanoscale as well as utilize nano-materials for the good of human being, research in nano-field has drawing a lot of attention. Particularly, researchers are getting interested in synthesizing and applying 1D nanostructures for practical applications. ZnO NW with its coupled semiconductive and piezoelectric properties has become one of the most heavily investigated nanostructures lately.

The dissertation is based on the previous work on the synthesis and characterization of ZnO NWs. A practical approach is developed to manipulate as well as prepare the contact formation between the ZnO NW and the underlying metal contacts for research purpose. A systematic study on the oxygen diffusion behavior that affects the stability of ZnO NWs in later applications is carried out. Two applications based on the as-synthesized ZnO NWs are realized and characterized, which are compatible with SOP platform and could be integrated for miniaturized electronic system. Further study on both of the applications is outlined for future work. Finally, the original contributions from the author also summarized in this chapter.

9.1 Summary

Chapter 1 starts with the definition of nanotechnology, which leads to the introduction of ZnO 1D nanostructure. Two properties of ZnO 1D nanostructure are

presented. The first property, which is high surface-to-volume ratio, is commonly found on all 1D nanostructures; while the second property is exclusive for piezoelectric materials, such as ZnO. These two properties lay the foundation for the underlying mechanisms of applications mentioned later in the dissertation. Another aspect of the research, which is the compatibility with SOP technology, is introduced in chapter 1 as well. The introduction starts with the definition of SOP and discusses the advantages of integrating nanostructures with SOP platform for miniaturizing electronic systems. Chapter 1 concludes with the problem statement and the outline of the dissertation.

A comprehensive literature review regarding the synthesis of ZnO nanostructures, particularly ZnO NWs starts chapter 2. Following the review on ZnO NW synthesis, three applications employing ZnO NWs are reviewed. The state-of-the-art status of bio-sensor development concludes this chapter.

Chapter 3 compares two approaches to manipulate the ZnO NWs, both of which are developed for the ZnO NW device fabrication. In addition, two contact preparation methods are discussed as well. Based on the advantages and disadvantages of these two approaches, the micro-manipulation method together with the Pt deposition is chosen for the device preparation for bio-sensor devices.

A systematic study on the oxygen diffusion behavior in ZnO NWs is carried out in chapter 4. This study is based on the motivation of investigating the effect of oxygen in the stability of 1D nanostructures. A finite element analysis (FEA) model is developed based on the oxygen diffusion behavior. The chapter closes with the extrapolation of the oxygen diffusion coefficient in ZnO NW from the experimental and the simulation data.

In chapter 5, the first application based on ZnO wire, which is ZnO bio-sensor, is introduced and discussed. The fabrication processes as well as the experiment protocol are explained in detail. This experiment demonstrates the feasibility of utilizing the ZnO NW to detect specific binding, which can be used to detect potentially any targeted molecule.

Following the previous chapter, chapter 6 takes this concept further by introducing a micro-fluidic channel into the system. The integrated bio-sensor is able to detect potentially any bio-molecules in real-time in ultra-low concentration. In addition, to cater for the industry manufacturing, a more industrial compatible approach, which utilizes ZnO thin films as the platform for the integrated system, is presented. The mechanism that governs both the systems is presented. The similarities as well as the differences between these two platforms are discussed later in the chapter.

Chapter 7 introduces a newly designed nano-generator which can produce continuous output under the excitation of ultrasonic wave. The working mechanism as well as the possible NW configurations in the mechanism is proposed. Finally, an improved package of the nano-generator leads to the operation of the nano-generator in bio-fluid, which has potential applications in bio-related fields.

Chapter 8 tackles the factors that govern the performance of a nano-generator. A schottky contact between the top electrode and the ZnO NW is found to be a key factor for any nano-generator to be operational. The carrier concentration, which can be tuned through the UV illumination, is related to the output characteristics of nano-generators as well. Finally, a circuit model which is based on the previous experimental results as well

as the proposed working mechanism is used to illustrate future guidelines of nano-generator output improvement.

9.2 Future Work

It is impossible to finish any research in a perfect manner. The following work can be done for further research in this area

7.2.1 The Detection Limit of the Bio-Sensor

The work done in chapter 5 and 6 demonstrates the feasibility of using the ZnO wires as well as the ZnO thin film to fabricate bio-sensors. Real-time detection is achieved through the integration of a micro-fluidic channel to the existing platform. It is desirable, however, to investigate the detection limit of the bio-sensor and its relationship with the dimensions of the platforms. Particularly, a systematic study can be carried out in ZnO thin film-based devices since the control over the dimensions of ZnO thin film is much easier than that of ZnO wire/NW.

7.2.2 The High Power Nano-generator

Having demonstrated that nano-generator is able to provide continuous current output is just the first step towards the real application of nano-generators. Further work has to be done based on the guidelines proposed in chapter 8 to bring the output power to a higher level.

The immediate work in this area could be to investigate the relationship between the shape and size of the top electrode and the output characteristics of nano-generators. Being a very important component of the nano-generator, investigating the relationship

between the parameters of the electrode and the performance is also very helpful in designing next generation nano-generators.

9.3 Contributions

Several original contributions have been made through this work to the nano research field. They are listed below

- A novel approach to manipulate 1D nanostrucutres couples with the contact formation process. Better ohmic contact has been achieved via this technique. Compared with existing methods such as DEP, cleaner surfaces of 1D nanostructres can be realized.
- The oxygen diffusion coefficient of ZnO nanodevices is extracted from the fitting between the experimental and the theoretical data. The coefficient is found to be two magnitudes larger than that in the bulk ZnO material. It is expected that such discovery will have significant impact on governing the stability analysis of nanodevices in the future.
- A first time report on using ZnO NWs as the platform for bio-molecule detection. There have been reports on using Si NWs as bio-sensors. However, being a bio-compatible material, the exploration of utilizing ZnO NWs as bio-sensors will increase the ease of integration between the bio-sensor and the biological system.
- A first time report of the integration of a glass based micro-fluidic channel with the ZnO wire/NW and thin film-based devices. A real-time specific detection of streptavidin is demonstrated through these platforms.
- A first report on developing a nano-generator based on ZnO NW arrays that has continuous current output. This is expected to have a significant impact on the

scientific research community due to its novelty and potential application in many fields.

- A first demonstration of the capability of a nano-generator to generate current output in bio-fluid. This work paves the way for the application of n in bio-field.
- An investigation between the carrier concentration, the schottky barrier and the output characteristics of a nano-generator is carried out. A criterion to distinguish the good nano-generators from the bad ones is proposed.
- A circuit model based on the experimental results as well as the working mechanism is proposed. A set of guidelines is created for future improvement of the performance of nano-generators.

The research performed in this work so far has led to 22 publications. These publications include three leading-author journal publications, four leading-author conference papers. There are also several co-authored journal publications as well as conference publications which the author has significant contributions. One paper has published in Applied Physics Letters. One paper has been published in Science Magazine. Two papers have been published in Nano Letters. One paper has been published in the 58th Electronic Components and Technology Conference (ECTC 2008). Two papers have been published in the 57th Electronic Components and Technology Conference (ECTC 2007). One paper has been published in 2006 11th International Symposium on Advanced Packaging Materials. One paper has been published in the 5th International Conference on Electronics Packaging Technology (ICEPT 2005). Several

other journal and conference papers have been published as well. The complete list of publications is:

- J. Liu, P. Fei, J. Zhou, R. Tummala and Z.L. Wang, "Toward high output power nanogenerator", Appl. Phys. Lett., 92 (2008), 173105.
- J. Liu, P. Fei, J.H. Song, X.D. Wang, C.S. Lao, R. Tummala and Z.L. Wang, "Carrier density and Schottky barrier on the performance of DC nanogenerator", Nano Lett. 8 (2008) 328-332.
- J.H. Song, X.D. Wang, J. Liu, H. Liu, Y. Li and Z.L. Wang, "Piezoelectric Potential Output from ZnO Nanowire Functionalized with p-Type Oligomer", Nano Lett., 8 (2008) 203-207.
- Z.L. Wang, X.D. Wang, J.H. Song, J. Liu and Y. Gao, "Piezoelectric Nanogenerators for Self-Powered Nanodevices", IEEE Pervasive Computing, 7 (2008) 49-55.
- J.H. He, Y.Y. Zhang, J. Liu, D. Moore, G. Bao and Z.L. Wang "ZnS/Silica Nanocable Field Effect Transistors as Biological and Chemical Nanosensors", J. Phys. Chem. C., 111(2007) 12152-12156.
- P.X. Gao, J. Liu, B. Buchine, B. Weintraub, Z.L. Wang and J.L. Lee, "Bridged ZnO nanowires Across Trenched Electrodes", Appl. Phys. Lett., 91(2007), 142108.
- X.D. Wang, J. Liu, J.H. Song and Z.L. Wang, "Integrated Nanogenerators in Bio-Fluid", Nano Lett. 7 (2007) 2475-2479.

- J. Zhou, J. Liu, X.D. Wang, J.H. Song R. Tummala, N.S. Xu and Z.L. Wang "Vertically Aligned Zn2SiO4 Nanotube/ZnO Nanowire Heterojunction Arrays", Small, 3 (2007) 622-626.
- X.D. Wang, J.H. Song, J. Liu and Z.L. Wang "Direct-current Nanogenerator Driven by Ultrasonic Waves", Science, 316 (2007) 102-105.
- P.X. Gao, J.H. Song, J. Liu and Z.L. Wang "Nanowire Piezoelectric Nanogenerators on Plastic Substrates as Flexible Power Sources for Nanodevices", Adv. Mater., 19 (2007) 67-72.
- J.H. He, C.L. Hsin, J. Liu, L.J. Chen and Z.L. Wang "Piezoelectric Gated Diode of a Single ZnO Nanowire", Adv. Mater., 19 (2007) 781-784.
- X.D. Wang, J. Zhou, J.H. Song, J. Liu, N.S. Xu and Z.L. Wang "Piezoelectric Field Effect Transistor and Nanoforce Sensor Based on a Single ZnO Nanowire", Nano Lett., 6 (2006) 2768-2772.
- J. Liu, P.X. Gao, W.J. Mai, C.S. Lao, Z.L. Wang and R. Tummala "Quantifying oxygen diffusion in ZnO nanobelt", Appl. Phys. Lett., 89 (2006) 063125.
- J. Zhou, J. Liu, R.S. Yang, C.S. Lao, P.X. Gao, R. Tummala, N.S. Xu, and Z.L. Wang "SiC-Shell Nanostructures Fabricated by Replicating ZnO Nano-objects: A Technique for Producing Hollow Nanostructures of Desired Shape", Small, 2 (2006) 1344-1347.
- C.S. Lao, J. Liu, P.X. Gao, L. Zhang, D. Davidovic, R. Tummala and Z.L. Wang "ZnO Nanobelt/Nanowire Schottky Diodes Formed by Dielectrophoresis Alignment across Au Electrodes", Nano Lett., 6 (2006) 263-266.

- J. Liu, J. Goud, P.M. Raj, M. Iyer, Z.L. Wang and R. R. Tummala, "Real-Time Protein Detection Using ZnO Nanowire/Thin Film Bio-Sensor Integrated with Microfluidic System", Electronic Components and Technology Conference (2008) Accepted
- J. Liu, J. Goud, P.M. Raj, M. Iyer, Z.L. Wang and R. R. Tummala, "Label-Free Protein Detection by ZnO Nanowire Based Bio-Sensors", Electronic Components and Technology Conference (2007) 1971-1976.
- J. Goud, P.M. Raj, J. Liu, R. Narayan, M. Iyer and R.R. Tummala, "Electrochemical Biosensors and Microfluidics in Organic System-on-Package Technology", Electronic Components and Technology Conference (2007) 1550-1555.
- J. Goud, P.M. Raj, J. Liu, M. Iyer, Z.L Wang and R. Tummala, "Conductimetric Detection of Protein and Cancer Cells with Oxide Nanosensors", Mater. Res. Soc. Symp. Proc. (2007) Vol. 1010, V06-09.
- J. Liu, J. Goud, M. Iyer, R. Tummala, and Z.L. Wang, "ZnO nanobelts/wire for electronic detection of enzymatic hydrolysis of starch", 2006 11th International Symposium on Advanced Packaging Materials: Processes, Properties, and Interface (IEEE Cat. No.06TH8875), 2006, 3.
- J. Liu, C.S. Lao, R. Tummala and Z.L.Wang, "Packaging of ZnO nanobelts as nanosensors: synthesis, alignment and characterization" 6th Inter. Conf. Electron. Packaging Technology. (2005) 546-549.
- Zhaoran Huang, Daniel Guidotti, Gee-Kung Chang, Jin Liu, Fuhan Liu, Y-J Chang, and Rao Tummala, "Optical Interconnects Integration on FR4 Board with

MSM Photodetector and Commercial Optoelectronic Devices", (2004) LEOS Summer Topical Meetings, MB2.4, 13-14.

REFERENCES

1. Feynman, R.P., *There's Plenty of Room at the Bottom.* Engineering and Science, 1960. **XXIII**(5).
2. Chan, W.C.W. and S.M. Nie, *Quantum dot bioconjugates for ultrasensitive nonisotopic detection.* Science, 1998. **281**(5385): p. 2016-2018.
3. Gao, X.H., et al., *In vivo molecular and cellular imaging with quantum dots.* Current Opinion in Biotechnology, 2005. **16**(1): p. 63-72.
4. Bruchez, M., et al., *Semiconductor nanocrystals as fluorescent biological labels.* Science, 1998. **281**(5385): p. 2013-2016.
5. Cui, Y., et al., *Nanowire nanosensors for highly sensitive and selective detection of biological and chemical species.* Science, 2001. **293**(5533): p. 1289-1292.
6. Mansilla, H.D., et al., *ZnO-catalysed photodegradation of kraft black liquor.* Journal of photochemistry and photobiology. A, Chemistry, 1994. **78**(3): p. 267-273.
7. Shibata, T., et al., *Characterization of sputtered ZnO thin film as sensor and actuator for diamond AFM probe.* Sensors and Actuators A: Physical, 2002. **102**(1): p. 106-113.
8. Lee, S.S., R.P. Ried, and R.M. White, *Piezoelectric cantilever microphone and microspeaker.* Microelectromechanical Systems, Journal of, 1996. **5**(4): p. 238-242.
9. Ryu, Y., et al., *Next generation of oxide photonic devices: ZnO-based ultraviolet light emitting diodes.* Applied Physics Letters, 2006. **88**: p. 241108.

10. Roszek, B., W.H. de Jong, and R.E. Geertsma, *Nanotechnology in Medical Applications: State-of-the-art in Materials and Devices*. 2005: RIVM.

11. Hutson, A.R., *Piezoelectricity and conductivity of ZnO and CdS* **.** Physical Review Letters, 1960. **4**(10): p. 505-507.

12. Heo, Y.W., et al., *Site-specific growth of Zno nanorods using catalysis-driven molecular-beam epitaxy.* Applied Physics Letters, 2002. **81**(16): p. 3046-3048.

13. Bao, D., H. Gu, and A. Kuang, *Sol-gel-derived c-axis oriented ZnO thin films.* Thin Solid Films, 1998. **312**(1-2): p. 37-39.

14. Kong, Y.C., et al., *Ultraviolet-emitting ZnO nanowires synthesized by a physical vapor deposition approach.* Applied Physics Letters, 2001. **78**: p. 407.

15. Kind, H., et al., *Nanowire ultraviolet photodetectors and optical switches.* Advanced Materials, 2002. **14**(2): p. 158.

16. Arnold, M.S., et al., *Field-effect transistors based on single semiconducting oxide nanobelts.* Journal of Physical Chemistry B, 2003. **107**(3): p. 659-663.

17. Park, W.I., et al., *Schottky nanocontacts on ZnO nanorod arrays.* Applied Physics Letters, 2003. **82**(24): p. 4358-4360.

18. Chen, R.J., et al., *Noncovalent functionalization of carbon nanotubes for highly specific electronic biosensors.* Proceedings of the National Academy of Sciences of the United States of America, 2003. **100**(9): p. 4984-4989.

19. Patolsky, F., G. Zheng, and C.M. Lieber, *Fabrication of silicon nanowire devices for ultrasensitive, label-free, real-time detection of biological and chemical species.* Nat. Protocols, 2006. **1**(4): p. 1711-1724.

20. Patolsky, F., G. Zheng, and C.M. Lieber, *Nanowire sensors for medicine and the life sciences.* Nanomedicine, 2006. **1**(1): p. 51-65.

21. Gao, P., *Piezoelectric Nanostructures of Zinc Oxide: Synthesis, Characterization and Devices*, in *Materials Science and Engineering*. 2005, Georgia Institute of Technology: Atlanta. p. 290.

22. Yi, G.C., C.R. Wang, and W.I. Park, *ZnO nanorods: synthesis, characterization and applications.* Semiconductor Science and Technology, 2005. **20**(4): p. S22-S34.

23. Pan, Z.W., Z.R. Dai, and Z.L. Wang, *Nanobelts of semiconducting oxides.* Science, 2001. **291**(5510): p. 1947.

24. Gao, P.X., et al., *Conversion of Zinc Oxide Nanobelts into Superlattice-Structured Nanohelices*. 2005, American Association for the Advancement of Science. p. 1700-1704.

25. Wang, Z.L., *Zinc oxide nanostructures: growth, properties and applications.* Journal of Physics-Condensed Matter, 2004. **16**(25): p. R829-R858.

26. Hiramatsu, M., et al., *Transparent conducting ZnO thin films prepared by XeCl excimer laser ablation.* Journal of Vacuum Science & Technology A: Vacuum, Surfaces, and Films, 1998. **16**: p. 669.

27. Wang, X.D., C.J. Summers, and Z.L. Wang, *Large-scale hexagonal-patterned growth of aligned ZnO nanorods for nano-optoelectronics and nanosensor arrays.* Nano Letters, 2004. **4**(3): p. 423-426.

28. Zhang, H., et al., *Arrays of ZnO nanowires fabricated by a simple chemical solution route.* Nanotechnology, 2003. **14**(4): p. 423-426.

29. Wang, X., *Large-scale patterned oxide nanostructures: fabrication, characterization and applications*, in *Materials Science and Engineering*. 2005, Georgia Institute of Technology: Atlanta. p. 214.

30. Wan, Q., et al., *Fabrication and ethanol sensing characteristics of ZnO nanowire gas sensors.* Applied Physics Letters, 2004. **84**: p. 3654.

31. Kang, B.S., et al., *pH measurements with single ZnO nanorods integrated with a microchannel.* Applied Physics Letters, 2005. **86**(11): p. 112105.

32. Wang, Z.L. and J.H. Song, *Piezoelectric nanogenerators based on zinc oxide nanowire arrays.* Science, 2006. **312**(5771): p. 242-246.

33. Bai, X.D., et al., *Measuring the work function at a nanobelt tip and at a nanoparticle surface.* Nano Letters, 2003. **3**(8): p. 1147-1150.

34. Voskerician, G., et al., *Biocompatibility and biofouling of MEMS drug delivery devices.* Biomaterials, 2003. **24**(11): p. 1959-1967.

35. Hahm, J. and C.M. Lieber, *Direct ultrasensitive electrical detection of DNA and DNA sequence variations using nanowire nanosensors.* Nano Letters, 2004. **4**(1): p. 51-54.

36. Duan, X.F., et al., *Indium phosphide nanowires as building blocks for nanoscale electronic and optoelectronic devices.* Nature, 2001. **409**(6816): p. 66-69.

37. Huang, Y., et al., *Logic gates and computation from assembled nanowire building blocks.* Science, 2001. **294**(5545): p. 1313-1317.

38. Voldman, J., *Electrical forces for microscale cell manipulation.* Annual Review of Biomedical Engineering, 2006. **8**: p. 425-454.

39. Smith, P.A., et al., *Electric-field assisted assembly and alignment of metallic nanowires.* Applied Physics Letters, 2000. **77**(9): p. 1399-1401.

40. Boote, J.J. and S.D. Evans, *Dielectrophoretic manipulation and electrical characterization of gold nanowires.* Nanotechnology, 2005. **16**(9): p. 1500-1505.

41. Dong, L.F., et al., *Dielectrophoretically controlled fabrication of single-crystal nickel silicide nanowire interconnects.* Nano Letters, 2005. **5**(10): p. 2112-2115.

42. Lao, C.S., et al., *ZnO nanobelt/nanowire Schottky diodes formed by dielectrophoresis alignment across Au electrodes.* Nano Letters, 2006. **6**(2): p. 263-266.

43. Liu, J., et al. *Packaging of ZnO nanobelts as nanosensors: Synthesis, Alignment and Characterization*. in *Electronic Packaging Technology, 2005 6th International Conference on*. 2005. Shenzhen, China.

44. Coppa, B.J., R.F. Davis, and R.J. Nemanich, *Gold Schottky contacts on oxygen plasma-treated, n-type ZnO(000(1)over-bar).* Applied Physics Letters, 2003. **82**(3): p. 400-402.

45. Ip, K., et al., *Contacts to ZnO.* Journal of Crystal Growth, 2006. **287**(1): p. 149-156.

46. Soo Young Kim, e.a., *Low-Resistance Ti/Al Ohmic Contact on Undoped ZnO.* Journal of Electronic Materials, 2002. **31**(8): p. 868-871.

47. Sheng, H., et al., *Ta/Au ohmic contacts to n-type ZnO.* Journal of Electronic Materials, 2003. **32**(9): p. 935-938.

48. Sundaram, K.B. and A. Khan, *Work function determination of zinc oxide films.* Southeastcon'96.'Bringing Together Education, Science and Technology'., Proceedings of the IEEE, 1996: p. 674-676.

49. Huang, Y., et al., *Directed assembly of one-dimensional nanostructures into functional networks.* Science, 2001. **291**(5504): p. 630-633.

50. Liu, J., et al., *Quantifying oxygen diffusion in ZnO nanobelt.* Applied Physics Letters, 2006. **89**(6): p. 063125-3.

51. Fan, Z., et al., *ZnO nanowire field-effect transistor and oxygen sensing property.* Applied Physics Letters, 2004. **85**(24): p. 5923.

52. Look, D.C., J.W. Hemsky, and J.R. Sizelove, *Residual native shallow donor in ZnO.* Physical Review Letters, 1999. **82**(12): p. 2552-2555.

53. Moormann, H., D. Kohl, and G. Heiland, *Variations of work function and surface conductivity on clean cleaved zinc-oxide surfaces by annealing and by hydrogen adsorption.* Surface Science, 1980. **100**(2): p. 302-314.

54. Sabioni, A.C.S., Ramos, et al., *Oxygen diffusion in pure and doped ZnO.* Mat. Res., abr, 2003. **6**(2): p. 173-178.

55. Liu, J., et al., *Label-Free Protein Detection by ZnO Nanowire Based Bio-Sensors.* Electronic Components and Technology Conference, 2007. ECTC'07. Proceedings. 57th, 2007: p. 1971-1976.

56. Wolf, S.F., et al., R*apid hybridization kinetics of dna attached to submicron latex-particles.* Nucleic Acids Research, 1987. **15**(7): p. 2911-2926.

57. McInnes, J.L., N. Habili, and R.H. Symons, N*onradioactive, photobiotin-labeled dna probes for routine diagnosis of viroids in plant-extracts.* Journal of Virological Methods, 1989. **23**(3): p. 299-312.

58. Girotti, S., et al., D*irect quantitative chemiluminescent assays for the detection of viral-dna.* Analytica Chimica Acta, 1991. **255**(2): p. 387-394.

59. Abel, A.P., et al., *Fiber-optic evanescent wave biosensor for the detection of oligonucleotides.* Analytical Chemistry, 1996. **68**(17): p. 2905-2912.

60. Chehab, F.F. and Y.W. Kan, D*etection of specific dna-sequences by fluorescence amplification - a color complementation assay.* Proceedings of the National Academy of Sciences of the United States of America, 1989. **86**(23): p. 9178-9182.

61. Ziegler, C., *Cantilever-based biosensors.* Analytical and Bioanalytical Chemistry, 2004. **379**(7-8): p. 946-959.

62. Andersson, M., et al., *Development of a ChemFET sensor with molecular films of porphyrins as sensitive layer.* Sensors and Actuators B: Chemical, 2001. **77**(1-2): p. 567-571.

63. Patolsky, F., G.F. Zheng, and C.M. Lieber, *Nanowire-based biosensors.* Analytical Chemistry, 2006. **78**(13): p. 4260-4269.

64. Zheng, G.F., et al., *Multiplexed electrical detection of cancer markers with nanowire sensor arrays.* Nature Biotechnology, 2005. **23**(10): p. 1294-1301.

65. Heo, Y.W., et al., *Electrical transport properties of single ZnO nanorods.* Applied Physics Letters, 2004. **85**(11): p. 2002-2004.

66. Souteyrand, E., et al., *Direct detection of the hybridization of synthetic homo-oligomer DNA sequences by field effect.* Journal of Physical Chemistry B, 1997. **101**(15): p. 2980-2985.

67. Stambouli, V., et al., *Development and functionalisation of Sb doped SnO2 thin films for DNA biochip applications.* Sensors and Actuators B-Chemical, 2006. **113**(2): p. 1025-1033.

68. Lu, Q. and S.S. Hu, *Studies on direct electron transfer and biocatalytic properties of hemoglobin in polytetrafluoroethylene film.* Chemical Physics Letters, 2006. **424**(1-3): p. 167-171.

69. Rouhanizadeh, M., et al., *Differentiation of oxidized low density lipoproteins by nanosensors.* Sensors & Actuators: B. Chemical, 2006. **114**(2): p. 788-798.

70. Patolsky, F., et al., *Electrical detection of single viruses.* Proceedings of the National Academy of Sciences of the United States of America, 2004. **101**(39): p. 14017-14022.

71. Javey, A., et al., *Layer-by-layer assembly of nanowires for three-dimensional, multifunctional electronics.* Nano Letters, 2007. **7**(3): p. 773-777.

72. Li, Z., et al., *Sequence-specific label-free DNA sensors based on silicon nanowires.* Nano Letters, 2004. **4**(2): p. 245-247.

73. Gao, Z.Q., et al., *Silicon nanowire arrays for label-free detection of DNA.* Analytical Chemistry, 2007. **79**(9): p. 3291-3297.

74. He, J.H., et al., *ZnS/Silica nanocable field effect transistors as biological and chemical nanosensors.* Journal of Physical Chemistry C, 2007. **111**(33): p. 12152-12156.

75. Fruhauf, J. and S. Kronert, *Wet etching of silicon gratings with triangular profiles.* Microsystem Technologies, 2005. **11**(12): p. 1287-1291.

76. Wang, X.D., et al., *Growth of uniformly aligned ZnO nanowire heterojunction arrays on GaN, AIN, and Al0.5Ga0.5N substrates.* Journal of the American Chemical Society, 2005. **127**(21): p. 7920-7923.

77. Wang, X.D., et al., *Direct-current nanogenerator driven by ultrasonic waves.* Science, 2007. **316**(5821): p. 102-105.

78. Yu, C., et al., *Integration of metal oxide nanobelts with microsystems for nerve agent detection.* Applied Physics Letters, 2005. **86**(6): p. 063101.

79. Wang, Z.L., *Nanopiezotronics.* Advanced Materials, 2007. **19**(6): p. 889-892.

80. Wang, X.D., et al., *Integrated nanogenerators in biofluid.* Nano Letters, 2007. **7**(8): p. 2475-2479.

81. Gao, Y. and Z.L. Wang, *Electrostatic potential in a bent piezoelectric nanowire. The fundamental theory of nanogenerator and nanopiezotronics.* Nano Letters, 2007. **7**(8): p. 2499-2505.

82. Liu, J., et al., *Carrier density and Schottky barrier on the performance of DC nanogenerator.* Nano Letters, 2008. **8**(1): p. 328-332.

VITA

Jin Liu was born in Qingdao, China, in May, 1980. He received his B.E. degree in Materials Science and Engineering from Shanghai Jiaotong University in 2002. After that, Jin went to Singapore for his graduate study. He obtained the M.S. degree in Advanced Materials in Micro- and Nano-systems (AMM&NS) from Sinagpore-MIT-Alliance, a collaboration program among National University of Singapore, Nanyang Technological University, and Massachusetts Institute of Technology, in 2003. During his study in Singapore, he met Prof. Rao Tummala and joined the Packaging Research Center (PRC) of Georgia Institute of Technology in Atlanta, GA, in 2003. At PRC, Jin Liu mainly works with Prof. Zhong Lin (ZL) Wang in the school of Materials Science and Engineering to investigate the properties and applications of one-dimensional ZnO nanostructures. He has been a Graduate Research Assistant in PRC from 2003 to 2008.